Optical overtones and light amplification in metal halide perovskite nanocrystals

Aurora Manzi

München, 2019

Optical overtones and light amplification in metal halide perovskite nanocrystals

Dissertation

submitted by

Aurora Manzi

from Siracusa (Italy)

at the Faculty of Physics
Ludwig-Maximilians-Universität München

Munich, 20.08.2018

Erstgutachten:	Prof. Dr. Jochen Feldmann
Zweitgutachten:	Prof. Dr. Andrey Rogach
Tag der mündlichen Prüfung:	14.10.2019

Solar guitar. It illustrates the analogy between the resonance effect regarding the optical excitation of charge carriers in a semiconductor through *optical overtones*, which is reported in this thesis, and the phenomenon known for music instruments when overtones of two different fundamental notes get into resonance. Photography by Dr. Verena Hintermayr. Edited by M.Sc. Christoph Maier.

To my father

for introducing me
to the beauty of science

Zusammenfassung

Die breitgefächerte Forschung an Halbleitermaterialien hat die direkte Umwandlung von Sonnenlicht in elektrischer Energie ermöglicht. Dieser Prozesses ist jedoch durch eine materialspezifische Eigenschaft (die Bandlücke) limitiert, welche die effiziente Energieumwandlung auf einen kleinen Teil des Sonnenspektrums begrenzt.

In dieser Arbeit werden Methoden entwickelt, um diesen Bereich der effizienten Umwandlung zu erweitern. In den letzten Jahren hat die Gruppe der Metall Halogen Perowskite großes Potential sowohl für die Photovoltaik als auch für lichterzeugende Anwendungen gezeigt. Diese werden daher hier in Form von Nanokristallen untersucht. Die Existenz eines neuartigen Wechselspiels zwischen Photonen unterhalb der Bandlücke und ganzzahligen Vielfachen der exzitonischen Bandlücke des Materials wird in den Nanokristallen entdeckt. Dieser Effekt führt zu einem besonders günstigen Energieaustausch unter bestimmten Resonanzbedingungen, was erstaunlich analog zu dem akustischen Phänomen der Obertöne und deren Resonanzen ist.

Interessanterweise kann dieser Resonanzeffekt nur beobachtet werden, wenn die Nanokristalle zu sogenannten Superkristallen zusammengesetzt werden. Dieses Phänomen kann auf den Rückgang der Auger Rekombination aufgrund der elektronischen Kopplung zwischen den einzelnen Nanokristallen zurückgeführt werden. Während die Geometrie der Superkristalle beibehalten wird, kann die chemische Zusammensetzung der Perowskite variiert werden, um die energetische Position der Resonanzen abzustimmen. Der Effekt der elektronischen Kopplung auf die Lichtemissions- und die Lichtverstärkungseigenschaften der Perowskit-Nanokristalle wird ebenfalls analysiert. Der Einspeisungsmechanismus für verstärkte spontane Emission wird untersucht und es wird festgestellt, dass die Emission aus den Superkristallen für die Lichtverstärkung im System verantwortlich ist.

Diese Erkenntnisse sind für Anwendungen in Solarzellen relevant, da die Gewinnung und Umwandlung der maximalen Lichtmenge in nutzbare Energie und damit die Reduzierung von Verlusten eines der Hauptziele ist, um die Shockley-Queisser-Grenze zu überwinden und einen höheren Wirkungsgrad in den Solarzellen von morgen zu erzielen.

Abstract

The rise of semiconductor materials has paved the way for the direct conversion of solar light into usable electric energy. However, this process is limited by a material-specific property (the bandgap), which demarcates the efficient energy conversion to a small portion of the solar spectrum.

In this thesis, steps towards extending this range of efficient conversion are taken. To this end, metal halide perovskites, a class of materials which have been recently shown to possess a huge potential for photovoltaic as well as for light-emitting applications, are analysed here in the form of nanocrystals. The existence of a novel interplay between below-bandgap photons and integer multiples of the material excitonic bandgap is revealed in these nanocrystals. This effect leads to an energy exchange that is particularly favoured under specific resonant conditions, which is amazingly analogue to the acoustic phenomenon of overtones and their resonances.

Interestingly, this resonance effect is observed only when the nanocrystals are assembled in an ordered fashion, forming so-called supercrystals. This phenomenon can be attributed to a reduction in incidence of Auger recombination as a result of the electronic coupling between the individual nanocrystals. When the supercrystal geometry is kept, the chemical composition of the perovskites can be varied to tune the energetic position of the resonances. The effect of electronic coupling on the light emission and light amplification properties of the perovskite nanocrystals is analysed as well. The feeding mechanism for amplified spontaneous emission is investigated and the emission from the supercrystals is revealed to be responsible for the light amplification in the system.

These findings are relevant for the design of solar cells, as harvesting and converting the maximum amount of light into usable power, hence reducing the losses, is one of the main goals to overcome the Shockley-Queisser limit to achieve higher efficiency in the solar cells of tomorrow.

List of publications and awards

Scientific publications of results presented in this work

- A. Manzi*, Y. Tong, J. Feucht, E.-P. Yao, L. Polavarapu, A.S Urban, J. Feldmann*; Resonantly enhanced multiple exciton generation through below-band-gap multi-photon absorption in perovskite nanocrystals, Nature communications, 9, 1 (2018)
- Y. Tong, E. Bladt, M.F Aygüler, A. Manzi, K.Z Milowska, V.A Hintermayr, P. Docampo, S. Bals*, A. S Urban*, L. Polavarapu*, J. Feldmann; Highly luminescent cesium lead halide perovskite nanocrystals with tunable composition and thickness by ultrasonication; Angewandte Chemie International Edition, 55, 44 (2016)
- Y. Tong, E. Bladt, M.F Aygüler, A. Manzi, K.Z Milowska, V.A Hintermayr, P. Docampo, S. Bals*, A. S Urban*, L. Polavarapu*, J. Feldmann; Starke Lumineszenz in Nanokristallen aus Caesiumbleihalogenid-Perowskit mit durchstimmbarer Zusammensetzung und Dicke mittels Ultraschalldispersion; Angewandte Chemie, 128, 44 (2016)
- Y. Tong, E.-P. Yao, A. Manzi, E. Bladt, K. Wang, M. Döblinger, S. Bals, P. Müller-Buschbaum, A.S Urban, L. Polavarapu*, J. Feldmann; Spontaneous Self-Assembly of Perovskite Nanocrystals into Electronically Coupled Supercrystals: Toward Filling the Green Gap, Advanced Materials, 1801117 (2018)

Additional publications

- D.C Mayer, A. Manzi, R. Medishetty, B. Winkler, C. Schneider, G. Kieslich, A. Pöthig, J. Feldmann, R.A Fischer; Controlling Multi-Photon Absorption Efficiency by Chromophore Packing in Metal-Organic Frameworks; Journal of the American Chemical Society, 141, 29 (2019)

- R. Wang, Y. Tong, A. Manzi, K. Wang, Z. Fu, E. Kentzinger, J. Feldmann, A.S Urban, P. Müller-Buschbaum, H. Frielinghaus; Preferential Orientation of Crystals Induced by Incorporation of Organic Ligands in Mixed-Dimensional Hybrid Perovskite Films, Advanced Optical Materials, 6, 6 (2018)
- R.D Nagel, S. Filser, T. Zhang, A. Manzi, K. Schönleber, J. Lindsly, J. Zimmermann, T.L Maier, G. Scarpa, K. Krischer, P. Lugli; Nanoimprint methods for the fabrication of macroscopic plasmonically active metal nanostructures, Journal of Applied Physics, 121, 8 (2017)
- A. Manzi, T. Simon, C. Sonnleitner, M. Döblinger, O. Stern, J. K. Stolarczyk, J. Feldmann; Light-induced cation exchange for photocatalytic CO2 reduction on Cu2S/CdS nanorods; Journal of the American Chemical Society, 137, 44 (2015)

Awarded

- CeNS Nano Innovation Award for PhD Thesis - Shortlisted candidate (2018)
- CeNS Travel Award - Poster at the MRS Fall Meeting Boston (2017)
- ACS Nano “Best poster award” in NaNaX8, Braga (2017)
- CeNS Innovation Award for Master Thesis (2015)

Conference contributions

Presentations and Posters

- Oral presentation at the “Workshop on Optical Spectroscopy of New Materials (OPTIMA)”, Haigerloch, Germany (2019, March)
- Oral presentation at the Materials Research Society Conference “MRS Fall Meeting 2018”, Boston, USA (2018, Nov.)
- Poster presentation at the “7th SolTech Conference-2018”, Würzburg, Germany (2018, Oct.)
- Oral presentation at the PSCO-2018: ”Conference on Perovskite Solar Cells and Optoelectronics”, Lausanne, Switzerland (2018, Sept.)
- Poster presentation at the CeNS Workshop “Celebrating Nanoscience”, Venice, Italy (2018, Sept.)
- Poster presentation at the Materials Research Society Conference “MRS Fall Meeting 2017”, Boston, USA (2017, Nov.)
- Poster presentation at the 6th SolTech Conference “Solar Technologies Go Hybrid”, Munich, Germany (2017, Oct.)
- Poster presentation at the conference “NaNaX8 – Nanoscience with nanocrystals”, Braga, Portugal (2017, July)
- Poster presentation at the conference “Nanotech France 2017”, Paris, France (2017, June)
- Oral presentation at the “PhOG Workshop on Optical Spectroscopy of New Materials (OPTIMA)”, Syracuse, Italy (2017, March)

- Oral presentation at the “PhOG Workshop on Photonics and Optoelectronics with New Materials”, Fall/Lenggries, Germany (2016, July)
- Poster presentation at the 5th International SolTech Conference “Solar Technologies Go Hybrid”, Munich, Germany (2016, April)
- Poster presentation at the “NIM Winterschool”, Kirchberg, Austria (2016, March)
- Oral presentation at the “DPG (Deutsche Physikalische Gesellschaft) Frühjahrstagung 2016” - section condensed matter, Regensburg, Germany (2016, Feb.)
- Invited talk at the CeNS Workshop “Channels and Bridges to the Nanoworld”, Venice, Italy (2015, Sept.)
- Poster presentation at the “CFP / NIM Workshop on Functional Photonics and Nanosystems”, Hong Kong (2015, May)
- Oral presentation at the “Nanotechnology for Next Generation High Efficiency Photovoltaics - NEXTGEN NANO PV” Spring International School and Workshop, Menorca, Spain (2015, April)
- Invited talk at the 4th International “Solar Technologies Go Hybrid - SolTech” Workshop, Kloster Banz, Germany (2015, March)

Memberships

Member of the NIM ‘Nano Initiative Munich” Graduate Program (2015-2019)

Contents

1 Introduction

Semiconductors are nowadays the most prominent materials for applications in opto-electronic devices aimed at converting solar light into usable electric energy. The International Energy Agency (IEA) reported that every day during the last year half a million solar panels have been installed around the world [1]. However, nowadays solar cells still suffer from relatively low energy conversion efficiencies. The Shockley-Queisser limit fixes the theoretical maximum efficiency to 33% for solar energy conversion in a single p-n junction photovoltaic device [2]. The energetic losses in such a process have their origin mainly in the bandgap limited absorption of semiconductors. This material property, the bandgap, defines the energetic region where solar light can be efficiently converted into electrical power. While below-bandgap photons normally pass through the material without generating currents, above-bandgap photons lose their excess energy into heat. Maximizing the amount of light harvested and converting it into usable power with the lowest amount of losses is hence still a big challenge and one of the main goals for solar cell fabrication.

Multiple exciton generation (MEG) is a process that addresses the conversion of highly energetic photons by using their excess energy to promote additional electrons to the conduction band [3–16]. However, this process requires that the energy of the exciting photon is at least twice that of the bandgap of the semiconductor. On the other hand, multi-photon absorption (MPA) is a process that allows to create charges in semiconductors at high light intensities of multiple below-bandgap photons which, if taken together, can overcome the bandgap [17–21]. Despite the increase in the absorption given by this process, the typical two-photon absorption alone, does not impact crucially on the total energy conversion efficiency of solar cells.

Before my PhD thesis, these two processes (MEG and MPA) have only been investigated independently from each other. It was demonstrated that the absorption of either high- or low-energetic photons can be improved in some specific situations, however with efficiencies too low to enable technological applications. The motivation behind this thesis is to tackle the problem of the bandgap limited photo-conversion in solar cells. To this end, MEG and MPA are for the first time targeted together.

To study the possible interplay of these phenomena, metal halide perovskite nanocrystals are synthesised and used as test model. This choice is driven by the high potential of perovskites for photovoltaic applications which was shown over the last few years [22–24]. Perovskite nanocrystals with different halide composition and geometries, both of which have a strong influence in the optoelectronic properties of the final material, are also analysed in this thesis work. Additionally, following a synthesis route that allows the creation of ordered arrangements of these nanocrystals, the different optical responses of isolated nanocrystals and electronically coupled so-called supercrystals are also reported.

Furthermore, both electronically coupled and uncoupled perovskite structures are analysed under high-intensity optical pumping conditions towards optoelectronic applications of these nanocrystals. In such a way, their light emission and light amplification properties are investigated and correlated with their geometrical ones.

2 Fundamentals

In this chapter the fundamental theory, which is necessary for the understanding of the physical phenomena reported in this thesis, is given. The need to overcome the limitations of the current semiconductor-based photovoltaics technology, mainly expressed by the Schockley-Queisser limit, is firstly discussed. Possible solutions to go beyond this theoretical limitation are introduced and, in this respect, concepts such as nonlinear absorption and carrier multiplication are presented. The light emitting properties of semiconductors are analysed, along with the effects of high intensity optical pumping, leading to amplified spontaneous emission (ASE) and optical gain. Finally, lead halide perovskite nanocrystals, on which the research done in this thesis work is focused, are introduced and the main concepts useful for the understanding of their unique optoelectronical properties are presented.

2.1 The Shockley-Queisser limit

The Shockley-Queisser (SQ) limit was first introduced in 1961 by William Shockley and Hans-Joachim Queisser [2]. In their publication, they calculated the maximum theoretical efficiency of a solar cell using a single p-n junction to convert solar to electrical power[1]. Assuming a semiconductor with a bandgap energy of 1.1 eV (such as, for instance, silicon), the maximum solar conversion efficiency is around 32%, assuming typical sunlight conditions (which can be referred to using the syntax "AM1.5" solar spectrum[2]). The bandgap of the employed semiconductor influences the maximum conversion efficiency, and even increases it up to a maximum conversion efficiency of 33.7% , which can be found by using semiconductors with a bandgap of 1.34 eV (see Figure 2.1).

The reason why only around one third of the light impinging on a solar cell can be converted into usable electric power is to be found in the lossy conversion processes that photons with an energy different from the semiconductor bandgap energy must undergo. For instance, if the absorbed photon has an energy which is higher than the bandgap energy, the photogenerated *electrons* and *holes*[3] have an excess of energy. When this happens, the charge carriers are often referred to as "hot carriers". This over-energy is usually lost through the interactions of the charge carriers with *phonons*[4], a relaxation process called cooling (represented by the red area in Figure 2.1). On the other hand, if photons have an energy which is lower than the bandgap energy, they pass the semiconductor without being absorbed as their energy is not high enough to optically generate charge carriers. These photons are therefore not contributing to

[1] In this thesis, the possibility to increase the conversion efficiency of solar cells through multiple p-n junctions (i.e. tandem solar cells) made of different semiconductor materials is not treated. However, this approach could also address the limitations of single p-n junction solar cells.

[2] The syntax "AM" is used to characterize the solar spectrum after passing through the Earth's atmosphere. AM stands for the *air mass coefficient*, whereas the number following it represents the optical path length through the atmosphere L, divided by the zenith path length (hence the one perpendicular to the Earth's surface) at sea level L_0. This number is therefore dependent on the Sun's elevation and on the latitude at which it is measured. AM1.5 represents an yearly average value for mid-latitudes.

[3] A hole is a quasiparticle identifying the lack of an electron. While the electron is characterised by a negative charge and, through photoexcitation, gets energetically promoted from the valence to the conduction band, the hole represents the positive charge which is remaining in the valence band when a photon is absorbed.

[4] A phonon is a quasiparticle representing lattice vibrations.

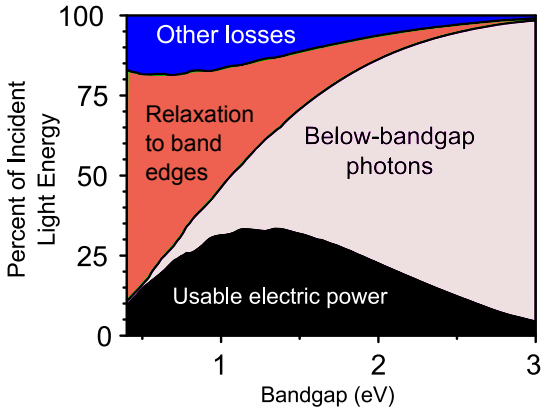

Figure 2.1: Schematics showing the percent of incident light energy which can be efficiently converted into usable electric power (black area) versus the bandgap energy of the material employed as absorber. The pink area corresponds to the percent of incident light energy which is lost because constituted by below-bandgap photons, whereas the red area is representing the losses due to above-bandgap photons. All the additional losses are included in the blue area, which contains the radiative recombination of the photogenerated carriers [2].

the energy conversion process at all. Hence, they represent a part of the solar spectrum which is completely lost (pink-coloured area in Figure 2.1).

The thermalised energy of photons with an energy above the bandgap and the non-absorbed photons with an energy below the bandgap constitute the major loss mechanisms in the SQ limit. Other additional losses are due to voltage loss because of thermal radiation and fill factors which differ from 100% (blue area in Figure 2.1).

In this thesis, steps aimed at increasing the efficiency of light conversion to usable electric power, crossing the restrictions given by the SQ limit, will be taken. To this end, the concepts of multi-photon absorption and carrier multiplication are introduced in the subsequent sections.

2.2 Optical nonlinearities: multi-photon absorption

Multi-photon absorption (MPA) is a process in which, at high optical excitation intensity, the simultaneous absorption of more than one low-energy photons becomes possible in semiconductors [25]. Exploiting this principle is therefore a way to go beyond the SQ limit, as below-bandgap photons would then contribute to the absorption process rather than be lost.

MPA is a particular case of optical nonlinearities, which occur when the response of a semiconductor to an applied optical field depends in a nonlinear manner upon the strength of the optical field. These, in turn, are manifested in changes in the optical properties of the material as the intensity of the light excitation is varied. Being the strength of the nonlinearity highly dependent on the intensity of the exciting optical field, these are typically observed under high light intensities and have therefore been discovered in 1961, right after the construction of the first laser[5] in 1960 [26].

To express the concept of nonlinearities in a mathematical manner, one should consider the variation of the polarization density $\vec{P}(t)$ in a material in response to an applied electromagnetic field $\vec{E}(t)$ [27]. In the case of linear optics the two terms are linearly proportional, as depicted by:

$$\vec{P}(t) = \varepsilon_0 \chi_e \vec{E}(t) \tag{2.1}$$

where ε_0 is the vacuum permittivity and χ_e is the electric susceptibility, a dimensionless constant indicating the degree of polarization of a material when an electromagnetic field is applied[6]. The polarization density is a vector field that expresses the density of electric dipole moments (permanent or not) in a material. Instead, in nonlinear optics the equation 2.1 has to be generalized in order to be valid. This operation can be done by expressing $\vec{P}(t)$ as a Taylor series expansion of the field strength:

$$\vec{P}(t) = \varepsilon_0 \left(\chi^{(1)} \vec{E}(t) + \chi^{(2)} \vec{E^2}(t) + \chi^{(3)} \vec{E^3}(t) + ... \right) \tag{2.2}$$

[5] A laser, which acronym stands for: "Light Amplification by Stimulated Emission of Radiation", is a device that emits high intensity light coherently.

[6] The greater χ_e , the greater the ability of a material to polarize, e.g. to minimize the total electromagnetic field inside the material.

where $\chi^{(n)}$ is a n+1 tensor representing the n-th order nonlinear optical susceptibility corresponding to the n-th order nonlinearity. This tensor encloses the information on the polarization-dependent nature of the material, as well as its symmetries (or lack of). If a material is centrosymmetric, i.e. possesses a center of inversion, meaning it displays inversion symmetry, then all the even-order nonlinear susceptibilities must vanish identically:

$$\chi^{(even)} = 0 \tag{2.3}$$

Examples of centrosymmetric materials are liquids, gases, amorphous solids. On the other hand, odd-order nonlinearities can occur both for centrosymmetric and noncentrosymmetric materials.

2.2.1 Parametric and non-parametric nonlinearities

Optical nonlinearities can be classified as parametric and non-parametric. This distinction is based on the occurrence (or the absence) of a change in the quantum mechanical states of the material undergoing the nonlinear effect [28].

A nonlinear effect can be classified as:

- **parametric** if the quantum state of the material is not changed by the interaction with the excitation optical field. This means that the population of charge carriers can vary in the ground- and excited-states only for a brief interval of time, when it resides in a so-called "*virtual state*". The nature of this exchange is therefore instantaneous. Examples of parametric effects are:
  - 2^{nd} **order** $\chi^{(2)}$: SHG, SFG, DFG, OR[7];
  - 3^{rd} **order** $\chi^{(3)}$: THG, IDRI[8].

[7]These acronyms stand for, respectively: second-harmonic generation, also known as *frequency doubling* (two photons create a single photon with twice the frequency, i.e. half the wavelength, of the original photons); sum-frequency generation (two photons with different frequencies create one photon with a frequency that is the sum of the two original frequencies); difference-frequency generation (two photons with different frequencies create one photon with a frequency that is the difference of the two original frequencies); optical rectification (the optical beam, which is a sinusoidal electromagnetic field, generates an average DC polarization in the material).

[8]These acronyms stand for, respectively: third-harmonic generation (three photons create a single photon at three times the frequency, i.e. one third the wavelength, of the original photons); intensity-dependent refractive index (the optical beam induces a change in the refractive index of the material

- **non-parametric** if the quantum mechanical state changes over time with the interaction with the excitation optical field. This means that there is a transfer of population from the ground-state to excited-states.
  - 3^{rd} **order** $\chi^{(3)}$: Two-photon absorption (2PA);
  - 5^{th} **order** $\chi^{(5)}$: Three-photon absorption (3PA).

2.2.2 Linear absorption *vs* multi-photon absorption

In the previous subsections the definition of optical nonlinearity and the introduction to the subclass of non-parametric processes, to which the multi-photon absorption processes belong, were given. To properly describe the latter it is important to analyse the linear process of light absorption, in order to understand their analogies and differences.

The term *absorption* refers to the physical process of energy transfer from light (photons) to matter (electrons and holes in the case of semiconductors). If this process involves a single photon to generate one electron-hole pair, then we refer to it as linear absorption. For this process to happen, the requirement for the photon to be absorbed is that its energy is at least as high as the semiconductor bandgap [9] and that the crystal quasi-momentum is conserved (see section 2.4 for more details).

While absorption shall be understood as the physical process of absorbing light, the quantity which is usually measured to quantify it is called *absorbance*. This is defined as the radiant power (also known as *attenuation*) lost passing through a certain cross section of the material. As such, the attenuation can also be due to other physical processes, such as reflection and scattering. However, for simplicity reasons, let us consider the case when the attenuation is mainly due to absorption (i.e. scattering and reflection can be neglected).

The Beer-Lambert law relates the transmittance T of light to the optical depth τ of the material where it is propagating and to its absorbance A [29]:

where it is propagating, which, in turn, influences the propagation of the beam. It is a special case of the optical Kerr effect and implies the process of self-focusing).

[9] In the case where *excitons* may be present, this is not fully correct. An exciton is a neutral quasiparticle consisting of a bound state of an electron and a hole. The Coulomb force governing this interaction lowers down the energy required for their creation with respect to the energy necessary to generate free (unbound) charges in a semiconductor. Therefore, photons with an energy slightly below the bandgap energy can be absorbed and form excitons.

$$T = \frac{\phi_t}{\phi_i} = e^{-\tau} = 10^{-A} \tag{2.4}$$

where ϕ_t is the radiant flux transmitted by the material, whereas ϕ_i is the one incident on it. τ can also be related to the linear attenuation coefficient (also known as extinction coefficient or absorption coefficient) α: $\tau = \alpha l$ where l is the path length (or cross section).

The absorbance can therefore be derived from equation 2.4:

$$A = -logT = log\frac{\phi_i}{\phi_t} \tag{2.5}$$

Instead, if scattering (S) and reflectance (R) play a role, the transmittance and absorbance are related by:

$$T + A + R + S = 1 \tag{2.6}$$

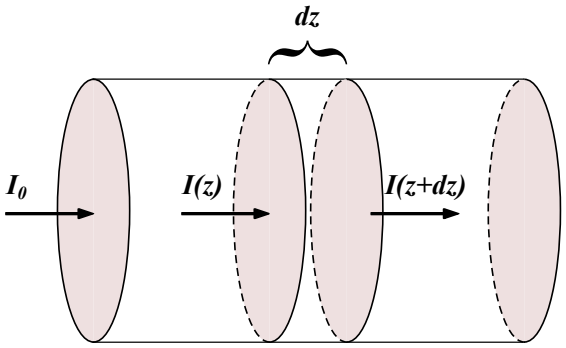

Figure 2.2: Schematic representation of the cross-section of an absorbing material. I_0 represents the intensity of light impinging on the material, whereas $I(z)$ the value it assumes at a certain position z across the cross section.

Considering the light intensity of the incident beam propagating along the z-axis $I(z)$ (see Figure 2.2), its attenuation can be expressed by the phenomenological expression:

$$\frac{dI(z)}{dz} = -\alpha I(z) \tag{2.7}$$

solving this differential equation, we can derive another expression of the Beer-Lambert law:

$$I(z) = I_0 e^{-\alpha z} \tag{2.8}$$

where *I(z)* is the light intensity as a function of the cross section x and I_0 is the initial light intensity impinging on the material.

Keeping this formalism, we can now introduce the effects of MPA on the light attenuation [28]:

$$\frac{dI(z)}{dz} = -\alpha I(z) - \beta I^2(z) - \gamma I^3(z) - \eta I^4(z)... \tag{2.9}$$

where α, β, γ and η are the one-, two-, three- and four-photon absorption coefficients, respectively.

For a pure 2PA process, the equation 2.9 would then become:

$$\frac{dI(z)}{dz} = -\beta I^2(z) \qquad \text{(2PA)} \tag{2.10}$$

which means that the probability that the material undergoes 2PA depends quadratically on the intensity of the light beam. Additionally considering the dependence of the energy of the incidence photons (and hence of their wavelength λ), the solution of equation 2.10 is:

$$I(z,\lambda) = \frac{I_0(\lambda)}{1 + \beta(\lambda) I_0(\lambda) z} \qquad \text{(2PA)} \tag{2.11}$$

Similarly, the probability to have a pure 3PA process is proportional to the third power of the local light intensity I^3:

$$\frac{dI(z)}{dz} = -\gamma I^3(z) \qquad \text{(3PA)} \tag{2.12}$$

whereas for a pure 4PA this will be proportional to the fourth power I^4.

$$\frac{dI(z)}{dz} = -\eta I^4(z) \qquad \text{(4PA)} \tag{2.13}$$

The physical meaning of these equations is that the probability of having an n–th order nonlinear absorption is proportional to the n–th power of the local light intensity [28].

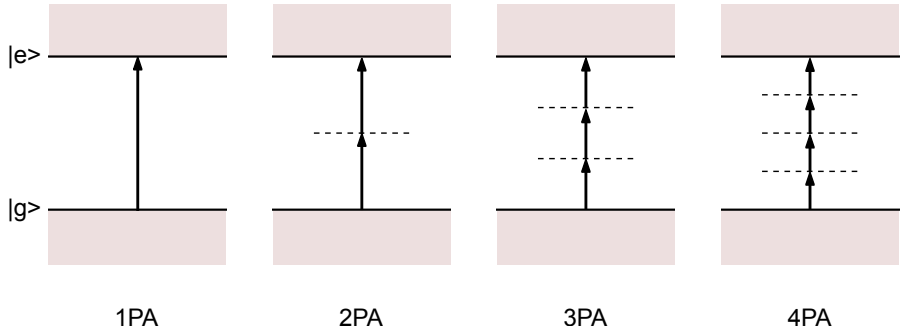

Figure 2.3: Schematic description of linear (1PA) and nonlinear (2PA, 3PA and 4PA) absorption processes. The solid lines represent real ground and excited states ($|g\rangle$ and $|e\rangle$, respectively), whereas the dashed lines represent intermediate virtual states.

A schematic representation of the linear (1PA) and nonlinear (2PA, 3PA and 4PA) multi-photon absorption processes is depicted in Figure 2.3. In this graph, the solid lines represent real ground and excited states, whereas the dashed lines represent the intermediate virtual states.

In this thesis, the possibility to achieve high-order multi-photon absorption events, which appear in correspondence of well-defined resonances between the exitation energy and the bandgap energy, is reported. This phenomenon is extensively discussed in Chapter 4.

2.3 Carrier multiplication

Carrier multiplication (CM) is a process in which the absorption of a single high-energetic photon leads to the creation of multiple electron-hole (e-h) pairs [30]. It therefore constitutes a way to efficiently convert the energy of above-bandgap photons into usable electric power, thus reducing the losses due to thermalisation[10] and offering a way to overcome the SQ limit[11]. CM is usually referred to as *impact ionization* [31] in the case of bulk semiconductors and as *multiple exciton generation* [32] (MEG) in the case of semiconductor nanocrystals. Although more rarely, CM appears in literature also under the name *quantum cutting*, which directly refers to the fact that a high-energy photon can be "divided" into a certain number of low-energetic photons (which are emitted as a consequence of the radiative recombination of the photo-generated multiple e-h pairs) [33].

To observe CM the following requirements between the photon involved in the photoexcitation and the multiple charge-carriers subsequently generated have to be fulfilled:

- energy conservation ;
- momentum conservation.

However, due to the discrete nature of their excitonic states, the requirement of momentum conservation is relaxed for zero dimensional (0D) quantum-confined semiconductors[12]. This effect lowers the threshold for CM in these systems, meaning that every time a photon involved in the photo-excitation has an excess energy $\Delta E = h\nu - E_g$ overcoming a multiple of the bandgap energy E_g, one additional e-h pair can be generated

[10] Thermalisation is the process by means of which optically excited charge carriers loose their over energy by cooling to the band edge through phonon scattering, hence transferring their excess energy into lattice vibrations in the form of heat.This process stops when the charge carriers and the lattice phonons reach the same temperature (i.e. are in thermal equilibrium).

[11] It has been demonstrated that a power conversion efficiency up to ~ 44% can be expected by employing CM in solar cells [10].

[12] Quantum confinement can be observed in semiconductors once the size of the material is comparable with the diameter of the exciton (which is characterized by twice the *exciton Bohr radius*, i.e. the distance in an e-h pair). When this happens, the excitons can be described with the "particle in a box" model , which leads to a strong deviation of the semiconductor properties from those of bulk semiconductors. Together with the appearance of discrete energy levels, there is an increase of the bandgap energy in quantum-confined semiconductors (and therefore a blue-shift of their photoluminescence).

(e.g, if the photon energy is $E_{photon} = h\nu \geq 2E_g$, its absorption can lead to the creation of two e-h pairs. If $E_{photon} = h\nu \geq 3E_g$, three e-h pairs can be generated, and so on).

Different quantum mechanical approaches involving density matrices have been proposed and are still under debate to describe the microscopic origin of MEG:

1. The photo-excitation leads to a high-energy e-h pair which decays into a number of multiexciton states available at this energy (i.e., the photon excess energy is high enough to promote additional electrons from the valence band to the conduction band). This process occurs through a real state, which is associated to the photo-generated hot e-h pair [30].

2. The photo-excitation creates an e-h pair which can coherently be converted into multiexcitons (which can again be converted into an exciton, and this process can be repeated many times) [34]. There is, in this case, a coherent superposition of single and multiexcitons states.

3. Multiple excitons are formed through a virtual e-h pair state, from which the final optical transition to the final two-exciton state takes place [4].

Besides competing against hot-carrier cooling, MEG is also hindered by *Auger recombination* (AR), which is its reverse process where an e-h pair recombines non-radiatively by transferring its energy to another charge carrier and increasing its energy. Being the probability for AR dependent on the electron density n and the hole density p like n^2p or np^2 (it is a three-particle process), it is more likely to happen in systems with a high density of charge carriers.

However, it has been demonstrated that AR can be suppressed in favour of radiative recombination of the photo-generated multiple excitons in dense solid-state dispersions of nanocrystals (see Figure 2.4) [35]. The reason for this suppression is that the interaction between the closely-arranged nanocrystals strongly enhances the overlap of their carriers wave functions up to a point where *minibands* are created. Minibands lead to a rapid spatial separation of the photo-generated multiple excitons throughout the sample, which consequently results in a suppression of the probability of AR recombination events.

In this thesis, the presence of MEG in semiconducting nanocrystals is observed in correspondence with specific resonance conditions between the photoexcitation and

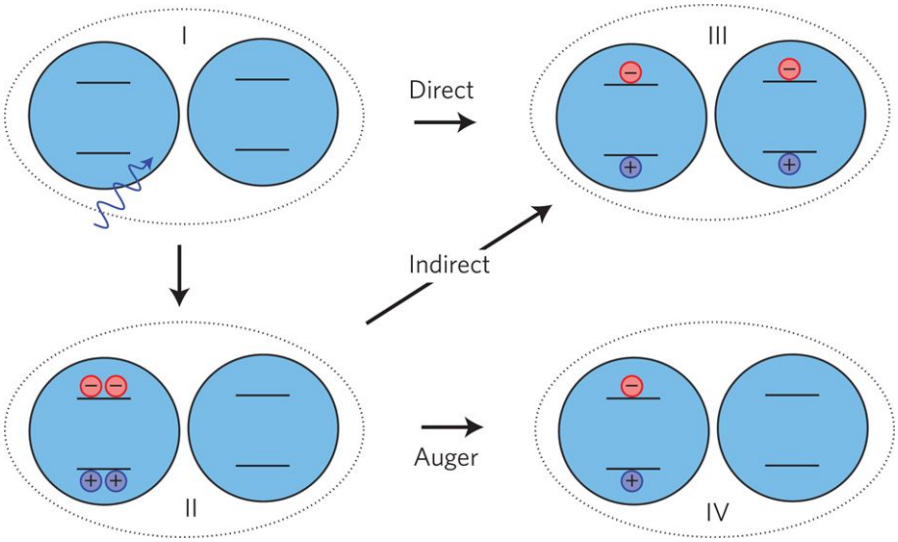

Figure 2.4: Absorption of a high-energy photon (I) can lead to the formation of multiple excitons. The excitons can either be confined in a single crystal (II) or delocalized in two adjacent crystals (III). When the excitons are confined in a single crystal (II) there is a high probability that they will recombine non-radiatively through Auger recombination (IV). This figure is taken from Trinh et al. [35].

the exciton energy. The creation of multiple excitons is identified through an increase in the radiative recombination rate in the system. Further details on these investigations are given in Chapter 4.

2.3.1 Superlattices and miniband formation

Minibands can form in periodic material arrays (e.g. supercrystals) where two different materials are periodically arranged one next to the other, and they are thin enough to allow electronic coupling between the different components [36, 37]. The ordered state of the components of a superlattice can then be related to the ordered arrangements of atoms in crystal lattices. As a result, the band structure of the isolated materials is changed as the wavefunctions of the two adjacent materials can mix, producing a split in the energy levels that, as it is repeated for the many components in the supercrystal, creates minibands instead of discrete energy levels. The presence of minibands not only changes the effective bandstructure of the material, but also favours delocalization of charge carriers over the supercrystals and hence mobility.

The miniband formation can be understood considering superlattices as multiple quantum well structures. These are alternating series of wells and barriers that well represent the superlattice configuration when the barrier thickness is thin enough to allow electronic coupling between the neighbouring quantum wells (see Figure 2.5).

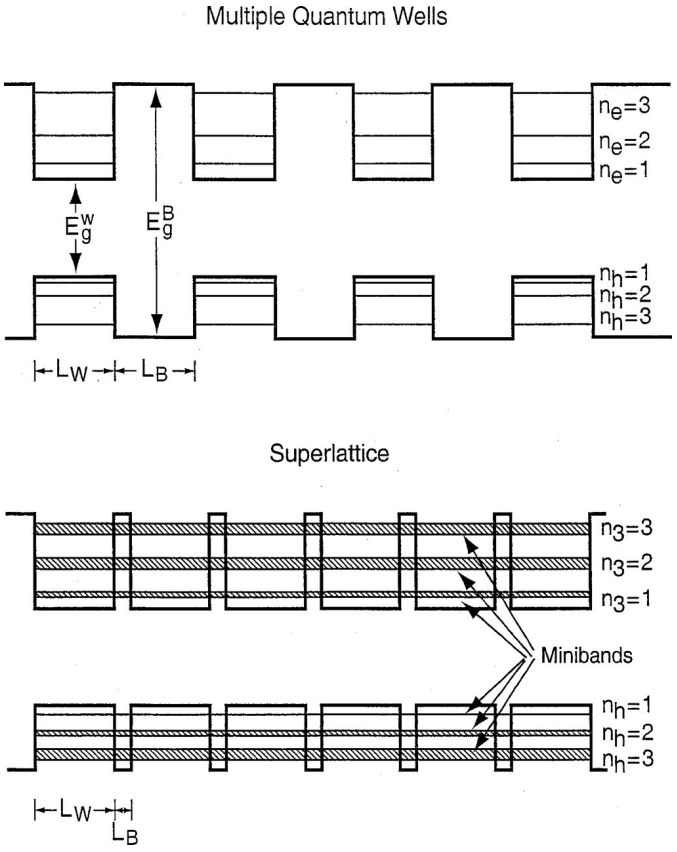

Figure 2.5: Schematics of the multiple quantum well (top side) and of the superlattices (down side) energy dispersion. This figure is taken from Nozik et al. [36].

The width of the minibands (i.e. the energy difference between the highest and the lowest energies constituting the band) is usually different in the valence and conduction band as it depends on the effective mass of the charge carriers (larger effective masses result in narrower minibands). The nomenclature 2Δ is typically employed to address the width of a miniband.

This energy width can be calculated using an eigenvalue equation given by:

$$cos(KD) = cos(\alpha L_W)\, cosh(\beta L_B) + \frac{1}{2}\left(\frac{m^*_W\beta}{m^*_B\alpha} - \frac{m^*_B\alpha}{m^*_W\beta}\right) sin(\alpha L_W)\, sinh(\beta L_B). \tag{2.14}$$

This calculation is based on the Kronig-Penney model [38], where K is the reciprocal wavevector, D is the superlattice period, m^*_W and m^*_B are the effective masses in the well and barrier material, respectively, L_W and L_B are the thicknesses of the wells and of the barriers. The two parameters α and β are defined as:

$$\alpha^2 = \frac{2m^*_W E}{\hbar^2} \tag{2.15}$$

and

$$\beta^2 = \frac{2m^*_B(V - E)}{\hbar^2} \tag{2.16}$$

where V is the band offset.

In this thesis, owing to the difficulties involved in estimating the heights of the energy barriers in closely-packed perovskite aggregates, the calculation of the miniband widths is not included. However, the effect of electronic coupling between adjacent nanocrystals is analysed. This phenomenon can happen through spontaneous self-organization of the nanocrystals into closely-packed arrangements (as observed in Chapter 4 and 5) or can be induced by employing specific synthesis techniques (as reported in Chapter 6). In both cases, this effect leads to a series of beneficial properties for the resulting material such as, to name a few: (i) a decreased amount of nonradiative recombination of the photogenerated charge carriers, (ii) bandgap tunability due to the formation of minibands, (iii) easier achievement of population inversion.

2.4 Light emission in semiconductors

To describe the basic interaction of light with the electrons and holes in a semiconductor, the concept of *crystal quasi-momentum* is usually introduced [39]. This quantity is associated to the charge carriers in a semiconductor and is defined as:

$$\mathbf{p} = \hbar\mathbf{k} \tag{2.17}$$

being $\mathbf{p}$ the crystal quasi-momentum and $\mathbf{k}$ the wavevector of the electron (or the hole), which is dependent on the quantum mechanical state where it is allocated.

The crystal quasi-momentum differs from the classical definition of momentum in that it includes the effect of the presence of the crystal on the mass of the carriers. An *effective mass* m^* is therefore defined to keep the analogy with free electrons[13].

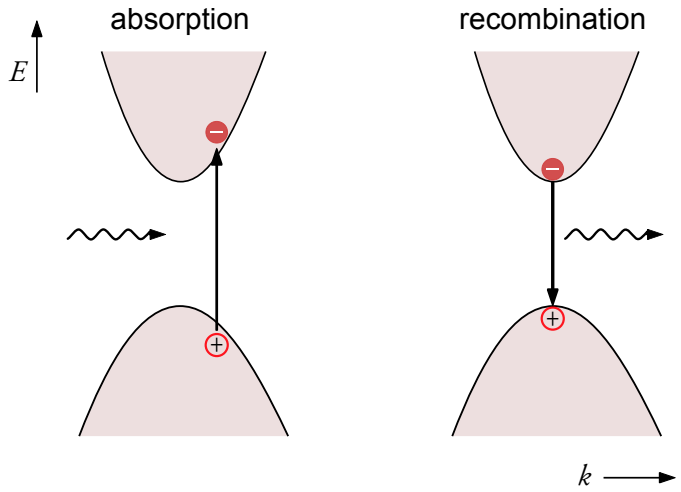

Figure 2.6: Schematic representation of the processes of photon absorption (left side) and charge carrier recombination (right side) in a semiconductor.

The total crystal quasi-momentum in a semiconductor has to be conserved:

$$\sum_i \mathbf{k}_i = 0 \tag{2.18}$$

[13]The effective mass m^* is defined as: $m^* = \hbar^2 \left[\frac{\mathrm{d}^2E}{\mathrm{d}k^2}\right]^{-1}$.

Therefore, when an electron is removed from the valence band (i.e. an hole is created), the electron assumes a wavevector in the conduction band $\mathbf{k}_e$ which is the opposite of the wavevector $\mathbf{k}_h$ of the hole:

$$\mathbf{k}_e = -\mathbf{k}_h \tag{2.19}$$

On the other hand, photons can also be described by associating them with an energy E:

$$E = h\nu \tag{2.20}$$

where ν is the photon frequency, which is connected to its wavelength λ by: $c = \nu\lambda$ being c the speed of light in vacuum.

Since the photon momentum is negligible, all the transitions involving photons in semiconductors are "vertical", meaning that the momentum of the electron is not changed following photon absorption or emission:

$$\mathbf{k}_i - \mathbf{k}_f = 0 \tag{2.21}$$

where $\mathbf{k}_i$ is the initial $\mathbf{k}$-vector of the electron and $\mathbf{k}_f$ is the final one.

The crystal momentum of an electron (or hole) can therefore be changed only through scattering events with another quasi-particle carrying momentum, such as another electron (or hole) or phonons.

Due to energy conservation, the final energy of the electron after an absorption event is equal to its energy before the interaction plus the energy of the absorbed photon. On the other side, an electron and a hole located at the band edge can recombine radiatively emitting light with an energy that is equal to the energy difference between the two charge carriers.

2.4.1 Radiative and non-radiative recombination

When light interacts with a semiconductor (through a linear or a nonlinear process) e-h pairs can be created. The way these e-h pairs successively recombine determines a property specific of each semiconductor, i.e. its luminescence *quantum yield* (QY). The quantum yield Φ measures the efficiency of photon emission from a semiconductor and is defined as the ratio of the number of photons emitted $N_{em}$to the number of photons

absorbed N_{em} :

$$\Phi = \frac{N_{em}}{N_{abs}} \tag{2.22}$$

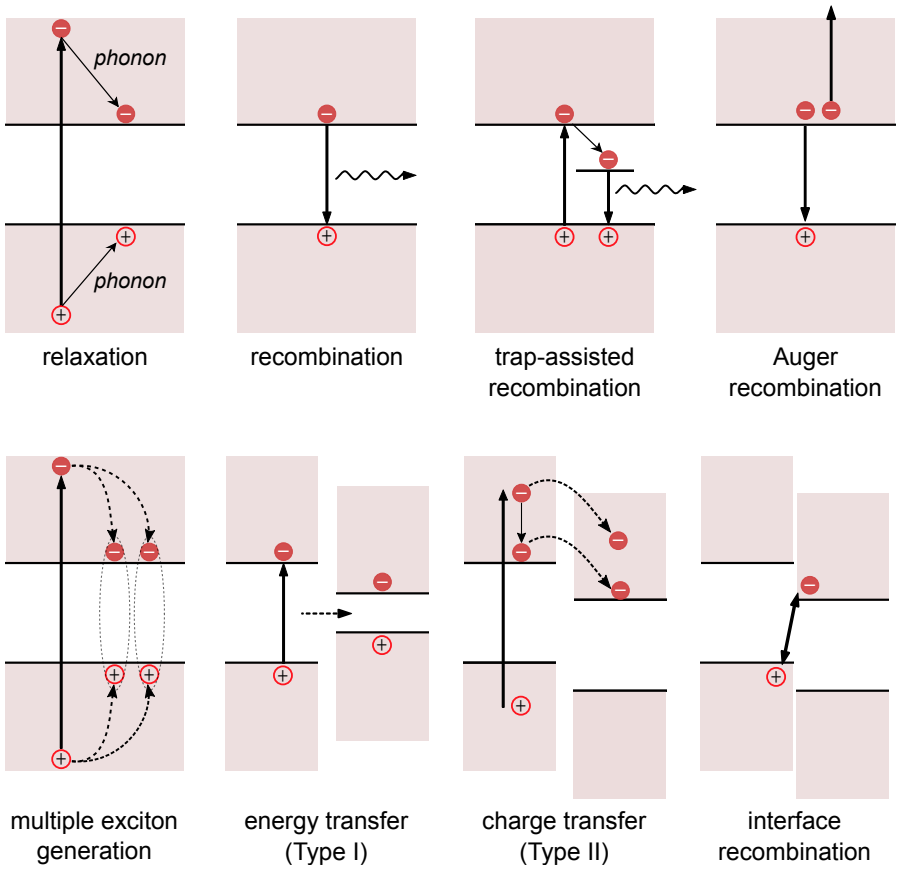

Figure 2.7: Schematic representation of several relaxation and recombination processes in semiconductors. Upon photoexcitation (vertical arrows in the schemes) electron-hole pairs are generated. The recombination of the charge carriers can be either radiative, if it entails the emission of a photon or nonradiative if it involves the emission of phonons instead.

In a semiconductor the relaxation and recombination of the photogenerated carriers can happen through different pathways, as illustrated in Figure 2.7. The electrons and holes can relax to the band edges through interactions with phonons and then from the band edges they can recombine emitting photons. The charge carriers can recombine also by populating a trap-state in the bandgap first or can interact with each other through Auger recombination. Multiple exciton generation, as described in Section

2.3, leads to the generation of more than one exciton through absorption of a high energetic photon.

When different materials are brought together, at the interface between them energy or charge transfer phenomena might take place. In the first case, the energy of the electron-hole dipole is transferred to the material with the proper energy band alignment to accept it (Type I alignment). This band alignment favours recombination of the charge carriers and is mostly used in light-emitting diodes. In the second case, one of the two charge carriers (electron in this case) is transferred to the second material, while the other charge carrier (hole) stay in the material where it was photoexcited. This band alignment is called Type II and favours charge separation (i.e. is mostly used in organic solar cells). The charge carriers belonging to two different materials can also recombine at the interface (interface recombination).

The transition which leads to the recombination of e-h pairs is one of two types:

- radiative;
- non-radiative.

In the first case, it produces a photon with an energy corresponding to the energy difference between the electron at the conduction band edge and the hole at the valence band edge (*band-to-band recombination*). In the second case, the transition does not release any photon, and instead the energy is transferred to other quasi-particles, such as phonons or an additional charge carrier (Auger recombination).

The QY can therefore be defined in terms of the rate constants characterizing the combination of all the radiative (k_{rad}) and the non-radiative (k_{nr}) processes:

$$\Phi = \frac{\Sigma k_{rad}}{\Sigma k_{rad} + \Sigma k_{nr}} \tag{2.23}$$

where the summation is on all rates of excited state decays.

By the definition of QY follows that this value can range from 0% (non-emitting semiconductor) as a minimum to 100% (perfectly emitting semiconductor) as a maximum.

2.5 Light amplification

Light amplification is a process happening when electron-hole pairs recombine emitting more photons than could be absorbed. This is happening if the emission of the material minus the absorption of the material (which defines the *gain* of the material) is a positive number. In this situation the light will be amplified while propagating through the material instead of being damped by it.

In this section, the basic concepts related to light amplification and lasing in semiconductors will be analysed.

2.5.1 Stimulated emission and population inversion

The process that results in the emission of photons in photo-excited semiconductors can be either spontaneous (so-called *spontaneous emission*) or stimulated by an incoming photon (known as *stimulated emission*), as shown in Figure 2.8.

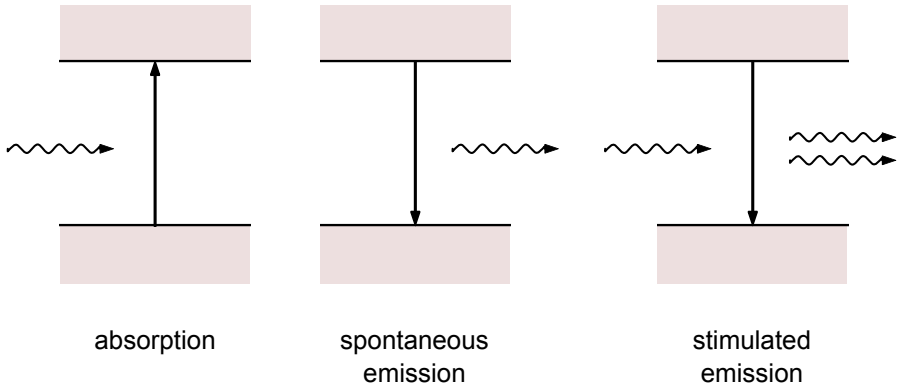

Figure 2.8: Schematic representation of the possible interactions of a photon with a semiconductor. The photon can be either absorbed, leading to the creation of an electron-hole pair, or can be emitted spontaneously due to the recombination of the electron-hole pair. If the system is already in an excited state, then an incoming photon could lead to stimulated emission, meaning that one electron-hole pair recombines and two photons identical to the exciting photons are emitted by the material.

In the first case, the photon emitted has a random spatial direction allowed by the propagation medium surrounding it. The light which is produced by that process is

called photoluminescence[14] (PL). In the second case, the photon emitted has the same properties of the incoming photon (i.e., for one photon impinging on the material, another identical photon is created). Therefore, this process constitutes the basis of light amplification and as such is employed in lasers and amplifiers, and where a good spatial coherence is required.

The variation of the light intensity per unit area I as it interacts with a gain medium can be expressed by the following differential equation:

$$\frac{dI(z)}{dz} = \gamma(\nu) \cdot I(z) \tag{2.24}$$

where z is the light direction of propagation, γ is a function of the light frequency ν and is defined as:

$$\gamma(\nu) = (N_2 - N_1) \cdot \sigma(\nu) \tag{2.25}$$

where N_2 and N_1 are the charge carrier populations in the excited state and in the ground state, respectively, and σ is the absorption cross section of the material. Therefore, the solution of the equation 2.24 strongly depends on the distribution of the charge carriers between the two states N_2 and N_1:

$$I(z) = I(0) \cdot e^{\gamma(\nu)z} \tag{2.26}$$

Light amplification can be strongly attenuated if the semiconductor material has too many regions where charge carriers are in the ground-state levels. If this is the case, indeed, the light amplification can be overcome by the light absorption [40], as these regions are entitled to absorb photons, rather than emit them. Efficient light amplification requires therefore that the number of charge carriers in excited states N_2 is higher than the number occupying ground-states N_1, i.e. $N_2 > N_1$. This requirement is called *population inversion* [39]: When this happens, then stimulated emission can dominate over spontaneous emission and the optical amplification can take place. It is therefore possible to define the *gain* of the analysed material.

This can be summarized as follows:

[14] The rate of spontaneous emission determines the radiative lifetime of the excited level. This is influenced by both the level itself (which defines if the transition to the ground state is allowed, hence fast, or forbidden, and therefore much slower) and by the modes allowed by the surrounding medium.

- if $N_1 > N_2 \longrightarrow \gamma(\nu) < 0$. In this case, $\gamma(\nu)$ is the intrinsic absorption coefficient α and equation 2.24 corresponds to the Beer-Lambert law (see equation 2.8).
- if $N_1 = N_2 \longrightarrow \gamma(\nu) = 0$. In this case, the material is defined optically transparent, as the absorption events equal the stimulated emission events.
- if $N_2 > N_1 \longrightarrow \gamma(\nu) > 0$. In this case, $\gamma(\nu)$ is the optical gain per unit length g and the light is amplified in the direction of propagation.

Therefore, optical gain is obtained when, at a specific light frequency ν, the absorption coefficient α turns negative after photoexcitation. In this case, the system exhibits net stimulated emission and $-\alpha = g$ corresponds to the material gain.

Applying the Maxwell-Boltzmann statistics to the number of atoms in each state, it follows that population inversion can never exist for a two-level system at thermal equilibrium: $N_2/N_1 = exp - (E_2 - E_1)/(kT)$, where 1 refers to the ground state and 2 to the excited state. The maximum inversion for this system is when $N_1 = N_2$, which corresponds to the phenomenon of optical transparency.

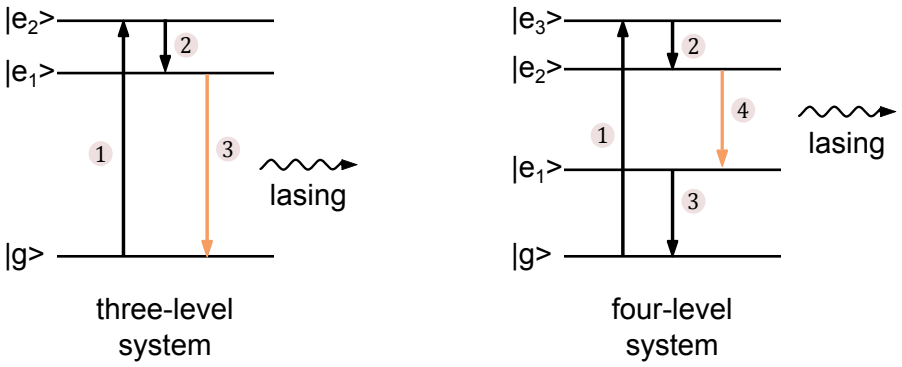

Figure 2.9: Schematic representation of three- (left side) and four-level (right side) lasing systems. The population inversion happen between the levels $|e_1\rangle$ and $|g\rangle$ in the first case and between the levels $|e_2\rangle$ and $|e_1\rangle$ in the second case.

To bring the system into a non-equilibrium state, a different method to populate the excited state must be used. This can be achieved with a N-level system (where $N \geq 3$). In Figure 2.9 the energy diagrams for three- and four-level systems are illustrated. The photon ① is, in both cases, the pumping laser which leads the charge carriers to an excited state. In the three-level system (left side), the transition ② between the two excited states $|e_2\rangle$ and $|e_1\rangle$ is fast and radiationless (i.e., $|e_2\rangle$ is short-lived). In such a

way, it is possible to build the population inversion between the states $|e_1\rangle$ and the ground state $|g\rangle$. ③ is the lasing transition, where stimulated emission takes place.

In the four-level system (right side), the population inversion is between the levels $|e_2\rangle$ and $|e_1\rangle$, hence ④ is the lasing transition. Correspondingly, ② and ③ are fast non-radiative transitions that allow a quick population of the level $|e_2\rangle$ and a fast depopulation of level $|e_1\rangle$, respectively.

2.5.2 Optical resonators and lasing

A semiconductor laser[15] is a device that emits collimated light coherently, by amplifying the stimulated emission from a gain material. It consists of a gain medium where the population inversion is taking place and a cavity supporting the amplification of radiation. The gain medium needs to be "pumped", i.e. it needs to be supplied with a sufficient amount of external energy necessary to promote charge carriers from the ground level to excited levels. This can happen either optically or electrically [39].

The simplest example of cavity for optical amplification is constituted by the *Fabry-Pérot* cavity. This consists of two opposing plane-parallel mirrors embedding the gain material between them, as shown in Figure 2.10. Once the gain material is led to population inversion, the spontaneous emission starts to be amplified inside of the material. The energy of this amplified radiation corresponds to a negative absorbance ($\alpha < 0$) of the material, hence a net stimulated emission overcoming it. The radiation emitted by the gain material is then interacting with the cavity. The length of the cavity L defines the modes of radiation that are allowed to travel inside of it:

$$2L = q\lambda \tag{2.27}$$

where q is an integer.

The modes associated to these frequencies interfere constructively with the reflected photons and are multiples of the fundamental frequency of the cavity ν_f, which is defined as:

$$\nu = q\frac{c}{2L} = q\nu_f \tag{2.28}$$

Instead, the photons that are not supported by the cavity will interfere destructively with their mirrored radiation and will not contribute to the optical amplification.

[15] The acronym *laser* stands for: "Light Amplification by Stimulated Emission of Radiation".

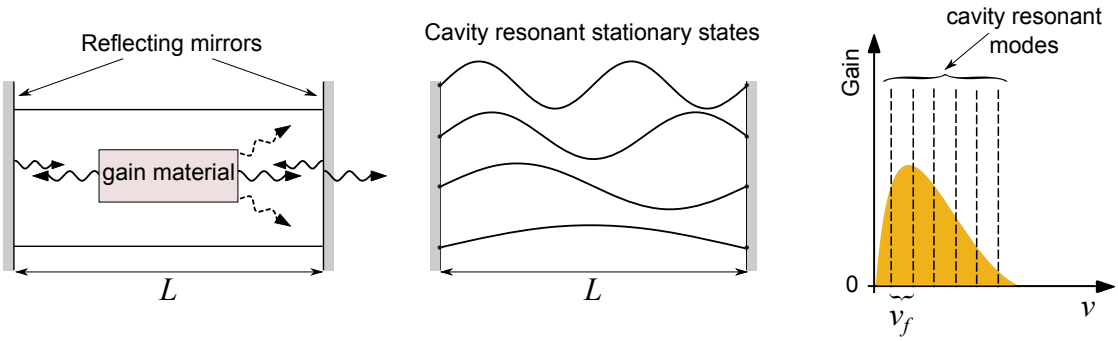

Figure 2.10: A typical Fabry-Pérot cavity (left side) representing the amplification process through a gain material. The stationary states which are resonant with the cavity (middle) are the only ones surviving inside of it. The resulting light emission (right side) is given by the overlay of the cavity resonant modes with the material gain spectrum, in the case in which the material gain is higher than the cavity loss. The emission spectrum narrows even further when a few modes start to dominate among the others.

Another possible cavity configuration is the one constituted by a concave surface, within which the optical radiation can travel around and be amplified. One important requirement for this structure is that its size is at least as big as the wavelength of light which needs to travel in it. In this case, the lasing process is called *whispering-gallering mode*[16] (WGM) lasing. The light waves are guided inside of these structures by optical total internal reflection, which takes places at their boundaries due to the mismatch between the refractive index inside the structures (high) and the one beyond (low).

For a given resonator, many whispering-gallery modes are possible (see Figure 2.11). Each mode can be associated with a number M which represents the number of wavelengths that can travel within the cavity. The criteria for resonance (and therefore light amplification) is given by:

$$2\pi nR = M\lambda_R \tag{2.29}$$

where n is the refractive index of the resonator, R is its radius and λ_R is the resonant wavelength.

Lasing could be also be achieved by multiple scattering events in a disordered amplifying medium. These events lead to light confinement in the gain material and produce optical feedback similarly to the mirrors in a Fabry-Pérot cavity. This process is commonly referred to as *random lasing*, since the energy of the photons to be amplified

[16]This process is named after the whispering gallery of St Paul's Cathedral, where this effect was originally discovered with sound waves by Lord Rayleigh in 1878 [41].

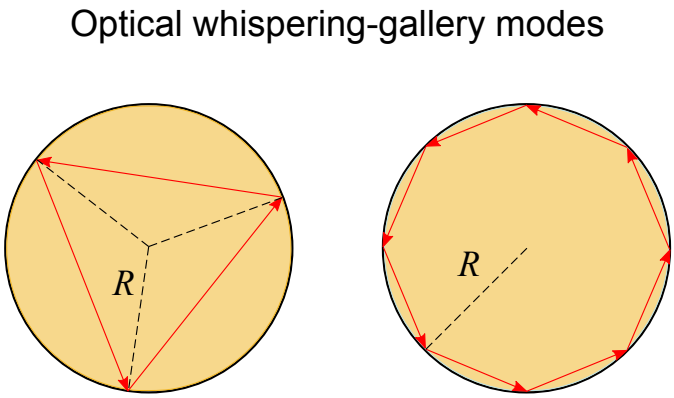

Figure 2.11: Schematic of the constructive interference in a whispering-gallery mode resonator. The two resonant modes $M = 3$ (left side) and $M = 8$ (right side) are illustrated.

differs for every excitation pulse. When these events lead to a "closed loop" of the emitted light, i.e. the last photon being emitted is scattered back to the position where the first photon originated, then spikes can be observed in the laser output, similarly to the case of WGM lasing.

Continuous wave and pulsed lasers

A laser can emit light either continuously, and in that case it is called *continuous wave* (CW) laser, or in pulses with a well-defined duration and intensity (*pulsed laser*). The continuous output of a CW laser is due to the fact that the modes supported by the cavity have random phases with respect to each other. This generates an approximately constant total output intensity over time.

To obtain a pulsed laser, it is fundamental that the phases of the amplified beams inside the cavity are locked. In such a way, periodical constructive interference between the different modes can be observed over time, which leads to high intensity pulsed beams with a certain periodicity. The technique that sets the phases inside the laser cavity is called *mode-locking*.

2.5.3 Amplified spontaneous emission and waveguiding

Amplified spontaneous emission (ASE) is the process by means of which spontaneously emitted photons are amplified through stimulated emission in a material. It therefore generates light which is characterised by a low temporal coherence as amplification is

started by several photons which are emitted spontaneously, i.e. with different phases. However, it has a good spatial coherence being the amplification process strongly directional.

In fact, since amplification in ASE is independent of the presence of a cavityit, it mainly requires gain materials where waveguiding is particularly favourable (see Figure 2.12). Waveguiding enables to confine the light emitted through spontaneous emission inside the gain material for a longer time (i.e. for a higher number of interactions with the material). In such a way, the interfaces air-material and material-substrate create a sort of optical resonator which makes light amplification in the direction parallel to the light propagation possible.

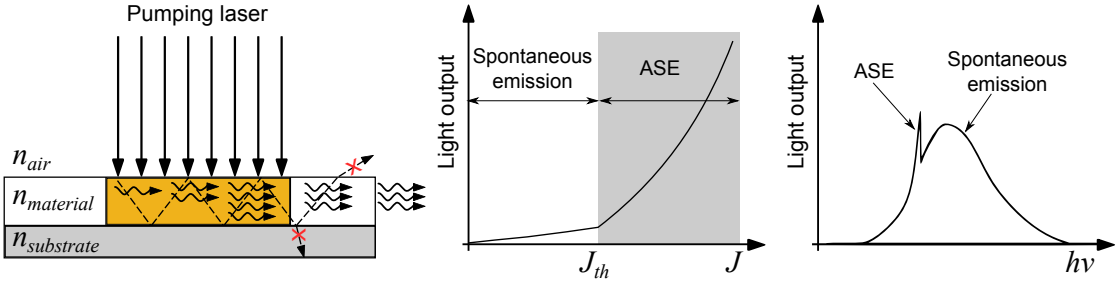

Figure 2.12: Schematic representation of the light amplification through ASE processes (left side). The pumping laser excites the material and, if the amplification exceeds the losses, ASE can be detected. The light output is plotted versus the incident current density (middle). Above the threshold current density J_{th} stimulated emission dominates over spontaneous emission. The light output versus photon energy (right side) shows the typical narrowing of the photoluminescence due to ASE.

The condition for an optimal waveguiding inside the gain material is that [39]:

$$n_{material} > n_{air}, n_{substrate} \tag{2.30}$$

where $n_{material}$ is the refractive index of the gain material, which has to be higher than the refractive indexes of air (n_{air}) and of the supporting substrates ($n_{substrate}$) to make total internal reflection inside the gain material possible.

When ASE dominates over spontaneous emission, a typical threshold-behaviour is observed in the light output of the active material (see the middle graph in Figure 2.12). While below the threshold current density J_{th} the PL of the material increase linearly with the excitation intensity, above this threshold the dependence becomes superlinear.

This is a sign of the amplification process, which is also evident in the spectral dependency of the PL spectrum (see graph on the right side in Figure 2.12). The presence of ASE is manifested there by the appearance of a second peak, much narrower than the spontaneous emission linewidth. The energy of such a peak corresponds spectrally to the region where gain overcomes losses in the active material. The reason for the peak narrowing and for its superlinear growth above the threshold can be explained considering the "winner-takes-all" dynamics of the interplaying optical modes [42].

In this thesis, ASE is observed and characterized for a system of perovskite nanocrystals. The semiconductor class of lead halide perovskite nanocrystals is introduced and examined in the following section. The effect of the photoexcitation energy is discussed in Chapter 5, where above- and below-bandgap photons are used to obtain population inversion. Furthermore, the effect of the nanocrystals arrangement is discussed in Chapter 6, where electronically coupled nanocubes are compared to their isolated counterparts. In both studies, a picture to describe light amplification is developed.

2.6 Lead halide perovskite nanocrystals

2.6.1 Lead halide perovskites - from discovery to reborn

With the name *perovskites* it is common to identify the class of compounds characterized by the same stoichiometry as calcium titanate ($CaTiO_3$), hence ABX_3. This mineral was the first one being named perovskite, after its discovery in the Ural Mountains by Gustav Rose in 1839. The mineral was named after Lev Perovski, a Russian mineralogist.

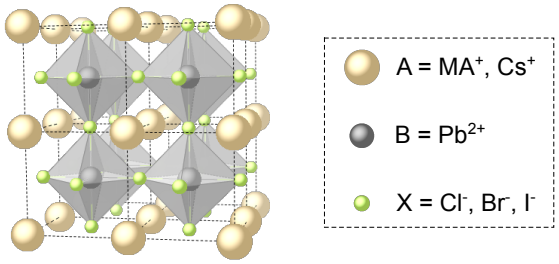

Figure 2.13: Crystal structure of lead halide perovskites. The A cation (MA^+ or Cs^+) is surrounded by PbX_6 octahedra, where X can be either chlorine (Cl), bromine (Br), iodine (I) or a mixture of these.

In lead halide perovskites (LHPs), A and B are two different cations, where A is bigger in size and can be either an organic molecule such as methylammonium ($CH_3NH_3^+$, which can be abbreviated as MA) or an inorganic element such as cesium (Cs). Either way, the big cations A in the perovskite structure are caged by 3D-corner-sharing BX_6 octahedra surrounding them, where B is typically lead (Pb)[17]. The X anions are bond to both A and B cations. They are placed in the octahedra corners and can be either iodine (I), bromine (Br), chlorine (Cl), or a mixture of these (see Figure 2.13).

After their discovery, perovskites became newly popular after the work of Kojima et al. in 2009, where organometal halide perovskites were used as sensitizers for photovoltaic cells [44]. In this work, the authors could achieve a power conversion efficiency (PCE) of 3.81% (measured under AM 1.5 simulated sunlight irradiation) with $MAPbI_3$-sensitized TiO_2 solar cells. This value was significantly high in comparison

[17]Recent studies are trying to investigate possible ways to substitute the heavy metal Pb(II) in the perovskite structure with less toxic options, such as, among others, silver (Ag(I)), bismuth (Bi(III)), germanium (Ge(II)) and tin (Sn(II)). Although much progress in the field has been made, the current lead-free perovskites are still characterized by lower efficiency and poorer stability with respect to their lead-containing counterparts [43].

to the ones which could be obtained in other dye-sensitized cells [45], and allowed a rise in interest in the LHPs. In only 10 years perovskite solar cells have reached the record PCE of 23% [46], making them the fastest growing photovoltaic technology in history[18].

After further investigations on the possibility to employ LHPs bulk films for solar cell applications (firstly as sensitizers and secondly as the main light absorbers), in 2014 the first report on the synthesis of LHP nanocrystals ($MAPbBr_3$) was published [47]. In this report the authors used for the preparation of the material a certain amount of a long organic chain, called octylammonium bromide (OABr), in addition to the MABr. As the long organic cations could not be incorporated into the perovskite structure due to their size, they functioned as capping ligands, which serve both for interrupting the growth of the particles during their synthesis (thus forming nanoparticles) and for stabilizing them, as described in Figure 2.14.

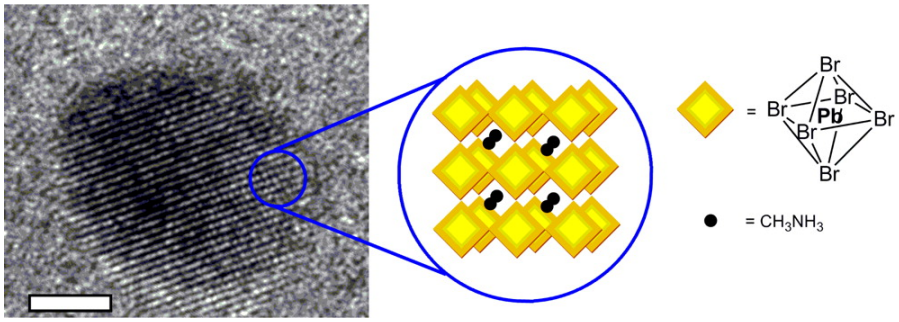

Figure 2.14: TEM image of a single $MAPbBr_3$ nanocrystal. The scale bar is 2 nm. The schematics illustrates the perovskite structure terminated due to organic capping. The figure is taken from [47].

This report paved the way to further studies on the possibility to control the growth mechanism of LHPs in order to synthesise nanocrystals with different geometries, such as nanoplatelets [48, 49], nanocubes [50], nanowires [51] and nanorods [52], to name a few. Reducing the crystal size up to obtaining individual nanocrystals made it possible to exploit quantum confinement effects to finely tune the bandgap and the optical properties of the synthesized materials.

[18] To make a comparison, the development of single-junction GaAs cells with an efficiency up to 29% took nearly 50 years.

2.6.2 Optical properties of lead halide perovskites nanocrystals

LHPs have unique properties which resulted in the great interest they have catalysed in the scientific literature over the last decade. Among them, the ease of synthesis (due to the high ionicity of bondings), the high PL QY that can be obtained without undergoing further electronic passivation, the possibility to tune the absorption and emission through the entire visible spectrum via halide exchange and, even more importantly, the tolerance for defects (mainly due to their shallow nature) [53].

The high PL QY typical of LHPs is primarily due to the fact that they are direct-bandgap semiconductors (see the band structure in Figure 2.15). The bandgap (which occurs at the R point in the Brillouin zone) is generated by the electronic states of the Pb and X atoms, whereas the big cations A do not play a major role there. The valence band (VB) maximum is determined by the hybridization of Pb 6*s* and the X *p*-orbitals (antibonding), whilst the conduction band (CB) minimum is determined by the empty Pb 6p states[19] [54].

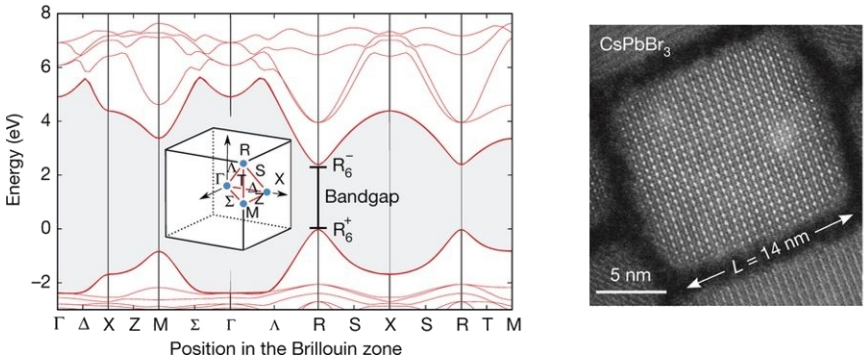

Figure 2.15: Calculated band structure of $CsPbBr_3$ cubic nanocrystals (left side) illustrating the material bandgap located at the R point. The first Brillouin zone is displayed in the inset. TEM image of a single $CsPbBr_3$ nanocube with a side length of 14 nm (right side). The figure is taken from [54].

The absorption onset and PL emission of LHP nanocrystals can be easily tuned by changing either their dimensionality [48] or their halide composition [55]. The latter technique consists in the replacement of the X halide (X = Cl, Br or I), which leads to the shift in PL wavelength from 410 nm (Cl) to 512 nm (Br) to 685 nm (I) in the case

[19] Interestingly, the band structure of LHPs is inverted with respect to that of GaAs, where the VB is determined by 4*p* states and the CB by 4*s* states.

of $CsPbX_3$. This tuning of the bandgap is obtained as a consequence of the shift of the VB edge energy, which is a consequence of the different halide composition. The values in between these extremes could be potentially achieved by using mixed halide components. However, it has been reported that mixed halide systems suffer from phase segregation, which results in a broadening of the PL peak and in a decrease in efficiency and stability [56].

To finely tune the bandgap of LHP nanocrystals it is therefore more advisable to take advantage of their tunable geometry and size, i.e. exploiting quantum confinement effects (see Figure 2.16). These can be nicely observed reducing the dimensionality of the nanocrystals towards the exciton-Bohr radius. In nanoplatelets of $MAPbBr_3$, for example, it was observed that the reduction of the thickness results in a blue-shifted PL from 519 nm (bulk) to 427 nm (monolayers consisting of 1 unit cell) [48].

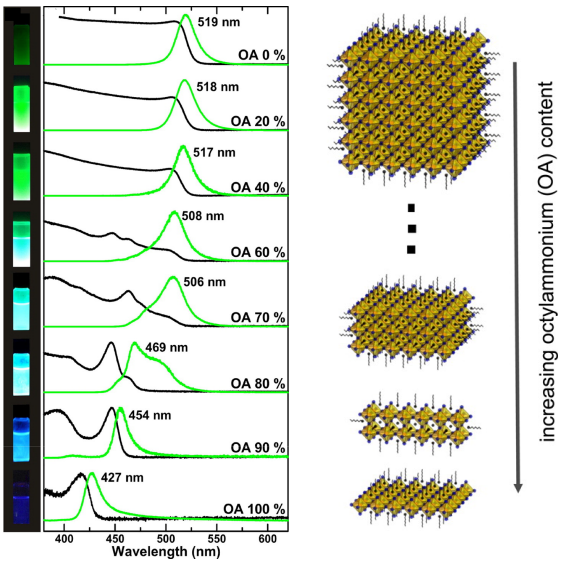

Figure 2.16: Photographs of the suspensions of $MAPbBr_3$ nanocrystals are displayed on the left side. Their color change through increase of OA content is also indicated in the absorption and PL measurements (middle). The increasing OA content induces a thinning of the nanocrystals and therefore an increase in quantum confinement. The figure is taken from [48].

Similarly, when the quantum confinement is released in one dimension, and therefore realised in two dimensions (such as in the case of nanowires), the PL exhibits a red-shift compared to systems which are quantum confined in three dimensions (such as nanocubes) [51].

Another possibility to further play with the bandgap of LHPs is to arrange them into ordered superstructures. When the nanocrystals are close to their neighbours, the wave functions of the individual crystals might overlap. Similar to what happens to atoms nicely ordered into crystal lattices, this coupling results in the splitting of the quantized energy levels of the individual nanocrystals and in the creation of three-dimensional minibands [57]. These coupled structures are called *supercrystals* or *superlattices*. Refining the intercrystal distance, the individual crystals size and the lateral elongation of the supercrystals, it is possible to finely tune their electronic and optical properties.

2.6.3 Multi-photon absorption with lead halide perovskites

LHPs have been reported to exhibit nonlinear absorption and emission in various studies over the last few years [58–63]. High-purity single crystals of $MAPbBr_3$ have been synthesised and their band-to-band PL at 572 nm was reported for below-bandgap excitation by Walters et al. (see Figure 2.17) [58].

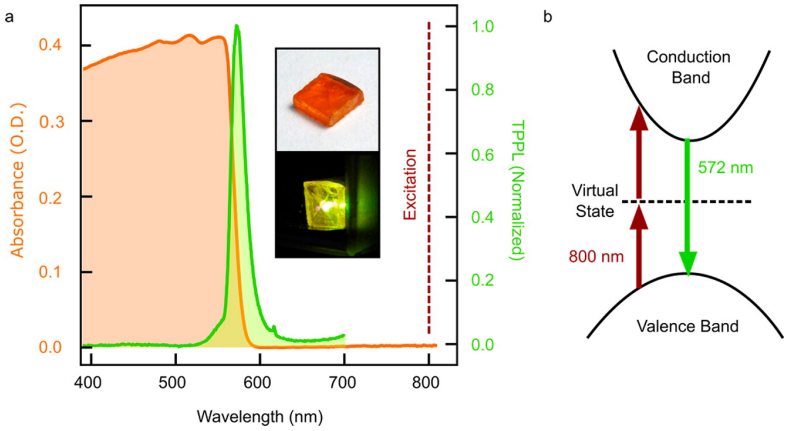

Figure 2.17: On the left side, the linear absorbance and the PL resulting from 2PA are shown for a single $MAPbBr_3$ crystal (see photograph in the inset). The vertical dotted line represents the excitation wavelength used for the 2PA measurements. On the right side, a schematic representation of the band structure illustrating the 2PA and PL processes. The figure is taken from [58].

Nonlinear optical measurements have also been performed in LHPs using the Z-scan technique. This method is based on transmission measurements of one excitation beam for different positions of the sample through the beam focus. Doing this analysis, the nonlinear refractive index (NRI) and the nonlinear absorption coefficient of the

studied sample can be evaluated. To analyse the first one, a narrow aperture has to be placed between the sample and the photo-detector, as illustrated in Figure 2.18. The NRI of $MAPbI_3$ thin films obtained from these measurements is $69 \cdot 10^{-12}$ cm^2W^{-1} for femtosecond laser excitation centred at 1028 nm [59].

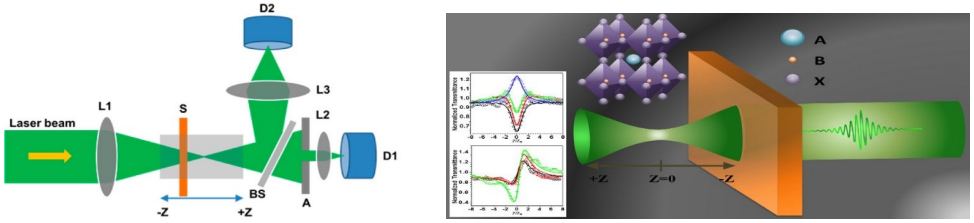

Figure 2.18: On the left side, a schematics of the experimental Z-scan setup is shown. The laser beam is focused with the lens *L1* towards the sample *S*, which position is varied from *-Z* to *+Z*. The transmittance of the sample is divided into two different paths with the beam splitter *BS*, one of which is sent through a closed aperture *A* to measure the nonlinear refractive index. On the right side, the normalized transmittance of $MAPbI_3$ thin films under open-aperture (upper graph) and closed-aperture (lower graph) configurations are shown for different laser pumping intensities. In both cases, the laser wavelength is centred at 1028 nm. The figure is taken from [59].

2.6.4 Multiple excitons in lead halide perovskites

Biexcitons and other multiexciton complexes have been observed in literature for LHPs nanocrystals [64, 65]. Makarov et al. have observed the presence of biexcitonic states in $CsPbX_3$ nanocubes by measuring the recombination dynamics at high pumping intensities (see Figure 2.19) [64]. From this analysis, a biexciton lifetime around 93 ps was reported for these nanocrystals.

Signatures of the interaction between multiple excitons have also been detected by de Jong et al. in transient absorption measurements performed on $CsPbBr_3$ nanocubes (~ 8.6 nm side length) [65].

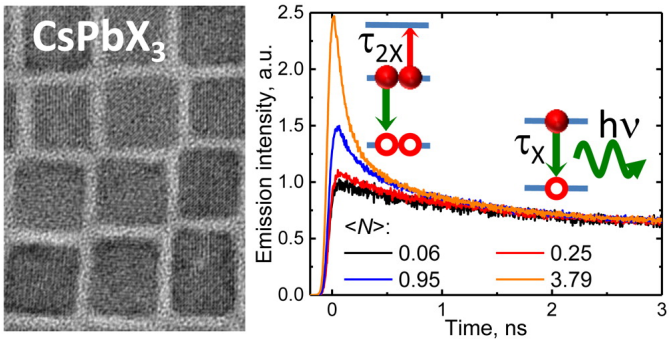

Figure 2.19: On the left side, a TEM image of the $CsPbX_3$ nanocubes with 11 nm as average side length is displayed. On the right side, the PL dynamics of $CsPbI_3$ nanocubes is shown. The early time PL decay component is attributed to biexcitons (leading to Auger recombination), whereas the long time decay component correspond to single-exciton recombination. The figure is taken from [64].

2.6.5 Light-emitting devices with lead halide perovskites nanocrystals

Due to their outstanding optical properties, LHPs were recently investigated not only for their application in photovoltaic [66], but also for light emitting applications [55].

On account of their large absorption coefficients, the slow Auger recombination and the large defect tolerance, LHPs have also been analysed for applications as lasing materials and were found to own high optical gain, along with low thresholds for ASE (see Figure 2.20) [67]. In that report, the measurements were carried on a 65 nm-thick $MAPbI_3$ film and revealed a threshold for ASE of $12 \pm 2\ \mu Jcm^{-2}$ and a gain of about $250\ cm^{-1}$ at a pump fluence of $14\ \mu Jcm^{-2}$.

Recently, ASE under CW photoexcitation has been demostrated in perovskites with a triple cation system [69].

Lasing from individual LHPs nanowires (with a length of a few microns) of $MAPbX_3$ was demonstrated by Zhu et al. at the low threshold of $220\ nJcm^{-2}$ for $MAPbI_3$ nanowires (see Figure 2.21) [68]. In that report, the authors used the smooth end facets of the microcrystals for the creation of a Fabry-perot cavity in the longitudinal axis of the microcrystals themselves. However, these hybrid organic-inorganic LHPs have in common a fast rate of photodegradation.

All-inorganic LHPs have been demonstrated to retain their optical properties for longer time, due to their greater stability [70]. In that work, Yakunin et al. demonstrated

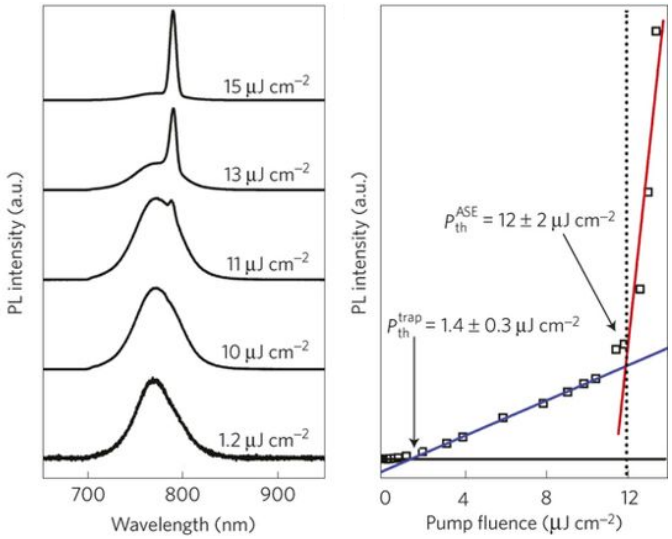

Figure 2.20: PL emission from $MAPbI_3$ films obtained using an excitation source at 600 nm with increasing pump fluence (left side). Plotting the PL intensity versus the pump fluence the onset of ASE is visible around 12 μJcm^{-2}. The figure is taken from [67].

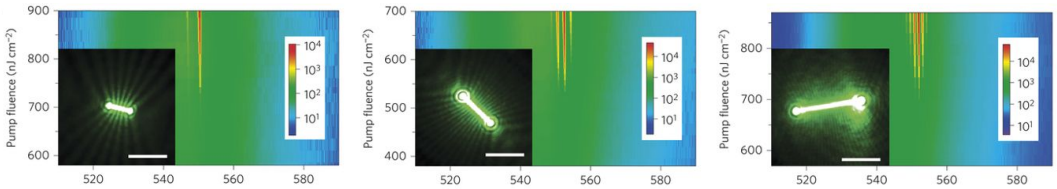

Figure 2.21: 2D plots of the emission from $MAPbBr_3$ nanowires of various lengths (7.5μm (left side), 13.6μm (middle) ND 23.6μm (right side). The scale bars are in all cases 10μm. The figure is taken from [68].

ASE from $CsPbX_3$ nanocubes (X = Cl, Br, I or their mixtures) with a size around 10 nm (see Figure 2.22). The threshold for ASE is in their work down to 5 μJcm^{-2}. Additionally, they have demonstrated that whispering-gallery-mode lasing can be obtained by covering some silica microspheres, which serve as cavities, with LHPs. Random lasing can also be observed in thick films of the nanocrystals.

Moreover, the possibility to obtain multi-photon pumped lasing in LHPs was investigated in literature. Gu et al. demonstrated two-photon pumped lasing from $MAPbBr_3$ microwires with a threshold of 674 μJcm^{-2} using an excitation wavelength of 800 nm with a repetition rate of 1 kHz and a pulse width of 100 fs [71]. Wang et al. have shown ASE from a thin film of close-packed $CsPbBr_3$ nanocrystals under

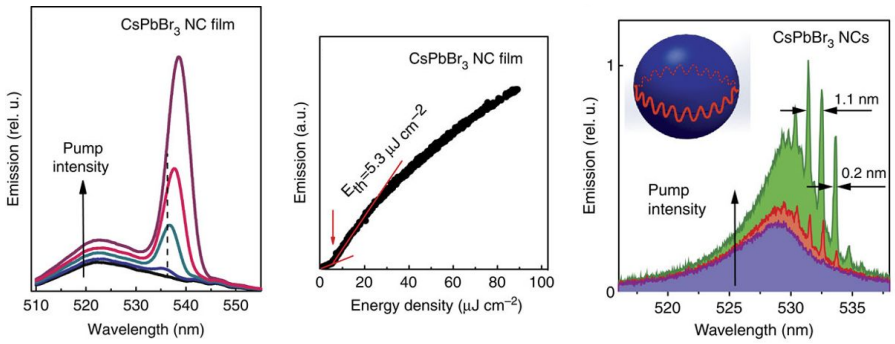

Figure 2.22: On the left side, the emission from a $CsPbBr_3$ film made of nanocubes is shown for various pump fluences varying from 3 to 25 μJcm^{-2}. In the middle, the integrated emission intensity is plotted versus the pumping energy density, indicating a threshold for ASE at 5.3 μJcm^{-2}. On the right side, whispering-gallery-mode lasing peaks are obtained by using a microsphere resonator (15 µm in diameter) combined to the nanocubes. The figure is taken from [70].

two- or three-photon below-bandgap excitation [72]. The threshold for two-photon stimulated emission is reported to be 2.5 $mJcm^{-2}$ at an excitation wavelength of 800 nm, whereas for three-photon stimulated emission (excitation wavelength1250 nm) it is 5.2 $mJcm^{-2}$. In both cases, a femtosecond pulsed laser having a pulse width of 100 fs and a repetition rate of 1 kHz is used as excitation. These reports emphasise the realistic promise for high-efficiency laser devices that is constituted by LHPs.

2.6.6 Lead halide perovskite superlattices

Several different techniques have been reported to successfully form superlattices made of LHP nanocrystals, ranging from the drying mediated self-assembly to the ligand-assisted formation[57, 73–79].

These assemblies can span several degrees of order: from 1D chains of aligned nanocrystals up to 3D superstructures made of interconnected perovskite nanocubes.

Most of the reported assemblies have in common the observation of a redshifted PL emission with respect to the uncoupled nanocrystals. However, different interpretations have been proposed to explain the origin of this shifted PL emission. First of all, the phenomenon of reabsorption could lead to the observation of an apparent red-shift in the PL emission. In fact, the blue high-energy side of the emission could be reabsorbed by the material itself, a process also called photon recycling [80, 81].

Another interpretation of the redshifted PL comes from the consideration of dipole-dipole coupling of excitons in adjacent nanocrystals [82]. Towards this interpretation, it was recently demonstrated that superfluorescence could be observed in $CsPbBr_3$ supercrystals [77]. Superfluorescence is a phenomenon consisting in the emission of a short and intense light pulse from coupled emitters characterized by in-phase dipoles.[83] This observation suggested that dipole-dipole interactions between the emitters constituting the supercrystals could underlie the characteristic red-shifted emission.

In this thesis, as evidence of superfluorescence from the synthesised supercrystals could not be detected, the interpretation of the observed redshifted emission is attributed to the formation of minibands in closely-packed assemblies of LHP nanocrystals. As previously described in Section 2.3.1, the presence of minibands modifies the electronic band structure of the uncoupled nanocrystals. This modification can be modelled, as reported by our group in the case of $MAPbX_3$ nanoplatelets [48], and is observed to be crucial for understanding the optical properties of the reported nanocrystals assemblies [57].

This thesis is divided into 7 distinct chapters. After the introductory chapter and this chapter on fundamentals, the methods used to perform and interpret the experimental data are presented. To follow, three chapters containing the main results and implications of the findings obtained in this work are analysed.

In the first result chapter, "Below-bandgap multi-photon excitation: resonances with multiple excitons", the optical properties of LHP nanocrystals with different composition and geometries are analysed. These materials are used as a test system to move beyond the Shockley-Queisser limit and achieve efficient light conversion into usable power in the energetic regions associated to the major losses. For that purpose, it is reported for the first time that MEG can be achieved through the absorption of multiple photons lying below the bandgap. This process is observed to be very efficient in correspondence of specific resonances, which are dictated by the excitonic energy specific of the analysed material. The novel results of these studies are presented and discussed with specific emphasis on the influence of the close-packing of the analysed nanocrystals towards the achievement of the observed resonance effects.

The second result chapter, "Stimulated emission in perovskite nanocrystals: above- and below-bandgap optical pumping", illustrates the effects of high excitation intensity

on the light emitting properties of the analysed LHP nanocubes. An extremely low threshold for ASE is observed for above-bandgap optical pumping when densely-packed nanocubes are investigated. The nanocrystals in this case spontaneously self-assemble forming the so-called "coffee-rings". Below-bandgap optical pumping is also investigated in this context, and the effect of the above mentioned resonances on the mechanism for population inversion is discussed.

In the third result chapter, "Supercrystals: the effect of electronic coupling in $CsPbX_3$ nanocrystals", ordered assemblies of LHP nanocubes (superlattices), are investigated. For low-excitation intensities the emission of these structures is reported to be red-shifted with respect to their uncoupled counterparts. This phenomenon could be attributed to the formation of minibands, which influences the optical properties of the examined crystals. For high-excitation intensities, a mixture of isolated and electronically coupled nanocrystals is investigated in order to shed light on the mechanism responsible for ASE. As a result, it is shown that the supercrystals provide the feeding mechanism necessary to obtain population inversion in the analysed system, confirming the crucial role of close-packing in the light amplification properties of LHP nanocrystals.

In conclusion, a chapter summarizing the outcome and findings of this thesis work is included.

3 Experimental methods

In this chapter the techniques used to characterize the properties of the analysed samples will be described. The experimental methods involved in this thesis range from sample preparation to characterization techniques.

This chapter will be divided into optical spectroscopy techniques, which were involved in the analysis of the electronic structures, and electron microscopy techniques, which were used to investigate the crystal geometrical properties. Finally, the methods used for the synthesis of the perovskite nanocrystal colloids and films made of well-organized structures will be covered.

3.1 Steady-state optical characterization techniques

3.1.1 Absorption spectroscopy

Absorption spectroscopy is a technique that measures the amount of radiation that, passing through a certain medium, is absorbed by it. This measurement is done as a function of the frequency or wavelength of the radiation interacting with the sample and when this range lays within the ultraviolet (UV)-visible range, it takes the name of UV-Vis spectroscopy.

The most common approach for measuring absorption spectra is based on the measurement of the intensity of a broadband light beam before and after going through the analysed sample. The light passing through the sample and the reference light source are sent to a spectrometer, through which the transmittance of the material can be estimated and resolved versus the energy of the excitation beam. Additionally, the transmittance of an empty cuvette (in the case of colloidal analysis) or of a clean substrate (in the case of solid-state analysis) are analysed and used as baseline to correct the effect of their presence in the material analysis. The absorbance of the analysed material is then calculated from the transmittance using the Beer-Lambert law (see equation 2.5).

In this work, the absorption spectra of either colloidal suspensions or films of LHP nanoparticles were measured using one of the following commercial setups: *Cary 5000* and *Cary 60, Aglient Technologies*. In both cases, a Xenon lamp was used as excitation source.

3.1.2 PL spectroscopy

Photoluminescence spectroscopy measures the intensity of radiation emitted by a material after optical excitation as a function of the emission wavelength. The excitation source for such technique is a monochromatic light beam whose energy is higher than the sample bandgap energy. Ideally, the best excitation wavelength corresponds to a maximum in the absorption spectrum and has some excess energy with respect to the absorption band edge. The excitation is called, in that case, *non-resonant*.

Under non-resonant excitation, it is easy to distinguish between the sample PL and the excitation source, which can be discriminated using an optical filter in the

detection path. On the contrary, resonant excitation (the case where the excitation energy corresponds to the absorption band edge or to the lowest exciton resonance energy, i.e. there is no excess energy) is more challenging. Indeed, in the latter case it is difficult to discriminate between PL and contributions from scattering caused by the excitation energy.

Unlike absorption spectroscopy, PL spectroscopy requires that the detector cannot be placed directly across from the light source axis, to avoid receiving both the transmitted and the PL radiation. Instead, the detector is usually placed at a certain angle θ with respect to the source axis, where $0 \ll \theta \leq 90°$.

In this work, the PL spectra were acquired with one of the following commercial setups: *Cary Eclipse, Aglient Technologies* and *Flurolog 3, Horiba*. In both cases, xenon lamps, equipped with monochromators, were used as excitation sources.

3.1.3 PLE spectroscopy

Photoluminescence excitation (PLE) spectroscopy is a particular type of PL spectroscopy that measures how much the intensity of radiation emitted by a material at a certain energy varies as the energy of the monochromatic excitation beam is varied. Consequently, peaks in the PLE spectrum usually correspond energetically to peaks in the absorption spectrum of the same material. This technique can therefore be used to get information about the electronic levels in a semiconductor, particularly when their transmission is too low to obtain clear results via absorption spectroscopy.

Differences between the absorption spectrum and the PLE spectrum of a certain material can underline the relaxation pathways of the optically excited charge carriers, the possibility for energy transfer between different species and the presence of non-radiative decay channels.

The PLE measurements shown in this work were conducted with a commercial setup from *Horiba* (*Flurolog 3*).

3.1.4 Dark-field spectroscopy

Dark-field spectroscopy is a technique based on a specific optical microscopy technique called *dark-field microscopy*. In this technique, light is coupled into the specimen through a light condenser, which generates a cone of light. This cone of light is focused onto the specimen surface, where it can get transmitted, absorbed, reflected and scattered.

Light is then collected by an objective with a numerical aperture[1] which is smaller than the one of the condenser (see scheme on the left side in Figure 3.1).

Additionally, the objective lens is placed in the dark hollow of the transmitted cone of light, which does not enter the small numerical aperture objective. In such a way, only the light scattered by the specimen will be collected and used to construct the image of the sample. Unscattered light is, instead, excluded from the analysis and therefore the field around the specimen appears dark.

This microscopy technique is particularly useful to obtain high contrast images of the specimen and it allows the identification of individual nanoparticles with sizes even below the diffraction limit through the visualization of the light scattered by them.

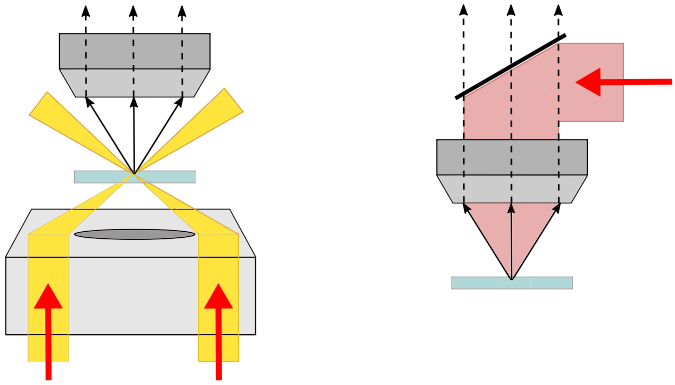

Figure 3.1: Schematics of the dark-field illumination setup (left side) used for locating the nanoparticles to be measured. The excitation with the supercontinuum laser is provided through the top-illumination scheme (right side). The PL from the nanocrystals is then collected upwards and sent to a CCD spectrometer. The red arrows represent the excitation source, whereas the black arrows represent the detected signal.

In this work, dark-field microscopy was performed using a commercial upright microscope (*Axio Scope.A1 HAL 100/HBO, ZEISS GmbH*). To this microscope, a supercontinuum laser[2] (*SuperK EXTREME, NKT Photonics*) was coupled through the back

[1]The numerical aperture (NA) characterizes the maximum angle over which the system can spread or collect light. It can be defined considering the refractive index n of the medium where the lens is working and the angle α which is the biggest half-angle that can enter or exit the lens: $NA = n \cdot \sin\alpha$.

[2]Supercontinuum lasers are based on a series of nonlinear optical processes (such as self-phase modulation, Raman scattering, phase matching and solitons) that act together to obtain a significant spectral broadening of the optical pulses which are originating them. As a result, a spectrum as broad as a typical lamp spectrum can be obtained, while maintaining the high intensity and spatial coherence typical of lasers.

of the microscope body and used as an alternative excitation source (see scheme on the right side in Figure 3.1).

In the case of illumination with the laser beam, the illumination path was therefore passing through the same objective used for light collection. The laser beam, before reaching the microscope, was passing through an acousto-optic tunable filter (AOTF)[3], to obtain monochromatic light over a wide spectral range (*SUPERK SELECT, NKT Photonics*). An appropriate notch filter was then positioned in the detection path of the microscope to block the specific laser wavelengths to prevent from imaging them.

3.1.5 ASE spectroscopy and VSL measurements

Amplified spontaneous emission (ASE) was measured in the analysed materials using a femtosecond pulsed laser with a pulse width of 100 fs and a repetition rate of 1 kHz as excitation source. The laser wavelength employed for excitation was either 800 or 400 nm, where the latter was obtained by frequency doubling the fundamental wavelength (800 nm) of the laser source (*Coherent Inc.*) through the use of a beta barium borate (BBO) nonlinear crystal.

The excitation was directed perpendicularly towards the substrate covered by the LHP nanocrystals following reflection from a proper dichroic mirror, while the PL obtained was transmitted through the same dichroic mirror and collected in the backward direction of the laser beam (see path #1 in Figure 3.2). The collected signal was then sent to a fiber-coupled CCD spectrometer (*Thorlabs*) to resolve the PL intensities over wavelength. A complementary metal-oxide semiconductor (CMOS) camera (*Thorlabs*) was used to estimate the size of the laser beam at the substrate position, fundamental for calculating the beam fluence impinging on it.

The excitation intensity of the laser beam was tuned using absorptive neutral-density filters and the corresponding PL signal was measured dependently.

Perovskite films were prepared by either drop casting or spin coating a few microliters of the synthesised colloidal dispersion of nanocrystals on top of glass substrates.

[3] Acousto-optic tunable filters are electro-optical devices that can modulate the intensity and energy of a laser. They usually consist of a bifrangent crystal, whose diffraction properties depend on the interaction with an acoustic wave. Tuning the acoustic wave, the angle at which a certain optical wavelength is diffracted passing through the crystal changes. Therefore, by placing a slit in a fixed position near to the crystal output, it is possible to select the energy of the monochromatic light that shall pass through it.

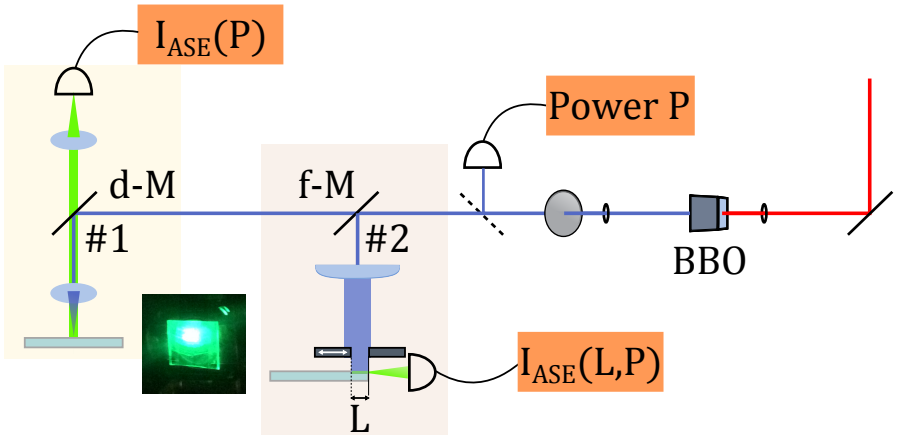

Figure 3.2: Schematics of the setup employed for ASE and VSL measurements. The excitation source at 800 nm is sent through a BBO crystal to obtain a laser signal centred at 400 nm. After the alignment through two pinholes, the laser power is adjusted with a continuously variable neutral density filter wheel. The power of the laser excitation P is monitored by sending 25% of the total power to a power meter. The flipping mirror "f-M" allows to distinguish two different excitation paths: the path #1 is used for vertical photo-excitation and detection of the sample PL and ASE signals as a function of the excitation power $I_{ASE}(P)$. This excitation/detection scheme is obtained by using the proper dichroic mirror "d-M" to discard the excitation signal from the detection path. The path #2 is used for VSL measurements to obtain $I_{ASE}(L, P)$, where the stripe signal is obtained through a cylindrical lens and its length L is controlled through an adjustable mechanical slit. The inset shows a photograph of a substrate with $CsPbBr_3$ nanocrystals deposited on it under frontal laser excitation and detection.

Variable stripe length (VSL) measurements rely on the optical excitation of a well-defined stripe in the analysed material. The stripe is obtained including a cylindrical lens in the optical path of the laser beam (see path #2 in Figure 3.2). The length of the stripe is then changed gradually by opening or closing a metallic slit placed after the cylindrical lens and the photoluminescence of the sample is collected perpendicularly with respect to the excitation. In these measurements the power of the laser is kept constant, as the variable excitation volume is the element of interest.

The VSL technique enables a quantification of the *net modal gain* G of the analysed material, which is defined as the optical gain g minus an overall loss coefficient which is due to the propagation of the radiation in the material. For this quantification the excitation stripe is considered as a one-dimensional optical amplifier. By doing this assumption, it is possible to express the light emission $I(L)$ as a function of the stripe

length L, of the spontaneous emission intensity I_S and of the net modal gain [84]:

$$I(L) \propto \frac{I_S}{G}\left(e^{GL} - 1\right) \tag{3.1}$$

By changing the volume of the material excited, it is possible to measure the minimum amount of material which needs to be excited to obtain optical amplification. When the stripe length is short, the photoluminescence detected is broad. The spectral narrowing of the photoluminescence signal is observed if optical gain is present in the material. If this is the case, the intensity of the photoluminescece increases superlinearly as the stripe length increases. In the absence of optical gain, instead, by increasing the stripe length only a linear increase of the photoluminescence is detected and the *full width at half maximum* (FWHM) of the peaks remains constant.

With respect to the frontal detection of the ASE, this technique enables to test the quality of waveguiding in the analysed material. In fact, the PL signal is detected only after it reaches the edge of the sample, hence after being guided through a big portion of the gain material.

3.2 Structural analysis of nanocrystals

The structural and morphological analysis of the LHP nanocrystals was conducted through various electron microscopy techniques. These are based on the use of an accelerated electron beam as source of interaction with the specimen. This interaction can lead to scattering, transmission and other effects such as ionization (which causes the generation of secondary electrons), emission of X-rays and so on. The analysis of the products generated by the of the result of the interaction between the excitation source and the specimen provides fundamental information on the nature of the investigated material.

The use of electrons as excitation source allows the determination of finer details of the specimen, with respect to what could be achieved with optical microscopy. This relies on the smaller *De Broglie wavelength*[4] of the electrons in comparison with photons, that improves the spatial resolution which can be achieved.

3.2.1 Transmission electron microscopy

Transmission electron microscopy (TEM) is a microscopy technique that can be used to analyse the transmission of ultra-thin specimens. From it, a contrast image can be obtained on a fluorescent screen placed on the opposite side of the electron gun and the specimen. Darker spots on the screen represent thicker regions in the sample, whereas whiter spots correspond to a higher transmission (thinner regions).

With this technique it is possible to achieve images of the analysed sample with nanometric resolution. Using an accelerating voltage of 80 kV, a resolution of around 1 – 3 nm can be reached, whereas increasing the voltage to several hundreds of kV a resolution up to 0.2 nm can be achieved. In the latter case, the microscopy technique takes the name of *high-resolution TEM (HRTEM)*.

In both cases, vacuum is required in the microscope chamber to increase the electron mean free path and avoid interaction of electrons with particles others than the ones

[4]The de Broglie wavelength was introduced in 1924 by the physicist Louis de Broglie to describe the wave-like behaviour of small objects (like electrons), which is typical in quantum mechanics[85]. This quantity is defined as: $\lambda_B = h/p$, where h is the Planck constant and p is the relativistic momentum of the particle. The bigger the particle, the bigger its mass and therefore the smaller the de Broglie wavelength associated to it.

belonging to the specimen. Magnetic lenses are used to focus the electron beam on the specimen.

In these studies, the TEM used for our investigations was a *JOEL JEM-1011*, whereas the HRTEM used was a *Titan Themis, FEI*.

3.2.2 Scanning electron microscopy

Scanning electron microscopy (SEM) is a microscopy technique based on the action of sweeping a focused electron beam across the surface of a specimen and recording the result of this interaction that bounces back in the direction of the electron source. In such a way, it is possible to construct an image of the portion of the surface scanned with a resolution up to a few nanometers.

Being based on scattering rather than transmission, SEM does not require a low thickness of the analysed specimen and can instead be used to analyse thick films and bigger structures. The main requirement for this technique is that the surface of the sample consists of conductive material, to avoid accumulation of electrons close to the excitation spots, that would hinder the achievement of high resolution. This condition can be easily achieved even for non-conductive samples by evaporating a thin layer of metallic compound on top of them. This process was obtained by using a sputtering machine (Sputter Coater EM SCD005, Leica) equipped with a gold-palladium target.

A SEM mainly consists of a column, where electrons are generated, collimated and accelerated, a chamber where the sample is located and several detectors. Also in this case, vacuum is required in both column and chamber to increase the electron mean free path.

In these studies, a *Gemini Ultra Plus field emission* SEM (Zeiss, Germany) with a nominal resolution of ~ 2 nm was used. This instrument is equipped with two different electron detectors: one *in-lens* detector, which measures high-energy backscattered electrons and secondary electrons generated by the irradiation with the primary electron beam (also called as *SE1*), and a *SE2* detector, which collects secondary electrons at a higher angle away from the electron gun axis. The accelerating voltage used for the SEM measurements in this work was in the range 3 – 5 kV.

3.3 Synthesis of perovskite nanocrystals

3.3.1 one-pot synthesis by tip-sonication

Most of the LHP nanocrystals examined in this work were synthesised under ambient atmospheric conditions using a tip-sonication metod. This is a single-step technique where the chemical precursors are inserted, together with the organic ligands and solvent, in a reaction vial and subjected to the effect of vibrations. Similar sonication techniques were formerly used to synthesise metal nanoparticles, until the applicability of this method was extended to the synthesis of LHPs in 2016 by our group [50].

The ultrahigh-frequency vibrations are transmitted from the sonicator probe's tip (which experiences longitudinal expansions and contractions due to the mechanical vibration of an internal piezoelectric crystal) to the solution containing the ingredients for the formation of perovskites. In the liquid, the energy created by the tip vibration creates microscopic bubbles that carry a high energy and lead to the heating of the reaction medium. Under proper settings of the amplitude and power of the tip vibration it is possible to drive the chemical reaction that leads to the formation of LHP nanocrystals:

$$Cs_2CO_3 + Pb\mathbf{X}_2 \longrightarrow CsPb\mathbf{X}_3 \tag{3.2}$$

In the case of $CsPbX_3$ nanocrystals (X = Cl, Br, I or mixtures of them), the following precursors were involved in the chemical reaction (see equation 3.2): Cs_2CO_3 and PbX_2, which were added to oleic acid and oleylamine (both serving as ligands) and 1-octadecene (used as nonpolar solvent). The concentration of the precursors can be varied, together with the reaction conditions, to obtain crystals with different shapes and compositions.

The formation of LHPs is quickly observed after the beginning of the tip-sonication process due to the change of color of the reaction medium. By illuminating the vial with UV light, it can also be observed that the solution starts emitting PL as the tip-sonication process advances. The increase in PL intensity over time is an indication of the formation of smaller nanocrystals in solution, with a higher PL QY than bulk LHPs.

One of the benefits of the tip-sonication method is its scalability. It is indeed possible to increase the amount of precursors and still obtain LHP nanocrystals with the same

optical properties obtained in a small-scale synthesis. This high yield of the reaction enables a facile and time-effective production of the desired nanocrystals [50].

The obtained solution right after sonication consists of a mixture of LHPs nanocrystals, but also of unreacted precursors and excess ligands. To obtain a clear dispersion of LHPs consisting of a uniform morphology and size-distribution, further purification steps are required as described below:

1. At first, the obtained solution is centrifuged with a speed of 8000 rpm[5] for 10 minutes to remove the excess ligands in the supernatant, and then the sediment is dispersed in hexane;

2. The obtained colloidal dispersion is further centrifuged at 5000 rpm for 10 minutes to remove big particles in the sediment, while the supernatant is kept. By changing the centrifugation speed, the desired mass (and therefore size) of the nanocrystals is selected.

Amount of precursors

Depending on the amount of chemical precursors involved in the ultrahigh-frequency tip-sonication technique, the outcome of the reaction could be changed drastically. For this thesis work two different LHP structures were synthesised: nanocubes and supercrystals (the latter being made of ordered assemblies of the first ones). The recipes for the preparation of both nanostructures are reported in Table 3.1.

Precursors for $CsPbX_3$...	nanocubes	supercrystals
1-octadecene [ml]	10	10
oleic acid [ml]	0.5	1.5
oleylamine [ml]	0.5	1.5
Cs_2CO_3 [mmol]	0.1	1
PbX_2 [mmol]	0.3	3
reaction time [min]	10	30

Table 3.1: Amount of precursors for the synthesis of $CsPbX_3$ nanocubes and supercrystals [50, 57].

[5]The unit of measurement used to express the centrifugation speed is rpm, which stands for "revolutions per minute". This is to be referred to the centrifuge used in these studies (*Eppendorf Centrifuge 5810 R*).

3.3.2 Hot-injection synthesis

Samples consisting of a mixture of isolated $CsPbBr_3$ nanocubes and supercrystals were obtained following the hot-injection synthesis method described by Rainò et al. [77]. In this case, the supercrystals were obtained by slow evaporation of solvent from a liquid droplet consisting of highly monodisperse $CsPbBr_3$ nanocubes.

The nanocubes were synthesised in a three-neck flask by dissolving $PbBr_2$ in 1-octadecene for 30 minutes at 100°C using oleic acid and oleylamine as ligands. The pre-synthesised caesium oleate (CsOL) is in the meantime dispersed in 1-octadecene (0.4 ml) and heated up as well. When the temperature is reached, the CsOL is injected in the $PbBr_2$ solution and the reaction is quenched immediately afterwards by placing the reaction flask in an ice bath. The obtained colloidal solution appears in green-yellow color and shows bright green PL under UV excitation.

The purification steps can be summarised as follows:

- The obtained solution is centrifuged with a speed of 1200 rpm for 5 minutes to remove the excess ligands in the supernatant. The sediment is then dispersed in 300 µl of hexane;
- The obtained dispersion is then centrifuged once more with a speed of 1200 rpm for 5 minutes. This time, the supernatant is kept and subsequently dispersed in 300 µl of hexane.

The amount of precursors involved in this synthesis is reported in Table 3.2.

Precursors for $CsPbBr_3$ nanocubes	
1-octadecene [ml]	5
oleic acid [ml]	0.5
oleylamine [ml]	0.5
caesium oleate (CsOL) [M]	0.125
$PbBr_2$ [mmol]	0.188

Table 3.2: Amount of precursors for the synthesis of $CsPbX_3$ nanocubes [77].

4 Below-bandgap multi-photon excitation: resonances with multiple excitons

As illustrated by the Shockley-Queisser limit, the main sources for energy losses in solar energy conversion are due to (i) below-bandgap photons that are not interacting with the material and (ii) above-bandgap photons that loose their excess energy through interaction with phonons (heat).

The two approaches that can be employed to overcome these two limitations in single p-n junction cells have been analysed in Chapter 2: (i) multi-photon absorption, which allows to absorb more than one low-energy photon simultaneously in order to overcome the bandgap and (ii) multiple exciton generation, that converts the excess energy of high energetic photons into more than one electron-hole pair.

These two processes have only been studied independently in the previously published work. In this chapter, the interaction of these processes in $CsPbX_3$ LHPs nanocrystals is reported for the first time.

The effect of the interaction between multi-photon absorption and multiple exciton generation is identified by the appearance of resonances. This discovery opens new pathways for a more efficient conversion of solar energy into usable power in semiconducting materials.

4.1 $CsPbBr_3$ nanocubes: linear optical characterization and structural analysis

The LHPs analysed for this study are mainly $CsPbBr_3$ nanocrystals in the forms of nanocubes (NCs). The validity of the reported results is then extended to other halide compositions ($CsPbI_3$) and other nanocrystal shapes.

The nanocrystals are synthesised following the ultrahigh-frequency tip-sonication technique reported in Section 3.3.1. From the TEM analysis, they appear cubic in shape with sides 10 – 15 nm long on average (see Figure 4.1 b).

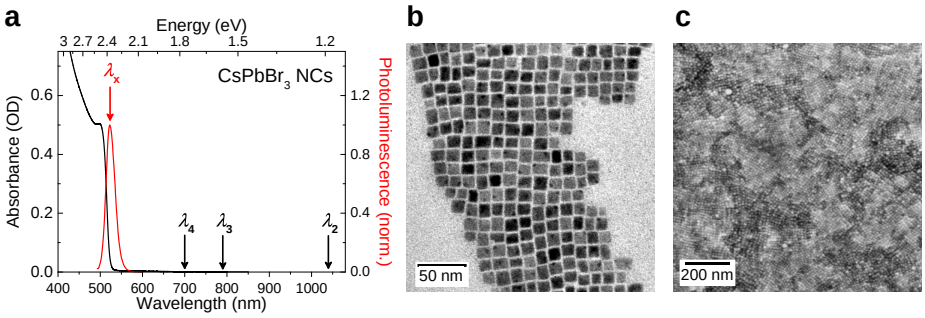

Figure 4.1: **a** Absorbance (left axis) and PL (right axis) of $CsPbBr_3$ NCs in hexane and on a glass substrate, respectively. **b** TEM image of the NCs, scale bar 50 nm. **c** SEM image of the NCs on substrate showing the close-packed arrangement, scale bar 200 nm. This figure is taken from [86].

The linear UV-Vis spectrum is characterised by a sharp absorption peak at 500 nm, with a clear excitonic nature. Additionally, the intensity of absorption for excitation energies below the bandgap (i.e. for wavelengths longer than ~ 510 nm) is appreciably negligible (see Figure 4.1 a). This indicates the absence of linear absorption from hypothetical states lying within the bandgap.

For further investigations, 300 µl of the NC dispersion is drop-casted on borosilicate glass substrates (side length 24 mm) in order to create a dried film from the dispersion of NCs. Interestingly, the SEM analysis of these films reveals that the NCs spontaneously assemble into ordered superstructures upon drying (see Figure 4.1 c). The PL of these films is centred around λ_x = 523 nm, which corresponds to an energy $E_x = h\nu_x$ = 2.37 eV.

4.2 Multi-photon absorption in $CsPbBr_3$ perovskites nanocubes

The nonlinear absorption properties of the $CsPbBr_3$ NCs are analysed by illuminating a defined area of the nanocrystal films with a focused supercontinuum laser (pulse length ~ 15 ps). The setup used for these measurements is described in Section 3.1.4. The repetition rate of the laser used for excitation is chosen to be 78 MHz, whereas the wavelength is tuned across the range 680 – 1080 nm, where the linear absorption of the material is close to zero.

The PL of the sample is then collected through the same objective used for excitation (100x magnification, NA 0.75 epiplan-neofluar objective, Carl Zeiss Microscopy) and sent to a CCD coupled spectrometer. The reflection of the laser signal is removed from the detection path by using an appropriate band-pass filter.

For all the excitation wavelengths in the range investigated, a PL signal can be detected (see inset in Figure 4.2), confirming the presence of an absorption process of nonlinear origin. Interestingly, the PL energy and FWHM do not change with respect to the excitation wavelength selected and resemble nicely the PL obtained for excitation ennergies above bandgap.

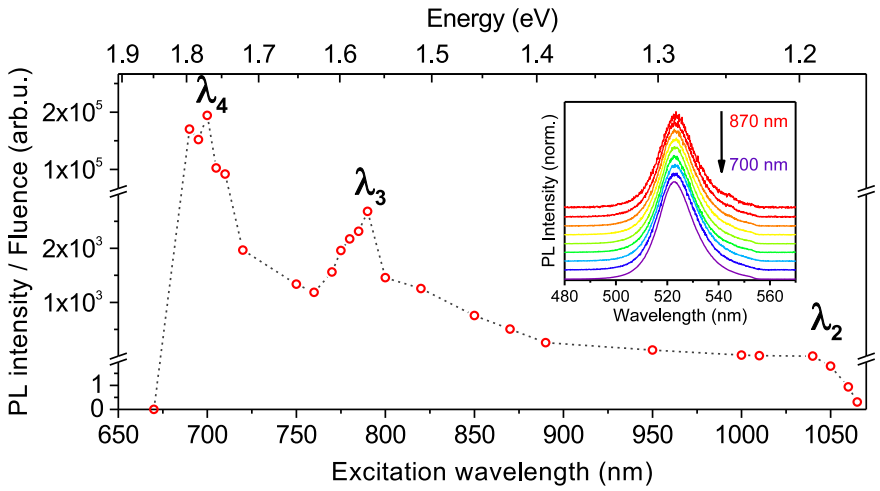

Figure 4.2: PL intensity of $CsPbBr_3$ NCs as a function of the below-bandgap excitation wavelength. The PL intensity is divided by the laser fluence for normalization purposes. The inset shows the normalized PL spectra for excitation wavelengths in the range 870 – 700 nm. The image is adapted from [86].

Instead, the PL intensity depends dramatically on the excitation wavelength chosen (see Figure 4.2). The trend is represented by a general increase of PL intensity as the excitation wavelength decreases. This increase is not monotonic in nature, but rather it is possible to identify two distinct peaks (noted in the graph with the letters λ_3 = 790 nm and λ_4 = 700 nm). The PL intensity associated with these two specific excitation wavelengths is several orders of magnitude higher than the PL detected at wavelengths away from these two peaks.

Additionally, an onset for PL can be observed around λ_2 = 1030 nm, indicating that for wavelengths longer than this value the PL intensity gets too low to be distinguished from the noise level in our setup. On the opposite side of the graph, an abrupt decrease of the PL intensity can be observed for excitation wavelengths shorter than 680 nm.

4.2.1 Relation between efficient multi-photon absorption and multiples of the exciton energy

From the PL data illustrated in Figure 4.2 it is possible to assess that the nonlinear process of multi-photon absorption (and the subsequent radiative recombination process associated with it) becomes particularly efficient in close proximity to the specific excitation wavelengths λ_3 and λ_4.

Interestingly, it can be observed that the energy associated to photons of such wavelengths, i.e. $h\nu_3 = 1.57eV$ and $h\nu_4 = 1.77eV$, respectively, perfectly match the energy of fractions of the exciton energy $E_x = h\nu_x = 2.37eV$:

$$h\nu_3 \simeq \frac{2}{3}E_x \quad \text{and} \quad h\nu_4 \simeq \frac{3}{4}E_x \tag{4.1}$$

which implies that:

$$3h\nu_3 \simeq 2E_x \quad \text{and} \quad 4h\nu_4 \simeq 3E_x \tag{4.2}$$

This correlation suggests a possible connection between two physical processes: multi-photon absorption (MPA), on the one hand, multiple exciton generation (MEG) on the other. In fact, the energy of three photons corresponding to the wavelength λ_3 is exactly enough to generate two excitons rather than one and, analogously, the absorption of four photons corresponding to λ_4 can generate three excitons.

The possible combination of MPA and MEG is illustrated schematically in Figure 4.3. The creation of more than a single exciton per absorption event can explain the observed increase in PL efficiency corresponding to the excitation wavelengths λ_3 and λ_4, assuming a high rate of radiative recombination for these excitons.

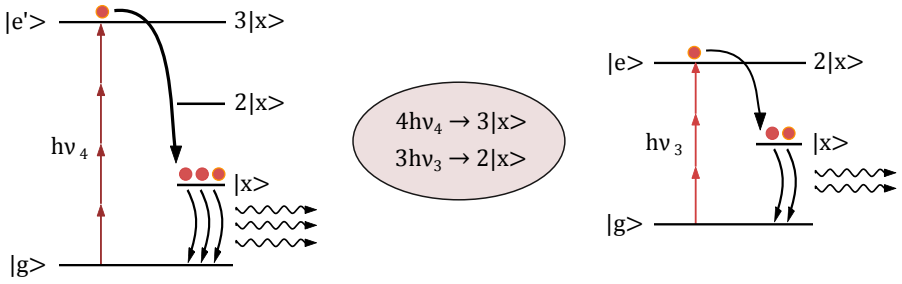

Figure 4.3: Schematic of the combined MPA-MEG mechanism, where below-bandgap photons are used to generate multiple excitons. The scheme on the left side illustrates the process of 4-photon absorption leading to the generation of 3 excitons, whereas the one on the right side illustrates a 3-photon absorption leading to 2 excitons. This figure is taken from [86].

Similar remarks may be made about the observed onset, which is associated to the wavelength λ_2 ($h\nu_2 = 1.20$ eV). In this case, the following relation holds:

$$2h\nu_2 \simeq E_x \tag{4.3}$$

which implies that the absorption of two photons with such an energy would have the minimum energy to overcome the bandgap and generate a single exciton. MEG is therefore not possible in correspondence to λ_2, motivating the absence of a peak associated to this transition in Figure 4.2.

Furthermore, photons with a longer wavelength than λ_2 need to undergo a nonlinear absorption process involving at least three photons to overcome the bandgap. This explains the reduction in PL intensity observed for longer wavelengths and the origin of the onset.

4.3 Order of the multi-photon absorption process

In order to evaluate the order of the nonlinear multi-photon absorption process, and hence verify the matching with the proposed model, the dependency of the PL intensity versus the fluence of the excitation laser is recorded. The order of the absorption process p can be evaluated by fitting the resulting data points with a power law function, as:

$$I_{PL} \propto (I_{exc})^p \tag{4.4}$$

where I_{PL} and I_{exc} are the PL and the excitation intensity, respectively.

As described in Section 2.2.2, for $p > 1$ the absorption process can be defined as nonlinear and the system experiences a simultaneous absorption of p photons via $p - 1$ virtual states.

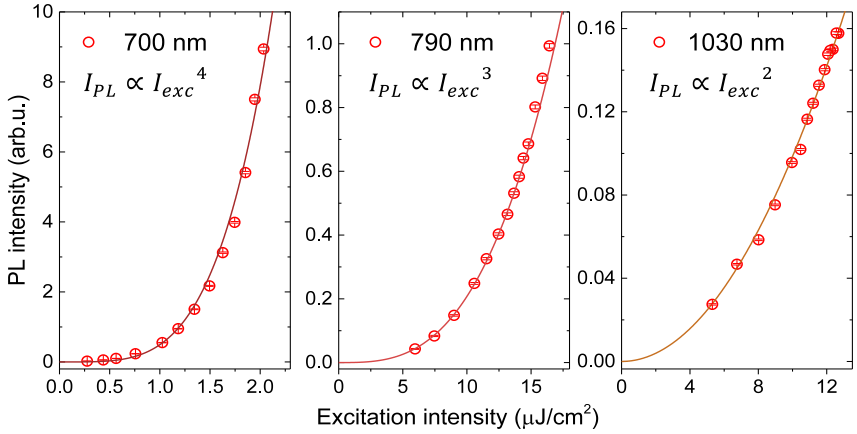

Figure 4.4: Integrated PL intensity as a function of the laser fluence at a specific excitation wavelength (700, 790 and 1030 nm, respectively). The solid lines are fit with power functions, indicating the order of the absorption process of 4, 3 and 2, respectively. This figure is adapted from [86].

The results obtained for the three remarkable cases constituted by λ_4, λ_3 and λ_2 are illustrated in Figure 4.4. It can be observed that the excitation at 700 nm (i.e. λ_4), nicely match with a fourth-order process, while at 790 nm (i.e. λ_3) the process is of third order and at 1030 nm (i.e. λ_2) of second order.

The picture introduced in the previous section (see Figure 4.3) is therefore in full accordance with the experimental results reported here.

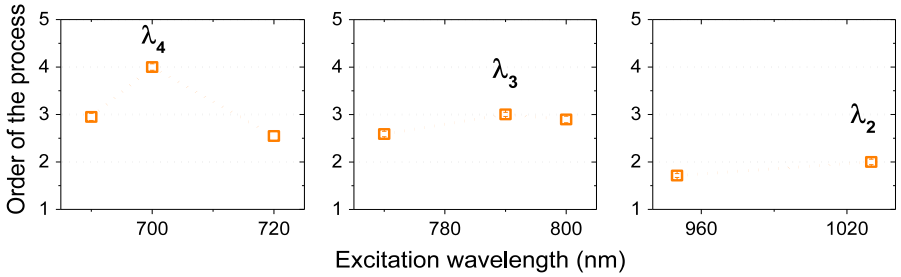

Figure 4.5: Order of the absorption process with respect to different excitation wavelengths. This figure is adapted from [86].

The order of the absorption process was measured for excitation wavelengths away from the observed remarkable positions as well (see Figure 4.5). Interestingly, an increase in the order of absorption can be observed in correspondence to the increase in PL intensity associated to λ_4 and λ_3. In between these wavelengths, the order of the absorption process decreases rapidly to 2, indicating a typical two-photon absorption process.

This suggests that the specific behaviour observed at λ_4 and λ_3 is due to the presence of resonances between MPA and MEG, which are indeed necessary to promote the high order of the nonlinearity.

4.3.1 Analysis of the energy levels

The analysis of the order of the nonlinear absorption reveals the mechanism behind the MPA and the number of photons involved in it. With this knowledge, a more accurate analysis of the energy levels employed in this process can be carried out.

When the wavelength λ_4 is used as excitation, 4-photon absorption takes place (see Section 4.3). The sum of the energies of these 4 photons leads to the energy level at 7.08 eV, which is resonant with $3E_x$ = 7.10 eV (see Figure 4.6 a).

On the other hand, when λ_3 is used as excitation, 3-photon absorption takes place. It follows that the photogenerated transition has a total energy of 4.71 eV, which is resonant with $2E_x$ = 4.73 eV (see Figure 4.6 b).

From this analysis it is possible to understand the drop of the PL signal to almost zero for excitation wavelengths below 680 nm in Figure 4.2. In fact, at these wavelengths an hypothetical 4-photon absorption process would lead to energies in excess of 7 eV,

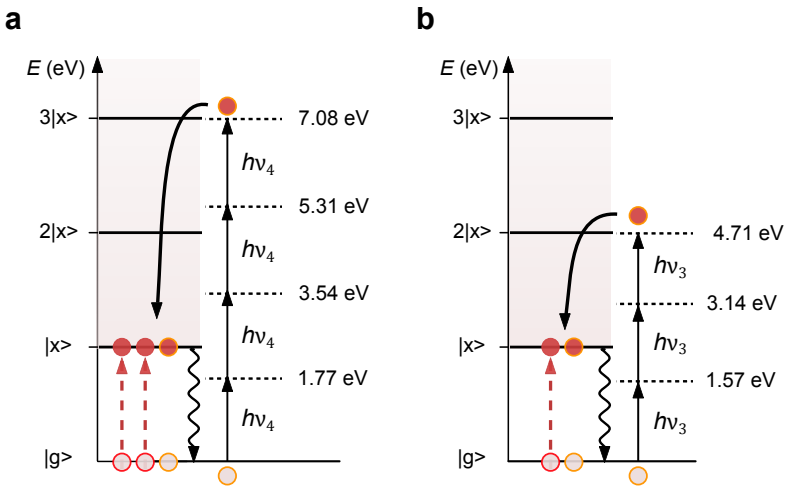

Figure 4.6: Energy diagram of $CsPbBr_3$ NCs and their MPA-MEG resonances. **a** Photoexcitation at $3E_x$ obtained through 4-photon absorption. **b** Photoexcitation at $2E_x$ obtained through 3-photon absorption. This figure is taken from [86].

which can induce photoemission of electrons out of the NCs and hence open a new non-radiative decay channel.

4.4 MPA-MEG resonances

It has been shown in Sections 2.2 and 2.3 that the conditions for MPA and MEG to take place are, respectively:

i there is a high density of incoming photons, which can be absorbed in groups of p if: $phv \geq E_x$, where hv is the energy of a single photon and E_x is the exciton energy of the material;

ii the photons absorbed have an energy as high as a multiple of the exciton energy: $hv \geq NE_x$, where N is the number of excitons that can be generated through this absorption process.

All the investigations conducted so far on $CsPbBr_3$ NCs indicate that there is a particular condition under which the appearance of the observed MPA-MEG resonances takes place. This is related to the fulfilment of the following relation:

$$phv = NE_x \tag{4.5}$$

When the resonance condition is satisfied, the energy exchange between overtones of the fundamental excitation energy hv and multiples of the exciton energy E_x is particularly favourable and, as a result, both processes become more efficient. The PL intensity of the nanocrystals increases under this condition and distinctive peaks appear (see Figure 4.2).

Upon closer inspection, also the shape of these peaks resembles the typical non-symmetrical form attributed to resonances (see Figure 4.2). On the right side of the peaks it is possible to observe a rapid decrease in the PL intensity, which is due to the lower energy of the excitation photons that does not suffice the energy required for MEG.

Interestingly, on the left side of the peaks the efficiency of the PL emission decreases as well. This is an indication that the interplay between MPA and MEG is particularly favourable when the resonant condition is strictly fulfilled, i.e. no additional excess energy is provided to the system.

4.5 Requirements for the observation of MPA-MEG resonances

To exclude that the observed phenomena are strictly related to the material investigated, control experiments have been performed on LHP nanocrystals with different halides (such as $CsPbI_3$ NCs), different dilutions and on $CsPbBr_3$ nanocrystals with different geometries.

4.5.1 The influence of the halide composition

$CsPbI_3$ NCs are synthesised through an ion exchange reaction [51] from the originally prepared $CsPbBr_3$ NCs (see Section 3.3.1 for more details on the synthesis) in order to preserve their size and shape (see Figure 4.7). The exciton energy is in this case E_x = 1.81 eV, indication of a redshifted absorption onset and PL with respect to the Br containing NCs. The size and arrangement on the substrate are kept the same as in the case of $CsPbBr_3$ NCs.

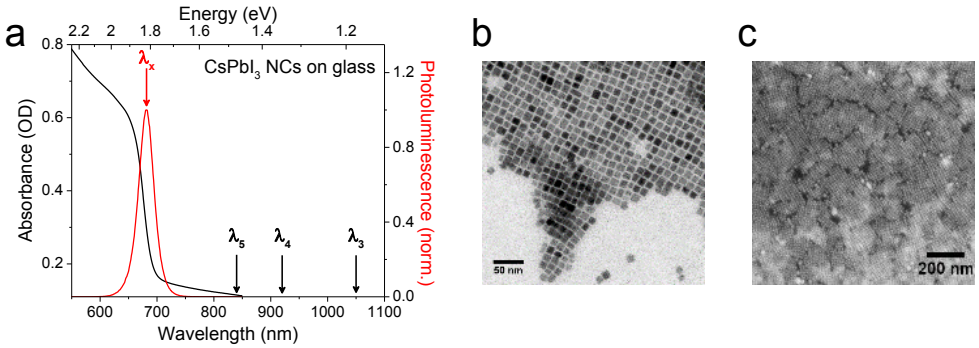

Figure 4.7: **a** Absorbance and PL spectra of $CsPbI_3$ NCs on substrate. The PL spectrum obtained through excitation at 450 nm is centred around 682.5 nm, i.e. E_x = 1.81 eV. **b** TEM image of $CsPbI_3$ NCs, scale bar 50 nm. **c** SEM image of $CsPbI_3$ NCs nicely arranged on substrate, scale bar 200 nm. This figure is taken from [86].

The results on $CsPbI_3$ NCs confirm the presence of the resonances observed in their Br- counterparts (see Figure 4.8). As the exciton energy is smaller than the one for $CsPbBr_3$ NCs, the spectral position of such resonances redshifts as well. The position

of the resonances can be still described with equation 4.5, supporting the notion that the proposed mechanism is not based on a specific characteristic of $CsPbBr_3$ NCs.

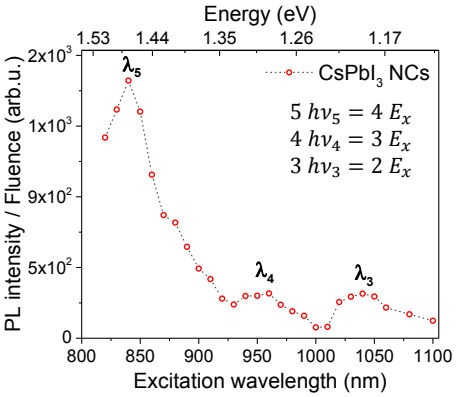

Figure 4.8: PL intensity of $CsPbI_3$ NCs as a function of the below-bandgap excitation wavelength. The PL intensity is divided by the laser fluence for normalization purposes. The resonances are centred around the energy $h\nu_5$ = 1.47 eV, $h\nu_4$ = 1.32 eV, $h\nu_3$ = 1.20 eV, respectively. This figure is taken from [86].

4.5.2 The influence of close-packing

In contrast to the negligible influence of the halide composition in the experiments reported so far, the degree of close-packing in the nanocrystal films seems to be crucial for the observation of MPA-MEG resonances.

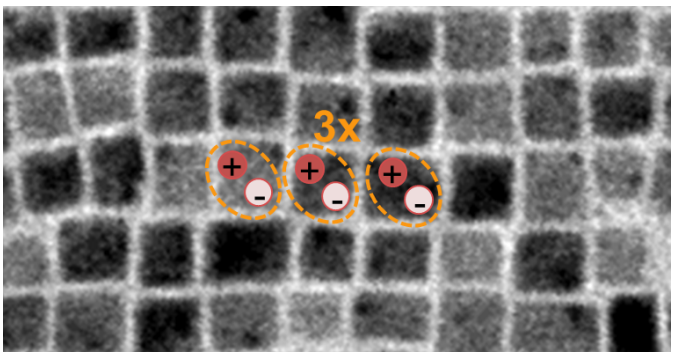

Figure 4.9: TEM image of $CsPbBr_3$ NCs with the schematics for the process of 3-exciton generation in adjacent nanocrystals.

In fact, when the NCs are measured while dispersed in solution, MPA-MEG resonances could not be recorded under comparable laser excitation intensities. This hints towards the necessity to have a close-packed arrangement of nanocrystals to observe these resonances.

The reason for this observation can be connected to the suppression of Auger recombination due to the spatial arrangement of the nanocrystals, as discussed in Section 2.3.1. In fact, Trinh et al. reported that close-packing of nanocrystals is the key element to suppress Auger recombination, which is subsequent to the generation of multiple excitons [35]. Indeed, when multiple excitons are generated in an isolated nanocrystal, the probability for them to interact with each other non-radiatively through Auger recombination is high, as it scales with N^3 (N being the number of charge carriers interacting with each other).

Instead, when the nanocrystals are close enough to each other, their wavefunctions overlap and the multiple excitons generated through MEG can spread over adjacent nanocrystals (see the sketch reported in Figure 4.9). In such a way, the probability of Auger recombination is highly reduced and in turn radiative recombination is strongly enhanced. This model can also explain the increase of PL efficiency that corresponds to the proposed resonances.

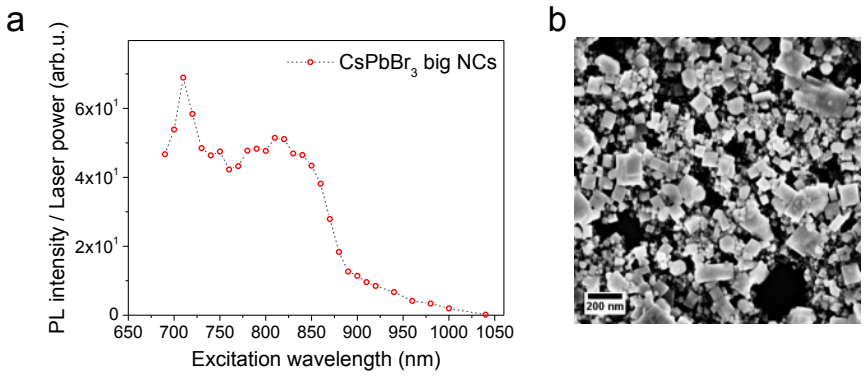

Figure 4.10: a PL intensity of $CsPbBr_3$ NCs with a side length around 100 nm as a function of the below-bandgap excitation wavelength. The PL intensity is divided by the laser fluence for normalization purposes. **b** SEM image of the $CsPbBr_3$ NCs on substrate, scale bar 200 nm. This figure is taken from [86].

To confirm the need for a closely-packed arrangement, larger $CsPbBr_3$ NCs are also investigated. In these cubes the edge sizes are in the order of 100 nm. The arrangement

on a glass substrate does not present the order and symmetry characteristic of the smaller and more monodisperse NCs (see Figure 4.10 b).

From the below-bandgap excitation measurements, an enhanced PL can be observed in vicinity of the expected resonances, which appear (if present) significantly weaker in intensity and broadened, probably due to the relatively large size distribution of the crystals (see Figure 4.10 a). The weak intensity of these resonances can be due to the higher degree of Auger recombination, which is not suppressed in this case.

4.5.3 Applicability of MPA-MEG resonances for solar energy conversion

In order to reveal whether these findings are feasible for solar applications, the degree to which solar light would have to be focused down to reach the fluences used in this work is estimated. Typical fluences used in these experiments are in the range of $1\,\mu Jcm^{-2}$ at the resonance of $CsPbBr_3$ at 700 nm, obtained with a laser having a pulse duration of 15 ps. Therefore the laser irradiance is in the order of: $I_{laser} = 6.7 \cdot 10^4\ Wcm^{-2}$.

Being the solar irradiance at AM1.5 about $I_{sun} = 0.12 \cdot 10^{-3}\ Wcm^{-2}$, to reach the same irradiance used in the setup for these experiments one would need to focus a $1\,cm^2$ area of solar light down to $1\,\mu m^2$.

Due to the diffraction limit, the minimum spot size that can be obtained at 700 nm is, with a numerical aperture $NA = 1.6$, equal to $0.15\,\mu m^2$. This is one order of magnitude smaller than what needed, suggesting that the proposed resonances can be employed to improve the efficiency of solar energy conversion using solar concentrators.

5 Stimulated emission in perovskite nanocrystals: above- and below-bandgap optical pumping

Lead halide perovskite (LHP) nanocrystals are promising materials for optoelectronic applications. This is mainly due to their ease of synthesis and the possibility of obtaining nanocrystal dispersions with a high degree of monodispersity. Due to their high PL quantum yields (PLQYs) and narrow PL linewidths, LHP nanocrystals have been analysed for applications in light-emitting devices, such as light emitting diodes (LEDs) and lasers.

In this chapter, the structural and optical properties of $CsPbX_3$ nanocubes are analysed. Further, the effect of a high excitation intensity on the light emitting properties of $CsPbBr_3$ nanocubes is covered. The observation of an extremely low-threshold for amplified spontaneous emission (ASE) in these materials is illustrated, together with a model to target light amplification in the analysed system.

Additionally, below-bandgap excitation is employed to study the effect of nonlinear absorption on the stimulated emission of $CsPbBr_3$ nanocubes. Interestingly, with an excitation wavelength of 800 nm, three-photon absorption is observed to dominate over two-photon absorption, in line with the resonant enhancement of the nonlinearities discussed in Chapter 4.

These observations open new pathways for the application of $CsPbX_3$ nanocrystals in efficient light-emitting devices involving above- or below-bandgap optical pumping.

5.1 Synthesis and optical characterization of the $CsPbX_3$ nanocrystals

The synthesis of the $CsPbX_3$ nanocrystals is based on the ultrahigh-frequency tip-sonication technique, which was examined in Section 3.3.1. Once synthesised, the nanocrystals are purified to remove the excess of ligands and unreacted precursors and redispersed in hexane for further studies. With this one-pot-technique it is possible to obtain colloidal nanocrystals with chlorine, bromine or iodine content (or some combinations of them) by simply changing the precursor salts PbX_2.

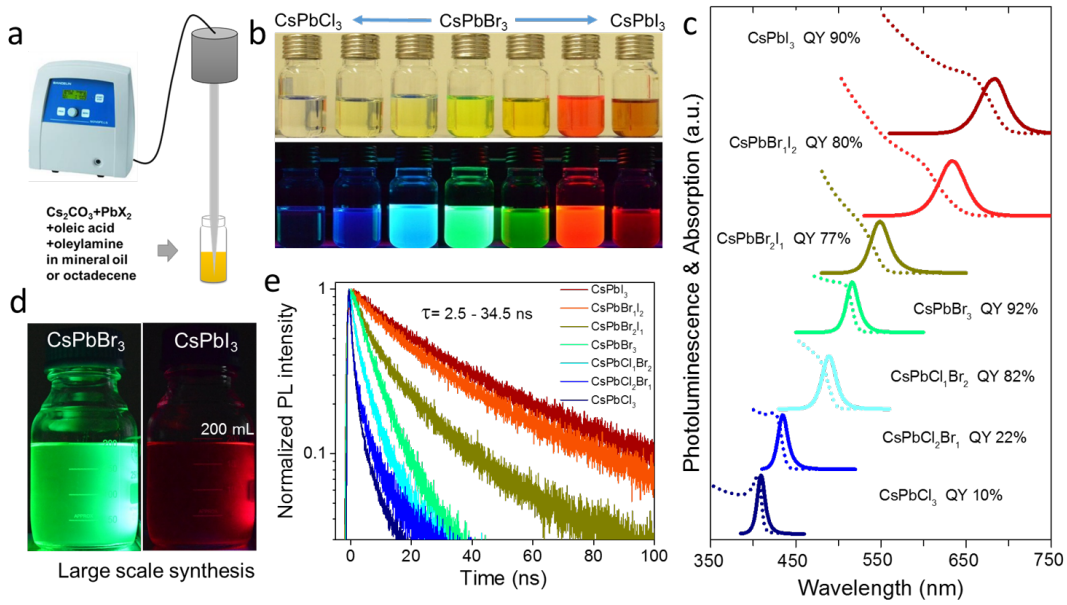

Figure 5.1: Scheme of the synthesis route to obtain $CsPbX_3$ nanocrystals through ultrahigh-frequency tip-sonication (**a**). Photograph of the obtained dispersions under room light and UV light (**b**). Absorption and PL spectra of the so-synthesised $CsPbX_3$ nanocrystals with different halide compositions and the respective PLQYs (**c**). Photograph of the nanocrystals dispersions obtained scaling-up the proposed synthesis route (**d**). PL decay traces of the nanocrystals with different halide compositions (**e**). This figure is taken from [50].

By changing the halide content it is therefore possible to synthesise materials with equal structure and morphology, and yet completely different optical properties. In fact, the absorption and the PL of the LHPs vary from blue to green to red depending

on their halide composition. In Figure 5.1 b this color change is clearly displayed. The upper part of the photograph shows the purified dispersions of $CsPbX_3$ nanocrystals in hexane under room light illumination, whereas the lower picture shows them under UV illumination. The bright colors stem from the high PLQY of the synthesised nanocrystals, while the different tones are an indication of the varying bandgap of the materials.

To characterize the shift of the bandgap energy depending on the halide composition, UV/Vis and PL spectra of the different dispersions are collected (see Figure 5.1 c). The absorption onset varies from ~ 700 nm in the case of $CsPbI_3$ up to ~ 410 nm in the case of $CsPbCl_3$. The possibility to manipulate the optical bandgap of these materials over such a broad range of energies makes them the perfect candidates for optoelectronic applications in the entire visible range.

Furthermore, from the PL of the different compounds it is possible to assess its narrow linewidth. This, together with the almost absent spectral overlap between different-halide-content nanocrystals, is an indication of the purity of the chemical and geometrical composition for each halide-mixture.

In Figure 5.1 e the PL decay curves of the different nanocyrstals are displayed. The PL lifetime changes dramatically depending on the halide composition of the nanocrystals from ~ 34.4 ns in the case of $CsPbI_3$ up to ~ 2.5 ns for $CsPbCl_3$. The PL dynamics seem to be therefore highly correlated with intrinsic properties of the halides constituting the LHPs.

5.2 Structural characterization of $CsPbX_3$ nanocrystals

The structural properties of the synthesised $CsPbX_3$ nanocrystals are mainly obtained through electron microscopy. In Figure 5.2 a and e it is possible to see bright field TEM pictures of $CsPbBr_3$ and $CsPbI_3$ nanocubes, respectively. In both cases, the average crystal sizes are in the range of 8 – 15 nm. The dimension of the nanocubes mainly depends on the duration of the synthetic reaction, as smaller nanocrystals can be obtained by terminating the reaction earlier than what is depicted here.

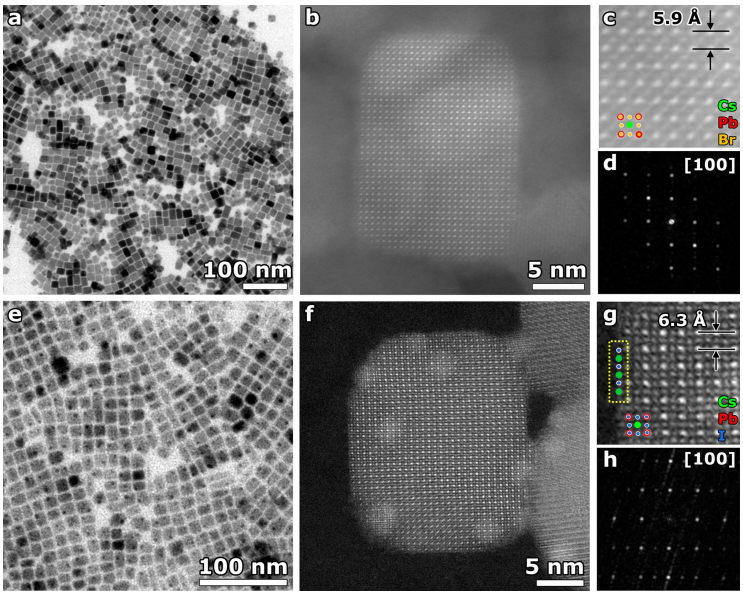

Figure 5.2: Bright-field TEM image of $CsPbBr_3$ and $CsPbI_3$ nanocubes, respectively (**a, e**). HAADF-STEM images of single $CsPbBr_3$ and $CsPbI_3$ nanocubes, respectively (**b, f**). Detailed view of the images displayed in **b** and **f**, respectively, with the position of the single elements obtained from EDX marked with color-coding (**c, g**). Diffractiograms of $CsPbBr_3$ and $CsPbI_3$ nanocubes, respectively, indicating the [100] zone with a single crystalline cubic phase (**d, h**). This figure is adapted from [50].

Figure 5.2 b and f are high angle annular dark field scanning TEM (HAADF-STEM) images of single $CsPbBr_3$ and $CsPbI_3$ nanocubes, respectively. From these images it is possible to assess that, in both cases, the nanocubes are single-crystalline. Additionally, from atomic-resolution measurements along the [100] direction the cubic nature of

the crystal structures appears evident (see Figure 5.2 d and h). The lattice parameter can be measured from this analysis and it results 5.9 Å for $CsPbBr_3$ nanocubes (see Figure 5.2 c) and 6.3 Å for $CsPbI_3$ nanocubes (see Figure 5.2 g).

Additionally, through energy-dispersive X-ray (EDX) spectroscopy the precise location of Cs, Pb, Br and I inside the crystal lattice is obtained (see figure 5.2 c and g). The results confirm the crystal structure expected for these $CsPbX_3$ nanocrystals.

In the following high-intensity optical pumping experiments, the $CsPbBr_3$ nanocrystals are measured after being drop-casted on glass substrates. A typical SEM image of the film obtained is shown in Figure 5.3. The close-packed arrangement of the nanocubes given by the spontaneous formation of the so-called *coffee-rings* is shown in the figure.

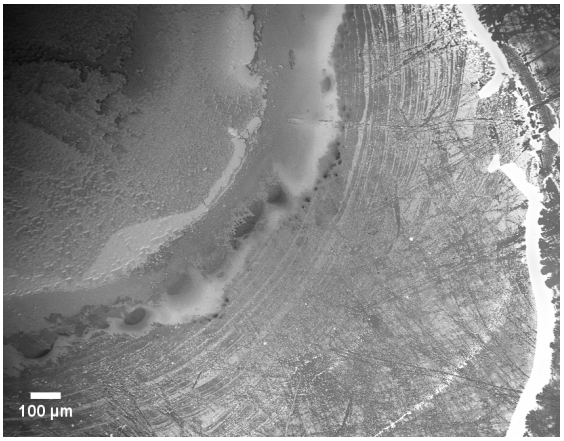

Figure 5.3: SEM image of $CsPbBr_3$ nanocubes drop-casted on a glass substrates showing the typical coffee-ring configuration. Scale bar 100 µm.

5.3 Above-bandgap high intensity photoexcitation

The high PLQYs of the synthesised $CsPbBr_3$ nanocrystals indicate them as possible candidates for light emitting applications. To test the possibility to obtain population inversion in these materials, high intensity photoexcitation is applied to them.

The setup employed for these studies consists in a femtosecond-pulsed laser centered around 400 nm. The configuration of the photoexcitation experiment is described in Section 3.1.5.

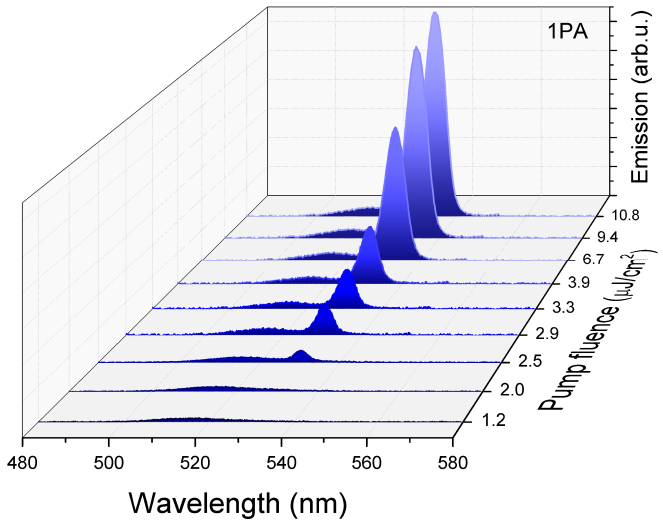

Figure 5.4: 3D plot of the pump fluence-dependent PL emission and ASE from $CsPbBr_3$ nanocubes drop-casted on a glass substrate. The excitation wavelength is 400 nm. This figure is adapted from [50].

The $CsPbBr_3$ nanocubes are analysed in drop-casted films of their dispersions, which (as already discussed in Section 4.1) spontaneously form close-packed arrangements. The distribution of the nanocrystals on the substrate is expected to be crucial for the observation of ASE, as waveguiding effects play a fundamental role in the propagation and amplification of light. The effect of close-packing and electronic coupling on the light emission and amplification of $CsPbBr_3$ nanocubes is examined in detail in Chapter 6.

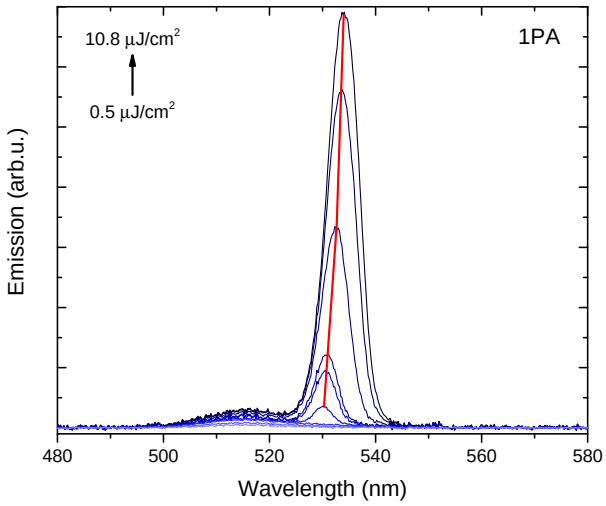

Figure 5.5: 2D plot of the pump fluence-dependent PL emission and ASE from $CsPbBr_3$ nanocubes drop-casted on a glass substrate. The excitation wavelength is 400 nm. The laser fluence is varied from 0.5 up to 10.8 μJcm^{-2}. The red line is a guide to the eye indicating the redshift of the ASE peak as the pumping fluence increases.

In Figure 5.4 the PL emission obtained through vertical photoexcitation (see Section 3.1.5) of the $CsPbBr_3$ nanocrystals on substrate is displayed for different pump fluences. While for low pumping intensities the normal PL band centred around 516 nm is obtained, at higher laser powers the emergency of a new, narrow peak is observed on the low-energy side of the PL spectrum. This narrow emission indicates the presence of ASE in the illuminated area of the nanocrystals.

From a 2D plot of the same data set (see Figure 5.5) it is possible to assess that, while the position of the PL peak remains constant around 516 nm, the position of the ASE peak redshifts from 530 nm to 534 nm as the pump fluence increases. This phenomenon can be explained with a bandgap renormalization model, where the exchange interactions between the high number of electrons being added to the conduction band result in a decrease in energy of the conduction band minimum, together with an increase in energy of the valence band maximum [50]. This effective shrinkage of the material bandgap under the effect of high population of the energy level denominated for population inversion is reversible and vanishes when the pump fluence is decreased to lower values, i.e. the state is promptly depopulated.

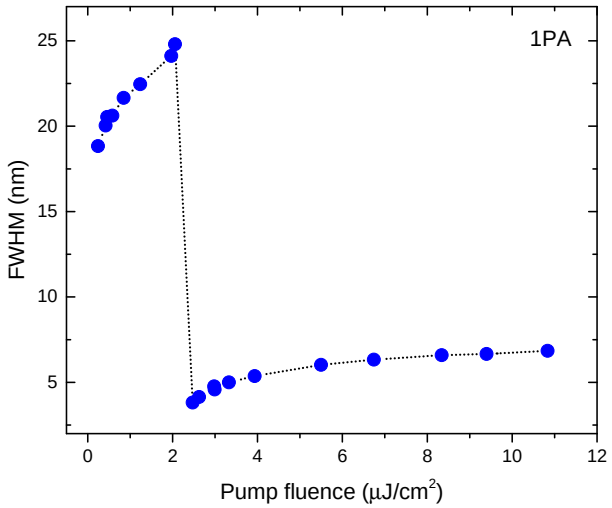

Figure 5.6: Fluence-dependent variation of the FWHM of the PL emission and ASE from $CsPbBr_3$ nanocubes drop-casted on a glass substrate. The excitation wavelength is 400 nm. This figure is adapted from [50].

The appearance of the ASE band is accompanied by the drastic reduction of the peak full width at half maximum (FWMH). As shown in Figure 5.6, the initial PL FWHM of 19 – 25 nm decreases to a few nanometers (3 – 7 nm) in the ASE peak. This narrow emission, which is redshifted compared to the PL peak by about 15 – 20 nm, corresponds energetically to the spectral position of optical gain in the material.

To calculate the pumping fluence at which stimulated emission starts to dominate over spontaneous emission, the integrated intensity of the photoemission is plotted versus the pump fluence (see Figure 5.7). In the graph on the left side, the data points are displayed in a linear plot. In such a way, a clear threshold behaviour can be observed, where the threshold pump fluence for ASE J_{th} marks the two distinct regimes:

- the region where $J_{laser} < J_{th}$, where the spontaneous emission dominates the overall emission process;
- the region where $J_{laser} > J_{th}$, where the light amplification takes place.

From the intersection of the linear fittings of the experimental data in these two regions, the threshold pump fluence is estimated to be around $2.14\,\mu Jcm^{-2}$.

The graph in Figure 5.7 (right side) shows the log-log plot of the experimental data. By using this different graphing technique, it is possible to identify three distinct regions corresponding to the relative photoemission regimes. Additionally, the slopes S of the three linear fittings associated to these three different regimes can be calculated.

Considering the variation of the PL intensity I_{PL} as a function of the pump fluence J, this can be expressed as:

$$I_{PL}(J) = J^S \cdot 10^{const.} = J^S \cdot const. \qquad \text{(linear plot)} \tag{5.1}$$

It follows that the slope calculated in a log-log plot through linear fitting gives informations about the I_{PL} dependency to J to the power of the slope (i.e. J^S):

$$\log_{10} I_{PL}(J) = S \cdot \log_{10} J + const. \qquad \text{(log - log plot)} \tag{5.2}$$

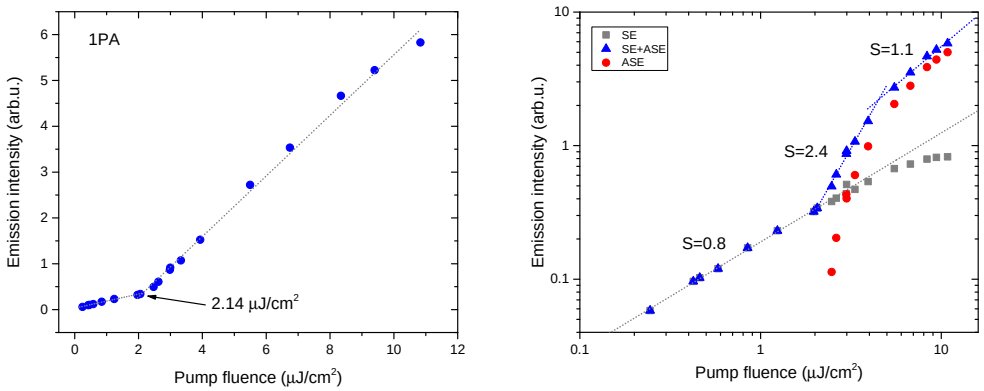

Figure 5.7: Linear plot (left side) and log-log plot (right side) of the integrated intensity of the PL emission and ASE as a function of the pump fluence. The excitation wavelength is 400 nm. This figure is taken from [50].

In the first region, which corresponds to low intensity photoexcitation ($J_{laser} < J_{th}$), the PL is expected to scale linearly with the increasing pump fluence. In this regime, the spontaneous emission is the process dominating the overall emission process. By fitting the data points with a power function, the slope associated to this process is $S = 0.8$. This slightly sublinear dependency can be associated to the presence of nonradiative decay channels that, when populated, decrease the total order of the global emissive process.

The second region ($J_{th} < J_{laser} < J_{sat}$) is characterised by an abrupt abandon of the linear dependency typical of the previous one. This change is marked by the system having reached the threshold fluence for ASE. At this pumping intensity, stimulated emission starts to dominate over spontaneous emission and optical amplification takes place in the excited material. The slope associated to this process is $S = 2.4$.

By tracking the spontaneous emission in the system (grey squares in Figure 5.7 right side), it is possible to observe that as the threshold fluence is reached, the spontaneous emission decreases in intensity. This is the feeding process of the ASE in the system, through which the additional pump intensity is fed into the ASE band.

The third region in Figure 5.7 (right side), corresponds to the saturation regime ($J_{laser} > J_{sat}$). Once the system reaches the threshold for saturation (J_{sat}), the amplification process decreases abruptly and the input power can not be further amplified. In this regime, a linear dependency of the intensity of the PL versus fluence is expected. Indeed, the slope associated to this process is $S = 1.1$.

5.3.1 Population inversion in $CsPbBr_3$ nanocubes

The optical pumping mechanism leading to population inversion in $CsPbBr_3$ nanocubes is simplified with the scheme in Figure 5.8. There, the individual nanocubes are represented by a multiple quantum well structure. Even though this model is an oversimplification of the real case, as (i) the nanocubes are in a weak quantum confinement regime [55] and neither (ii) excitonic levels, nor (iii) defect states are indicated here, it can be used to visualize the mechanism leading to population inversion.

The origin of ASE in LHP nanocrystals is currently debated in literature. Several models have been proposed involving either bi-excitonic lasing (which explains the redshifted ASE peak with respect to the PL peak) [70] or single-exciton gain [54] [87].

In the picture analysed here, the excitation laser creates e-h pairs at energies well above the electronic band edges. Relaxation of these charge carriers to the band edges can be followed by radiative recombination due to either:

- spontaneous emission of PL, or
- stimulated emission,

being the second option possible only if the nanocrystal is already found in a state of population inversion. Light amplification is then achieved when the light emitted

through stimulated emission overcomes the spontaneous emission and optical losses (such as reabsorption [40]) in the excited material.

In the case of isolated nanocrystals, population inversion can be achieved if the relaxation speed differs for electrons and holes. In such a way, the system can be found in the situation in which the number of electrons N_e occupying the lowest energy state in the conduction band exceeds the number of holes N_h in the highest energy state in the valence band. However, being the effective masses of electrons and holes in LHPs similar, it is possible to assume that this condition can not be easily achieved.

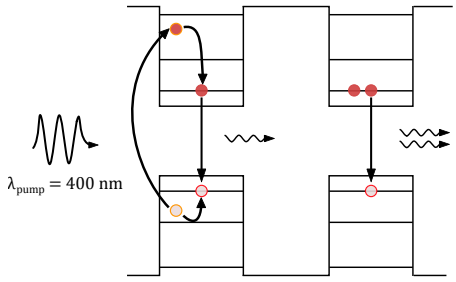

Figure 5.8: Schematic representation of optical pumping and population inversion in a multiple quantum well structure. The excitation wavelength is 400 nm.

However, on the basis of the extremely low pumping fluence for ASE that these nanocrystals show, a different picture represented to interpret the experimental observations needs to be developed. Towards the understanding of the underlying mechanism, the observation that ASE could be observed only on high density regions of $CsPbBr_3$ nanocubes plays a crucial role.

The close vicinity of the nanocubes can modify not only the way light is waveguided in the material, as it was previously observed in densely packed CsSe/CdS nanorods by Zavelani-Rossi et al. [88], but also the band structure of the nanocrystals. The effect of close-packing is studied in more detail in Chapter 6, where a combined system of uncoupled $CsPbBr_3$ nanocubes and closely-packed supercrystals is analysed.

5.4 Below-bandgap optical pumping

The remarkable nonlinear optical properties of the $CsPbBr_3$ nanocrystals, which have been discussed in Chapter 4, foretell the possibility to obtain efficient light emission from these nanocrystals even at excitation energies below the optical bandgap. To investigate whether it would be possible to obtain population inversion and light amplification also at below-bandgap optical pumping, the setup employed for ASE studies (see Section 3.1.5) is slightly modified by removing the BBO crystal to obtain femtosecond-pulsed laser excitation centered around 800 nm.

The nanocrystals used for these analysis are $CsPbBr_3$ nanocubes drop-casted on glass substrates. As previously observed in Section 4.1, this deposition technique leads to the formation of close-packed arrangements of the nanocrystals. The PL emission for different pump fluences of the $CsPbBr_3$ film is reported in Figure 5.9. At high laser fluences a new, narrow peak emerges and can be clearly distinguished from the broad PL peak observed for lower excitation fluences. This observation is similar to the findings observed for above-bandgap optical excitation. Hence, in $CsPbBr_3$ nanocubes ASE takes place even for below-bandgap optical excitation.

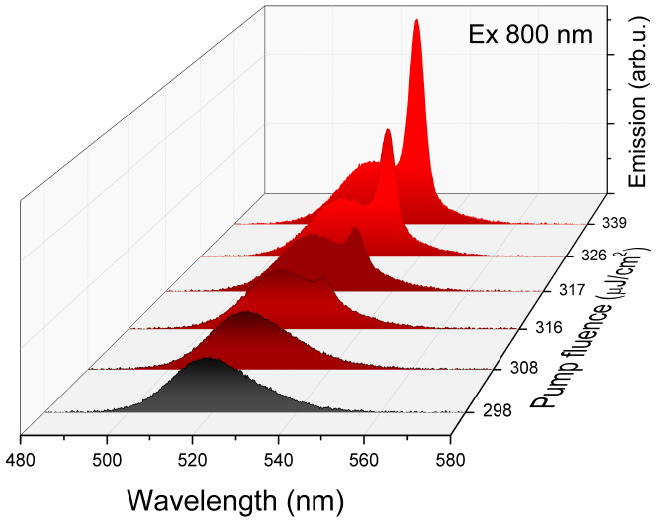

Figure 5.9: 3D plot of the pump fluence-dependent PL emission and ASE from $CsPbBr_3$ nanocubes drop-casted on a glass substrate. The excitation wavelength is 800 nm.

In Figure 5.10 the 2D plot of the fluence-dependent PL emission and ASE is displayed. This representation allows to analyse the aspects of the PL and ASE peaks in more details. Both the PL and the ASE peak remain centred around 517 nm and 530 nm, respectively. This agrees well with the findings obtained for above-bandap excitation and emphasises that the energetic levels responsible for spontaneous emission and population inversion are independent of the linearity of the absorption process. As observed in the case of linear excitation, the ASE peak redshifts from 530 nm to 532 nm when increasing the pump fluence, which can result from the bandgap renormalization.

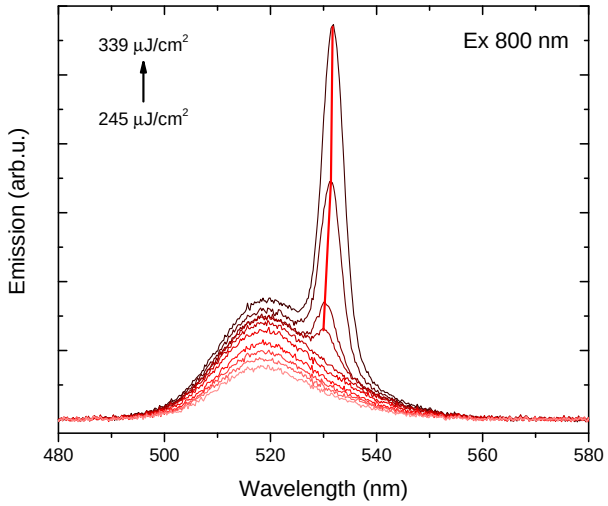

Figure 5.10: 2D plot of the pump fluence-dependent PL emission and ASE from $CsPbBr_3$ nanocubes drop-casted on a glass substrate. The excitation wavelength is 800 nm. The laser fluence is varied from 245 up to 339 μJcm^{-2}. The red line is a guide to the eye indicating the redshift of the ASE peak as the pumping fluence increases.

As expected, the ASE band is also characterised by a much narrower FWHM than the spontaneous emission peak (see Figure 5.11). Indeed, the initial FWHM of the spontaneous emission peak of around 22 nm decreases abruptly to only 5 nm as soon as ASE is observed in the system.

However, the threshold for ASE varies drastically changing from linear to nonlinear optical excitation. In Figure 5.12 the linear and the log-log plot of the PL intensity versus the pump fluence are displayed. From these graphs, the ASE threshold J_{th} is calculated to be equal to 312.6 μJcm^{-2} (for details about data analysis see Section 5.3). Even though

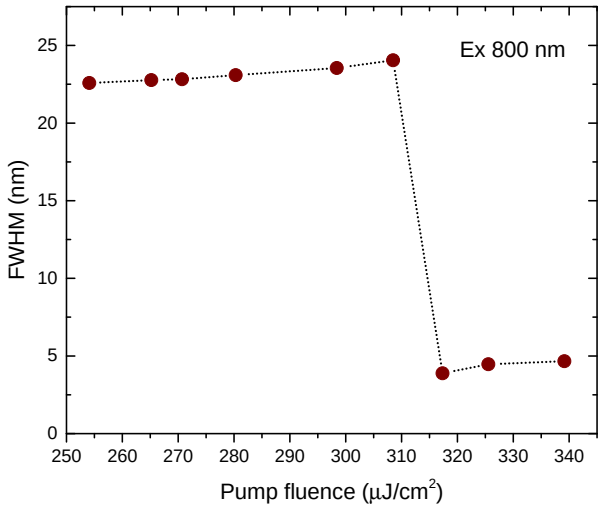

Figure 5.11: Fluence-dependent variation of the FWHM of the PL emission and ASE from $CsPbBr_3$ nanocubes drop-casted on a glass substrate. The excitation wavelength is 800 nm.

this value is two orders of magnitude higher than the threshold obtained in the case of linear optical excitation, it is still noteworthy that nonlinear optical excitation can lead to population inversion in these materials.

The log-log plot in Figure 5.12 (right side) further allows to analyse the distinct photoemission regimes that are separated by the threshold value J_{th}. Two different regimes can be clearly identified from this graph: the regime where spontaneous emission dominates ($J_{laser} < J_{th}$) and the one where stimulated emission dominates and light amplification takes place ($J_{laser} > J_{th}$). For both cases, the slope S associated with the dependency of the PL intensity I_{PL} to the excitation fluence J_{laser} is calculated.

Importantly, the slope associated to the first regime is equal to 3.1. In case of nonlinear absorption process, the value of this slope is closely linked to the order of the absorption process, as described in Section 2.2.2. Therefore, this dependency to the third power of the excitation fluence can be ascribed to a 3PA process, which can be consequently considered responsible for the optical pumping of the analysed system.

The observed deviation from a typical 2PA process, which would be expected for below-bandgap optical excitation at such energies, can be explained considering the model of MPA-MEG resonances developed in the previous chapter. This is described by

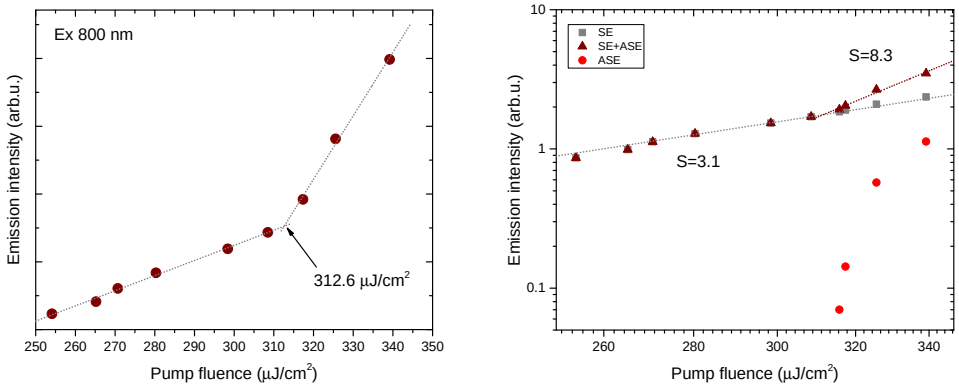

Figure 5.12: Linear plot (left side) and log-log plot (right side) of the integrated intensity of the PL emission and ASE as a function of the pump fluence. The excitation wavelength is 800 nm.

the relation:

$$phv = NE_x$$

where the number of photons simultaneously absorbed p is now equal to 3 and the exciton energy is E_x = 2.39 eV. In fact, being the energy of the single photons employed for photoexcitation hv = 1.54 eV, the following relation holds:

$$3hv = 1.9E_x \approx 2E_x \tag{5.3}$$

Therefore, the excitation wavelength of 800 nm is in close proximity to the MPA-MEG resonance where 3PA leads to the generation of two excitons.

The presence of MEG in this excitation regime could provide an explanation for the absence of saturation of the spontaneous emission observed for $J_{laser} > J_{th}$. In fact, contrary to what was observed in the case of above-bandgap excitation, here the intensity of the spontaneous emission is not decreasing abruptly with the rise of the ASE peak above threshold. This behaviour can be due to the fact that only a part of the photogenerated excitons participates in the feeding mechanism for population inversion. The remaining excitons are rather involved in the spontaneous emission, even after the threshold fluence for ASE has been reached.

5.4.1 Population inversion for below-bandgap excitation

Similarly to what already discussed for 1PA processes, the mechanism that $CsPbBr_3$ nanocubes undergo towards population inversion can be simplified with the scheme in Figure 5.13. However, contrary to what is observed for above-bandgap excitation, here the number of photons participating in the pumping system is ≥ 2. Therefore, the photoexcitation involves a certain number of virtual states, which are indicated by dotted lines in Figure 5.13.

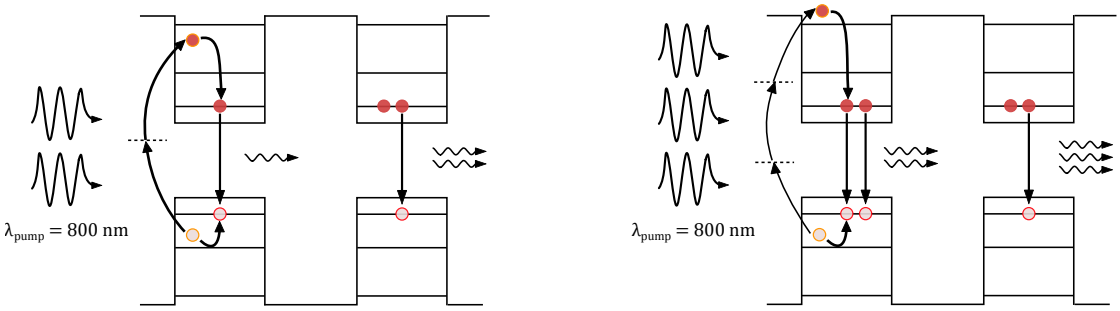

Figure 5.13: Schematic representation of optical pumping and population inversion in a multiple quantum well structure under below-bandgap excitation. 2PA is illustrated on the left side, whereas 3PA and subsequent multiple exciton generation is on the right side. The excitation wavelength is 800 nm.

The increase in the ASE threshold of around two orders of magnitude observed for excitation at 800 nm can be attributed to the lower efficiency of below-bandgap processes compared to above-bandgap ones. In fact, due to the lower absorption cross section for below-bandgap excitation, SE becomes less probable and therefore a higher pumping fluence is required to bring the system to the population inversion regime.

In the analysed system, it is possible to assert that the nature of the nonlinear absorption, which is responsible for the optical pumping, deviates from a typical 2PA process. Confirming the observation of the MPA-MEG resonances which is reported in Chapter 4, also here the vicinity to the resonant condition is accompanied by an increase of the order of the nonlinear absorption process. Hence, the detected increase in the rate of 3PA can be interpreted as a signature of the MPA-MEG resonance leading to the creation of 2 excitons for a 3-photon absorption process.

Under these conditions, it can be expected that the increasing number of photo-generated carriers favours the appearance of population inversion. However, this is true only if the Auger recombination rate does not increase as well.

As discussed in Section 4.5.2, Auger recombination can be effectively reduced when the nanocrystals are closely-packed to form a dense arrangement which enhances electronic coupling between them. Consequently, as ASE is only observable in high density regions for $CsPbBr_3$ nanocubes, the simple model for isolated crystals depicted in Figure 5.13 is not sufficient to explain the observed phenomena.

To better understand the mechanism leading to population inversion in these nanocrystals, electronically coupled $CsPbBr_3$ nanocubes are synthesised and analysed in Chapter 6.

6 Supercrystals: the effect of electronic coupling in $CsPbX_3$ nanocrystals

In the previous chapters it is described how an ordered assembly of the LHP nanocrystals is crucial for the successful outcome of the analysed experiments. In Chapter 4 the high degree of close-packing in the nanocrystal films enables the overlap of their electronic wavefunctions, which is fundamental to suppress Auger recombination and increase the radiative recombination rate of multiple excitons. On the other hand, in Chapter 5 light amplification is obtained from $CsPbBr_3$ nanocrystals only if high density regions, which can typically be identified by the *coffee-ring* configuration, are photoexcited. This high-density of nanocrystals not only ensures an effective waveguiding of the light to be amplified, but also allows the crystals to couple electronically.

The outcome of these experiments can be explained considering the process of self-assembly of the LHP nanocubes, which is based on the spontaneous drying that accompanies the solvent evaporation when the colloidal nanocrystals are deposited on a glass substrate. To push this process even further, in this chapter a novel synthesis method is reported through which ordered assemblies of nanocubes, the so-called *supercrystals*, can be formed colloidally before deposition. By using this synthesis technique, a higher degree of order in the nanocrystals assemblies is obtained and the optical properties of the resulting supercrystals are examined.

Finally, a system consisting of both uncoupled LHP nanocubes and their supercrystals is analysed under high intensity photoexcitation. The feeding mechanism for ASE is investigated and the emission from the supercrystals is revealed to be responsible for light amplification in the system, confirming the picture elaborated in the previous chapters.

6.1 Synthesis and structural characterization of $CsPbBr_3$ supercrystals

The synthesis of the $CsPbBr_3$ supercrystals is based on the ultrasonication technique described in Section 3.3.1. However, here the concentration of the precursor salts Cs_2CO_3 and $PbBr_2$ is increased by ten times with respect to what was described previously for the sysntesis of well-dispersed nanocubes. Instead, the concentration of solvent (octadecene) and ligands (oleic acid and oleylamine) is kept constant.

The change of these parameters in the synthesis of the nanocrystals is already visible to the eye, due to the variation in the density of the obtained dispersion (see Figure 6.1 a). Additionally, the high density of precursor salts result in the precipitation of part of the perovskite crystals, which is an indication of the presence of large particles in the dispersion.

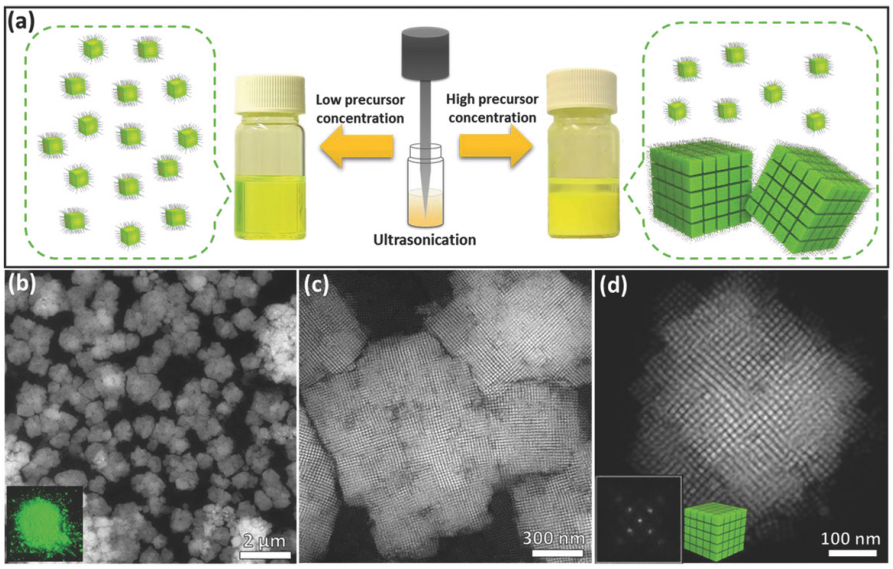

Figure 6.1: a Schematics of the synthesis techniques employed to produce isolated nanocubes (left side) or nanocubes coupled into supercrystals (right side). **b-d** HAADF-STEM images of $CsPbBr_3$ supercrystals with different magnifications. The inset of **b** is a photograph of the dried supercrystals under UV illumination, whereas the inset of **d** is the fast Fourier transform (FFT) pattern of the supercrystals, indicating the cubic close packing of the nanocubes. This figure is taken from [57].

These large particles are then extracted from the ensemble through centrifugation steps and are subsequently analysed by electron microscopy. The results are displayed in Figure 6.1 b-d. Even though particles with sizes around 1 µm are present, microscopy images at increased magnifications reveal that these particles are actually made of smaller cubic nanocrystals with sizes around 10 nm. These nanocubes are nicely arranged one next to the other until forming the superlattice assemblies observed in Figure 6.1 b.

By shining UV light on a dried supercrystal sample (see inset in Figure 6.1 b), a strong green emission can be clearly observed. The emission properties of these superstructures are analysed and characterised in the next section.

6.2 Optical characterization of $CsPbBr_3$ supercrystals

The strong PL signal, which can be detected from a dried supercrystal sample, is an indication that, even though the sample consists of large agglomerates of the individual nanocubes, their emission properties do not resemble the ones of bulk-like perovskites (which are, instead, characterised by a significantly lower PLQY [48]).

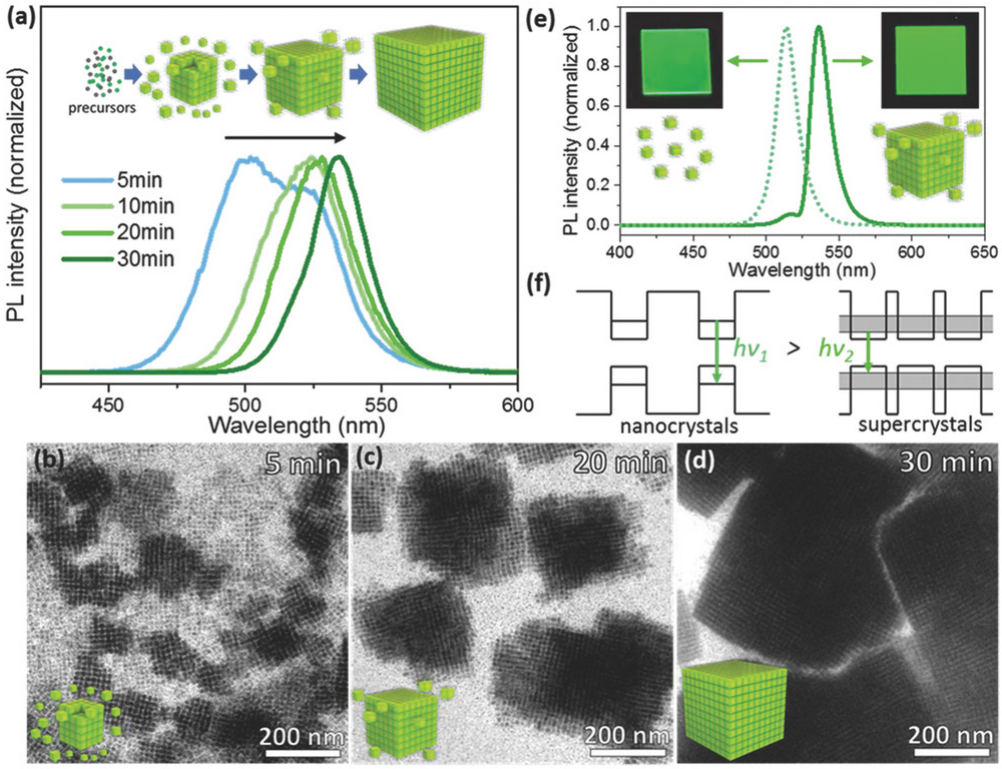

Figure 6.2: **a** PL spectra acquired at different reaction times (5, 10, 20 and 30 minutes, respectively) during the synthesis of $CsPbBr_3$ supercrystals. The scheme on top of this graph represents the proposed formation mechanism. **b-d** Bright-field TEM images of the results of the synthesis after a reaction time of 5, 20 and 30 minutes, respectively. **e** PL spectra obtained from a spin-coated film of isolated nanocubes (left side) and supercrystals (right side). In the insets the photographs of the corresponding films are shown. **f** Energy diagram proposed to describe the redshifted PL in the supercrystals with respect to the case of isolated nanocubes. The origin of minibands is the basis for this method. This figure is taken from [57].

To study the properties of the synthesised supercrystals, and to analyse the variation of the optical properties of the individual nanocubes which are involved in their forma-

tion process, PL spectra are recorded during the nanocube assembly (see Figure 6.2 a). In combination with these measurements, TEM images of the samples are acquired at different reaction times, in order to correlate the optical characterization with the structural advancement of the supercrystals formation (see Figure 6.2 b-d).

The first PL signal can be detected after 5 minutes from the beginning of the synthesis reaction (light blue curve in Figure 6.2 a). This broad PL spectrum indicates the presence of different populations in the ensemble. Two shoulders can be clearly identified, the first one located around 499 nm and the second one around 526 nm. These PL shoulders can come from individual small $CsPbBr_3$ nanocubes (which quantum-confinement is higher than in the case of the nanocubes employed in Chapters 4 and 5) and from already aligned nanocubes, respectively. This association is confirmed by TEM images of the sample at the same reaction stage (see Figure 6.2 b).

The second analysis is done for the reaction time 10 minutes. At this stage, the intensity of the first shoulder is strongly decreased, indicating that the second shoulder constitutes now the main component of the reaction. Additionally, the position of the first shoulder shifts to longer wavelengths and is centred around 512 nm now, indicating that the seed-mediated growth of the individual nanocubes continues.

This trend is maintained for the reaction times of 20 and 30 minutes, where ultimately the two peaks overlap and therefore no shoulders can be clearly distinguished any more. The final peak obtained after 30 minutes from the beginning of the synthesis is centred around 535 nm, which is fairly surprising for $CsPbBr_3$ nanocrystals as the maximum redshift observed for these nanostructures (in the case of non-quantum confined nanocrystals) results in PL centred around 520 nm [89]. On the contrary, the energetic position of this PL signal resembles the one observed for bulk millimeter-sized $CsPbBr_3$ crystals [90].

6.2.1 Miniband formation in $CsPbBr_3$ supercrystals

To compare the results of the supercrystal synthesis with the ones obtained synthesising isolated nanocubes, these two different samples are deposited through spin-coating onto two glass substrates. The photographs of these substrates under UV light illumination are displayed in Figure 6.2 e.

The sample on the left side consists of $CsPbBr_3$ nanocubes, synthesised using the method indicated in Section 3.3.1. These are produced using a low concentration of

precursors salts, which results in the formation of isolated nanocrystals in dispersion. Once these nanocrystals are deposited on a glass substrate, the evaporation of the solvent surrounding them may result in a form of ordering of the nanocrystals, as observed in Section 4.5.2. However, long-range crystal packing leading to the formation of microstructures, such as the ones observed in the case of supercrystals, is not observed in that case. The PL peak obtained from this sample is centred around 514 nm (left graph in Figure 6.2 e).

On the other side, the sample obtained from $CsPbBr_3$ supercrystals (right graph in Figure 6.2 e) exhibits a main PL peak centred around 535 nm, together with a small shoulder at 516 nm, which can be an indication of a small amount of isolated nanocubes present in the ensemble.

The PL redshift of 21 nm (~ 100 meV) observed from isolated nanocubes to supercrystals can be explained considering the electronic coupling between the nanocrystals which is present in the latter case. This coupling results from the close vicinity of the nanocubes, which causes the electronic wavefunctions of the individual nanocubes to interact. This is similar to what happens with atoms in a solid, where electronic interactions give rise to the material band structure. In coupled nanocrystals this interaction leads to the formation of so-called *minibands*, both in the valence and in the conduction band (see Figure 6.2 f).

In the system analysed here, the two different materials of which the superlattices consist are (i) the $CsPbBr_3$ nanocubes and (ii) the ligand shells surrounding them. From the TEM images the size of the nanocubes can be identified to be around 10 nm, while the thickness of the ligand layer is $\leq$ 1 nm. Therefore, since the Bohr diameter for $CsPbBr_3$ nanocrystals is reported to be around 7 nm [91], a weak quantum confinement regime is to be considered.

In the case of $CsPbBr_3$ supercrystals, the minibands are expected to have similar widths in the valence and conduction band, as schematically shown in Figure 6.2 f. This is due to the fact that the effective masses of electrons and holes have similar values in LHPs.

6.2.2 Redshift and reabsorption

To exclude that the observed redshift in the PL peaks is mainly related to reabsorbption effects (which were studied by Pazos-Outón et al. in films of bulk LHPs [81]), the PL

spectra of films made of isolated $CsPbBr_3$ nanocubes and supercrystals are analysed together with their corresponding PLE spectra (see Figure 6.3).

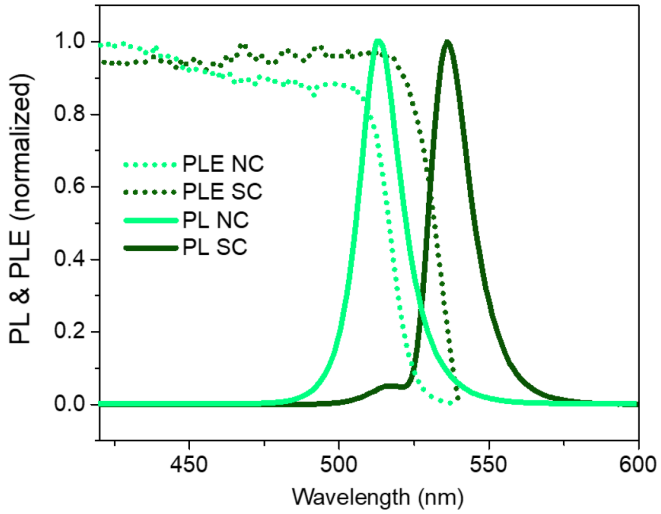

Figure 6.3: PLE spectra (dotted lines) and PL spectra (solid lines) from a spin-coated film of isolated nanocubes (light green) and supercrystals (dark green). This figure is taken from [57].

Reabsorption, also called "photon recycling" by the solar cell community, is a process by which a material emits a certain amount of light of which the energy is then reabsorbed by another portion of the material. In this sense, the reabsorbed photons are recycled (i.e. used to create new electron/hole pairs) by the absorbing material instead of being lost in free-space emission.

The effect of reabsorption on the optical properties of a semiconductor is reflected in the appearance of a strongly asymmetric PL peak (where the short-wavelength side is missing in the PL spectrum) with a greatly reduced FWHM [40]. At the same time, the absorption (or PLE) spectrum is not affected by it.

In contrast to that, in the $CsPbBr_3$ supercrystals analysed here, the PL redhift due to the increased electronic coupling from the isolated nanocubes to the ordered superlattices is not accompanied by a narrowing or an important asymmetry of the resulting PL peak. In addition to that, the PLE spectra reveal a strong redshift of the onset between the two samples analysed, which is a strong indication that the electronic band structure of the ordered nanocubes is changed with respect to their isolated counterparts.

6.2.3 The effect of dilution on $CsPbBr_3$ supercrystals

As supercrystals are obtained here by increasing the density of precursor salts in the synthesis procedure, the reversibility of the supercrystal formation can be tested by analysing the effect that dilution has on the ordered nanocube structures.

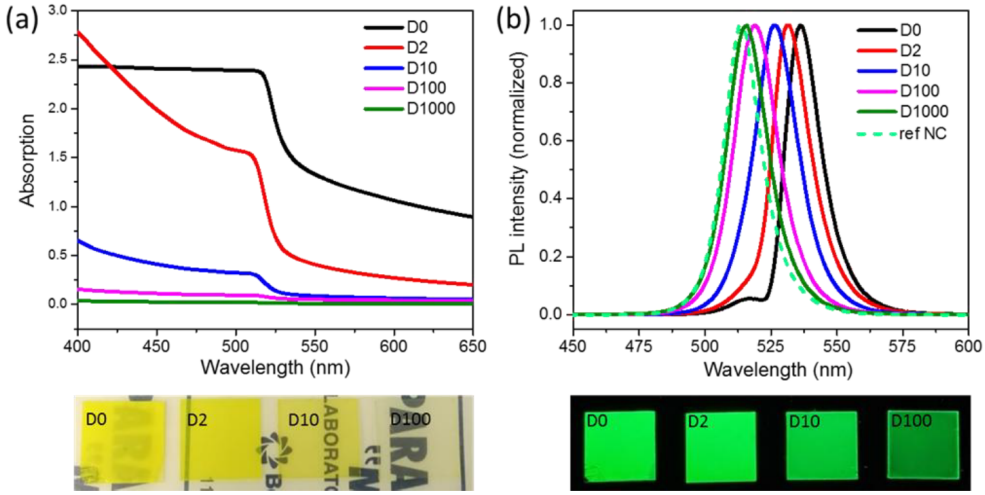

Figure 6.4: a Absorption spectra of spin-coated films of supercrystals with different dilutions. D0 stands for no dilution, while D*X* stands for a dilution 1:*X*, where *X* is varied from 2 to 1000. **b** PL spectra of the corresponding films. The photographs of the films under room light (left side) and UV light (right side) are displayed in the lower section. This figure is taken from [57].

In Figure 6.4 the absorption and PL spectra of films obtained by spin-coating supercrystal dispersions with varying dilutions *D* are displayed. The black curves indicate the measurements taken on an undiluted sample, while the other colors are for different dilutions from 1:2 to 1:1000. Additionally, the PL spectrum obtained from a film made of isolated nanocubes is shown in Figure 6.4 b.

It can be observed that by diluting the initial supercrystal dispersion, both the absorption onset and the PL peak center wavelength gradually blueshift to higher energies. This is an indication of the disassembly process of the supercrystals, which occurs in conjunction with an increase of the dilution coefficient.

Furthermore, the PL signal obtained for a dilution of 1:1000 (see Figure 6.4 b) overlaps almost perfectly with the PL peak from isolated nanocubes. Therefore, this dilution results in the nearly complete disassembly of the supercrystals in the suspension.

Therefore, it is evident from these measurements that the formation process of ordered nanocubes is reversible and can be inverted by increasing the relative amount of solvent in the supercrystal dispersion.

6.2.4 Filling the "green gap"

The term "green gap" is understood as the lack of high quantum yield emitters with an emission wavelength at 532 nm. This color requirement is crucial in applications as television displays, which quality is regulated by the "Rec. 2020" standard[1]. This identifies a color space delimited by the RGB primary colors characterised by the following wavelengths: 630 nm for the red, 532 nm for the green and 467 nm for the blue. These three points are represented as the vertices of a triangle in a CIE 1931 chromaticity diagram[2] (see Figure 6.5 c) and indicate the limits of the color range that can be achieved by a display by properly mixing the RGB primary colors.

To demonstrate the applicability of $CsPbBr_3$ supercrystals for light emitting applications, a LED device is fabricated (see Figure 6.5 a). The electroluminescence obtained from it nicely resemble the PL peak obtained in these studies (see Figure 6.5 b).

With a view to using LHPs in light emitting applications satisfying Rec. 2020, the analysed $CsPbBr_3$ supercrystals are ahead of the other perovskites counterparts analysed so far. This is mainly due to the fact that not only their PL emission approaches the desired 532 nm (more than LHPs thin films or uncoupled nanocubes), but also their PLQY is relatively high (around 45%). As a comparison, the emission properties of $CsPbBr_3$ thin films comprising of larger nanocubes (side length around 100 nm) are much worse, with PLQY $\leq$ 0.5% (see Figure 6.6). In contrast, the PLQY of a film made of uncoupled $CsPbBr_3$ nanocubes lies around 40%.

[1] Rec. 2020 stands for "ITU-R Reccomendation BT.2020", which is a protocol defining the quality standards for ultra-high-definition television (UHDTV).

[2] The CIE 1931 chromaticity diagram was created in 1931 by the International Commission on Illumination (CIE) to define the connection between the different wavelengths in an electromagnetic visible spectrum and the way color vision is perceived by humans. It therefore delineates a color region, the so-called color space, which includes all the colors that are visible to humans with an average eyesight.

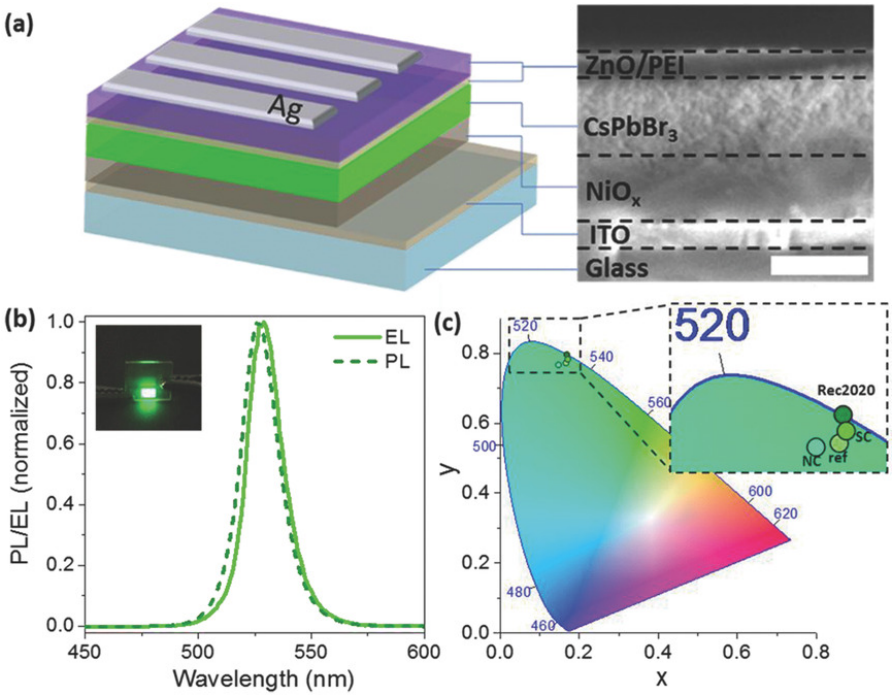

Figure 6.5: **a** Schematics of the architecture (left side) and SEM cross-section of the LED device based on $CsPbBr_3$ supercrystals. **b** Electroluminescence (EL) and PL obtained from the LED device. The inset shows a photograph of it. **c** CIE 1931 chromaticity diagram of the color coordinates obtained from the LED. This figure is taken from [57].

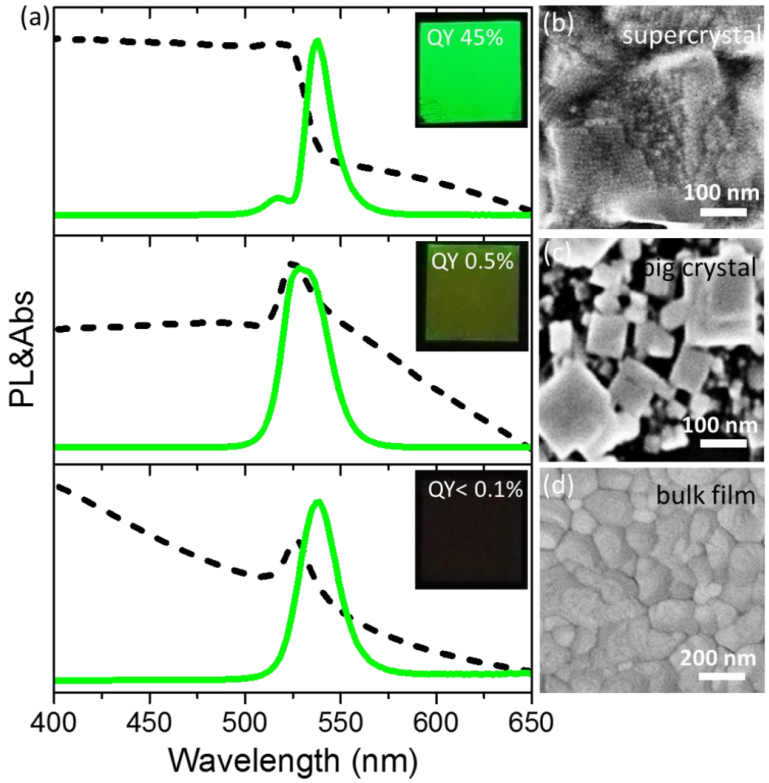

Figure 6.6: a Absorbance and PL spectra of $CsPbBr_3$ supercrystals, big crystals and bulk film, respectively. The insets show a photograph of the films under UV light excitation, together with their PLQY. **b-d** SEM images of the corresponding films. This figure is taken from [57].

6.3 High intensity photoexcitation in $CsPbBr_3$ supercrystals and nanocubes

To understand the role of close-packing of the LHP nanocrystals for light amplification, a system comprising both uncoupled $CsPbBr_3$ nanocubes and supercrystals is synthesised. The synthesis procedure slightly differs from the one used so far based on ultrahigh-frequency tip-sonication. In fact, to synthesise these combined structures a different approach is used, consisting in the hot-injection synthesis of highly monodisperse $CsPbBr_3$ nanocubes (see Section 3.3.2 for more details) and in the subsequent controlled evaporation of the solvent where these are dispersed. In such a way, the film of nanocrystals obtained consists of regions where the nanocubes are nicely arranged in superlattices and regions where the nanocrystals remain uncoupled, similarly to what Rainò et al. obtained [77].

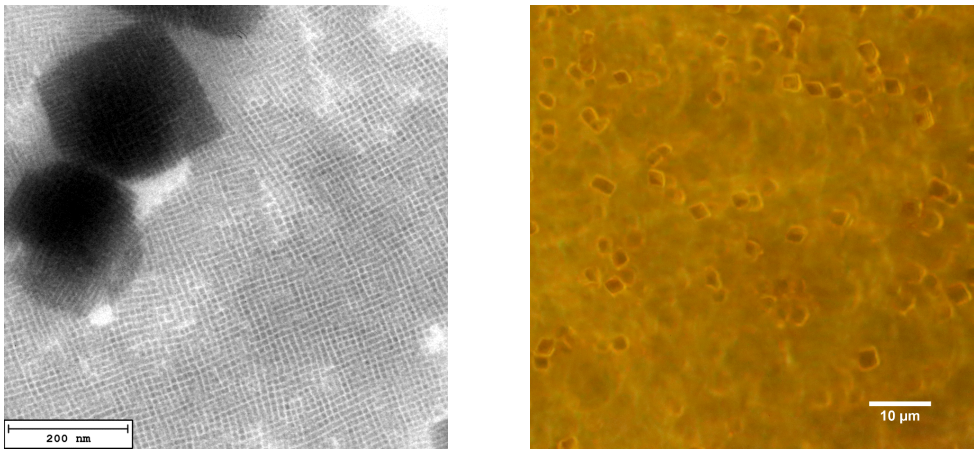

Figure 6.7: On the left side, a bright-field TEM image of the $CsPbBr_3$ supercrystals and nanocubes. The supercrystals can be identified by the stronger contrast, whereas the nanocubes appear lighter in the grey-scale, due to the smaller thickness that results in an higher transmission of the electron beam. The scale bar is 200 nm. On the right side, a DFM image of a film comprising both $CsPbBr_3$ supercrystals and nanocubes. Here the solvent evaporation is retarded with respect to what is obtained by depositing the dispersion on a TEM grid. In such a way, the size of the supercrystals is increased up to several micrometers. The scale bar is 10 µm.

In Figure 6.7 (on the left side) a TEM image of such system is reported. It is possible to observe that the individual nanocubes are here smaller in size (~ 10 nm) with respect to the ones obtained previously with the ultrahigh-frequency tip-sonication method. The nanocubes constituting the building blocks of the superlattices are also identifiable from this image, along with their inter-particle spacing which appears smaller than the one of the crystals not assembled in the supercrystal fashion.

In contrast to what obtained with the ultrahigh-frequency tip-sonication technique, here the supercrystals constitute only a small portion of the final sample. The nanocubes which are assembled in the superlattices form structures ranging several micrometers, as shown on the right image in Figure 6.7. Therefore, by studying these structure it is possible to understand the effect of electronic coupling on the light amplification properties of spontaneously assembled or so-synthesised superlattices.

6.3.1 ASE with $CsPbBr_3$ supercrystals and nanocubes

The setup employed for the high intensity photoexcitation experiment is described in Section 3.1.5. The configuration of frontal excitation and detection is used to test the light amplification and waveguiding properties of the studied material in the direction perpendicular to the glass substrate where it is deposited.

Under these conditions, the laser beam has a diameter of roughly $1.55\,mm^2$, which illuminates several individual supercrystals, as well as many individual nanocubes which are deposited next to them. It is therefore beneficial to interpret the obtained results considering the sample to be constituted by assembled supercrystals, as well as uncoupled nanocubes.

While the excitation wavelength is set to 400 nm, the laser fluence is gradually varied from $2.8\,\mu Jcm^{-2}$ up to $225.5\,\mu Jcm^{-2}$ and the light emission from the specimen is recorded (see Figure 6.8).

From the emission spectrum obtained for low-intensity photoexcitation, it can be observed that the sample exhibits a PL signal centred around 520 nm. This is in line with what has previously been reported for $CsPbBr_3$ nanocubes of such size [92].

When the photoexcitation fluence is increased further, an additional narrower peak starts to appear around 530 nm. This is an indication that at a certain excitation threshold, ASE dominates the light emission.

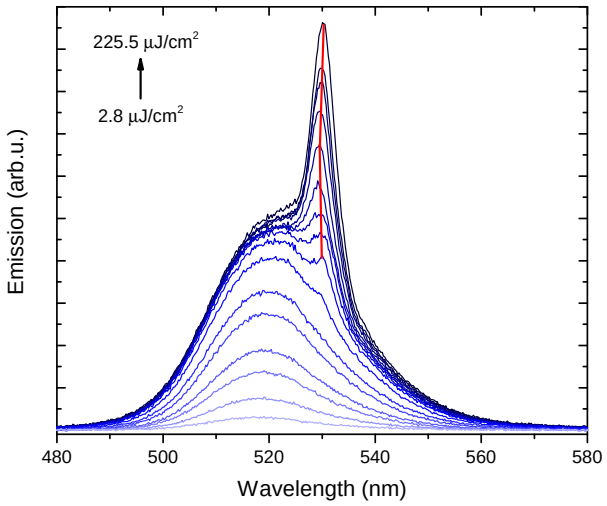

Figure 6.8: Pump fluence-dependent PL emission and ASE from $CsPbBr_3$ supercrystals drop-casted on a glass substrate. The excitation wavelength is 400 nm, while the fluence is varied from 2.8 up to 225.5 μJcm^{-2}. The red line is a guide to the eye indicating the position of the ASE peak.

To estimate the exact threshold at which stimulated emission overcomes spontaneous emission, the integrated intensity of the light emission is reported in Figure 6.9 versus the pump fluence. In the graph on the left side, the linear dependency of the emission intensity over the laser fluence is shown.

It is possible to observe that, contrary to what is obtained for $CsPbBr_3$ nanocubes in Section 5.3, here the ASE onset is not obvious and the graph strongly differs from the typical "S-type" scheme described there. Instead, a deviation from the initial linear trend is observed already for fluences > 16.2 μJcm^{-2}, leading to an overall saturation of the light emission. Although no ASE peak is visible at such fluences, it is possible to assign the origin of the lossy PL emission to the begin of light amplification in the system. The feeding mechanism, however, is able to overcome the overall optical losses only at higher fluences around 117.9 μJcm^{-2}.

In the log-log plot shown in Figure 6.9 (right side) this trend is displayed in a clearer way. The data points are fitted with linear functions to extrapolate the order of the different processes involved in the light emission. For low pump fluences, the linear fit

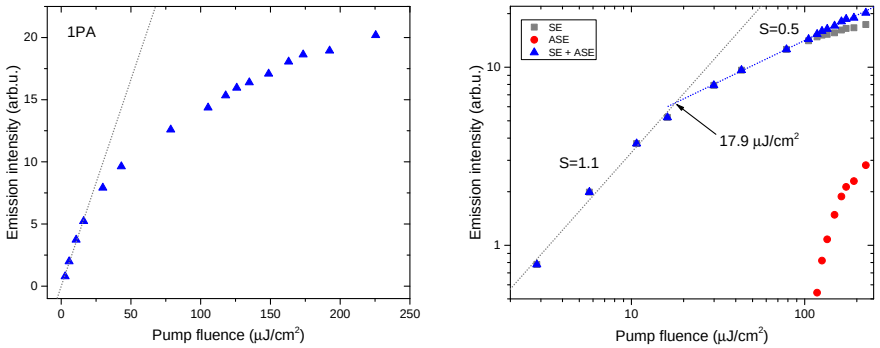

Figure 6.9: Linear plot (left side) and log-log plot (right side) of the integrated intensity of PL emission and ASE from $CsPbBr_3$ supercrystals. The excitation wavelength is 400 nm.

highlights the slope value $S = 1.1$, which is an indication of the linear photon absorption and light emission.

Instead, the overall slope obtained for higher fluences is strongly sublinear ($S = 0.5$). Being the SE higher than the ASE in intensity, the rise of the amplification is not straight forward from the integrated emission intensity. However, by looking exclusively at the integrated ASE intensity (red dots in the graph), the threshold for the ASE detection can be ascribed to pump fluences $\geq 117.9\,\mu Jcm^{-2}$.

At these high pump fluences a further saturation of the SE signal with respect to the total emission intensity is observed (see gray squares on the right side of Figure 6.9). This saturation is an indication that part of the SE is suppressed in favour of the increase in stimulated emission, hence ASE.

In order to identify the feeding process leading to ASE emission in the analysed system, the emission spectra are closely studied and modelled by Gaussian functions (see Figure 6.10). For this purpose, the SE and ASE emission spectra are plotted on an energy scale and fitted with Gaussian functions.

As the best fit of the PL spectra with a single Gaussian function could not be obtained, two distinct Gaussians are used instead. The convolution of these two functions perfectly represents the experimental data. The peak on the high-energy side is centred around 518 nm and is higher in intensity and narrower than the low-energy side peak, which is located around 525 nm (see the graph on the left side in Figure 6.10). This observation hint towards the assignment of the PL to two different populations in the

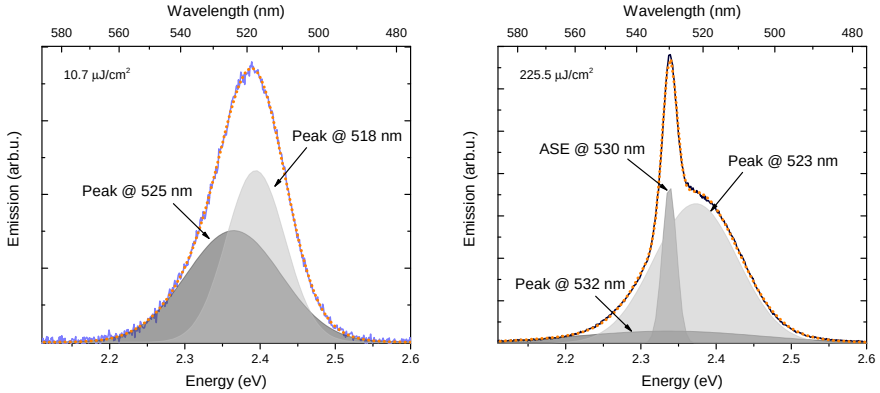

Figure 6.10: Analysis of the SE and ASE peak from $CsPbBr_3$ supercrystals. The excitation wavelength is 400 nm, whereas the fluence is 10.7 μJcm^{-2} (left side) and 225.5 μJcm^{-2} (right side). The filled curves represent Gaussian fit, the orange dotted line is their cumulative fit peak.

sample: the first one constituted by $CsPbBr_3$ supercrystals and the second one by the uncoupled (or less coupled) nanocubes counterparts.

When the pump fluence is increased above the ASE threshold, the positions of these two peaks slightly redshift and the narrow ASE peak at 530 nm is added. Interestingly, while the high-energy side peak increases in intensity, the intensity of the low-energy side changes dramatically until almost vanishing at 225.5 μJcm^{-2}.

The evolution of the two SE peaks is therefore analysed independently and plotted in Figure 6.11. The integrated intensity relative to the high-energy peak is represented by the light grey squares, while the low-energy peak is displayed with dark grey squares and the ASE peak with red circles. Interestingly, it is possible to observe that while the high-energy peak has an almost linear dependency with the pump fluence, the low-energy one saturates as soon as the ASE threshold (vertical red line in the graph) is reached.

By identifying the high-energy peak with the uncoupled nanocubes and the low-energy one with the supercrystals, it is therefore possible to interpret this observation as follows. While the SE from the uncoupled nanocubes is not affected by the appearance of ASE and undergoes only a weak saturation as the pump fluence is increased, the opposite trend can be asserted for the supercrystals. In fact, as soon as the ASE threshold is reached, the SE from the supercrystals undergoes a strong saturation process, leading ultimately to a strong suppression of the signal attributed to it.

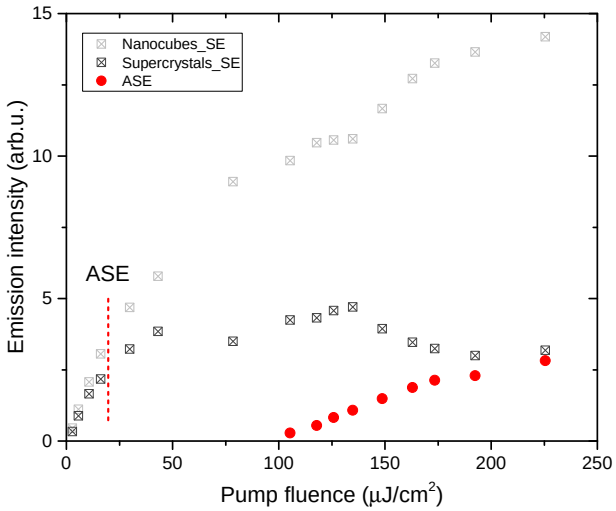

Figure 6.11: Analysis of the variation of the emission intensity relative to the two different SE and ASE peaks. The ASE threshold is indicated with the vertical red dotted line.

This observation hints towards the assignment of the SE from the supercrystals to the feeding mechanism responsible for the achievement of population inversion in the analysed system. This discovery is in accordance with the results obtained in Chapter 5 and support the hypothesis that a closely-packed arrangement of the nanocubes is fundamental to obtain efficient ASE in $CsPbBr_3$ perovskites.

6.3.2 Population inversion in coupled *vs* isolated $CsPbBr_3$ nanocubes

From the results of the ASE experiments in a combined system of $CsPbBr_3$ supercrystals and nanocubes it is possible to evince that the presence of the first ones is fundamental to achieve ASE. But what is the reason why the uncoupled nanocubes do not bring the system in the population inversion regime?

The answer to this question is, in my view, twofold. First of all, the sample geometry of the supercrystals favours light amplification. Being the light emission from the sample detected in the backward direction of the laser excitation, a higher number of nanocrystals deposited vertically on the glass substrate means higher chances of waveguiding the spontaneously emitted and amplified light in the direction of detection.

In contrast to the thick supercrystal structures, which are several micrometers in size, the isolated nanocubes surrounding them are expected to be just a few monolayers-thick.

However, thicker films of uncoupled $CsPbBr_3$ nanocubes, like the ones analysed in Chapter 5, do not support ASE either unless the nanocubes are spontaneously packed in a coffee-ring structure. Therefore, the thickness of the emitter layer does not explain the observed results on its own.

Another parameter to be taken into account is the effect of electronic coupling. In Figure 6.12 a schematic representation of optical pumping in a uncoupled quantum well structure (left side) and in a supercrystal structure (right side) is reported.

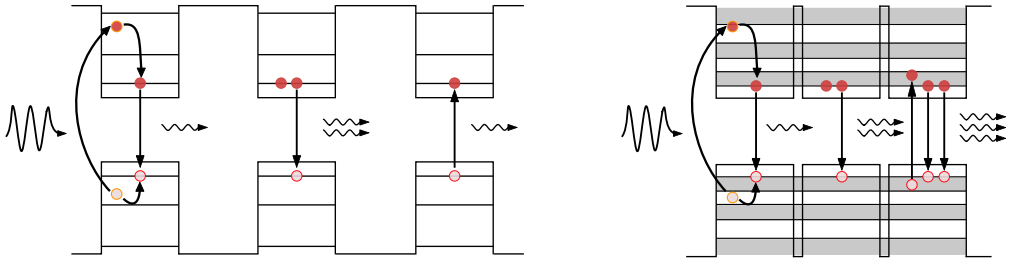

Figure 6.12: Schematic representation of optical pumping and population inversion in a multiple quantum well structure (left side) and a supercrystal (right side). The excitation wavelength is 400 nm.

It appears evident from this representation that obtaining population inversion is harder in the case of isolated nanocrystals. In fact, being the energy levels separated between two adjacent crystals, even if a certain number of nanocrystals show population inversion, this is not necessarily true for the nanocrystals surrounding them. Hence, the probability for a photon to be absorbed is higher than the probability to get amplified.

Additionally, in the case of isolated nanocrystals the narrow energetic linewidth of the states where population inversion could potentially take place contributes to increase the amount of Auger recombination, which is another process fighting against population inversion.

Conversely, in the case of electronic coupling between the nanocrystals, population inversion becomes more likely. The presence of minibands extending through the neighbouring nanocubes favours the spatial delocalization of the photogenerated carriers into different nanocubes, which lowers down Auger recombination (as shown in Section 4.5.2). This delocalization also implies that, while in the case of isolated

nanocrystals more than half of them have to be in the population inversion condition in order to have net amplification, in the case of supercrystals a lower number of inverted crystals is enough to obtain light amplification.

Additionally, the higher energetic width of the minibands results in a broader gain spectrum for these materials, which also leads to an easier achievement of population inversion. This is related to the fact that absorption does not have to be fully saturated in supercrystals in order to achieve population inversion, as the states for absorption and stimulated emission are spread energetically. These can therefore happen simultaneously, reducing the competition for the achievement of population inversion.

Therefore, in view of what is listed above, it can be concluded that the packing of the $CsPbBr_3$ nanocubes into ordered superlattices enables the observation of light amplification in the analysed system.

7 Summary and conclusions

In summary, in this thesis possible pathways to go beyond the Shockley-Queisser limit by using lead halide perovskite nanocrystals as a test system have been analysed. Within this framework, the nonlinear optical absorption (MPA) of these nanostructures and the possibility to obtain multiple exciton generation (MEG) for below-bandgap photo-excitation have been studied. Not only it was reported here for the first time that MPA and MEG can be combined together in perovskite nanocrystals, but also that high-order absorption processes, deviating from the expected two-photon absorption, can be observed at very specific energetic positions corresponding to MPA-MEG resonances.

This result thus validates the central idea that the appearance of the two processes in the same system is possible and must be sought. Additionally, this observation has turned out to be extremely significant as these specific energies could be linked to multiples of the semiconductor band-gap energy. In such a way, a new method was developed by means of which this effect could be described as a resonance behaviour between MPA and MEG, which has never been reported before.

Interestingly, the resonance effect between MPA and MEG could only be observed once the perovskites were assembled in an orderly fashion, forming supercrystals. This phenomenon can be attributed to the electronic coupling given by the close-packed arrangement of individual nanocrystals that reduces the incidence of Auger recombination, which represents the main opponent of the survival of multiple excitons. The chemical composition of the perovskites can be varied to tune the energetic position of the MPA-MEG resonances, provided that the supercrystal geometry is kept. This has been successfully demonstrated for $CsPbBr_3$ and $CsPbI_3$ nanocrystals, confirming that the same effect can be obtained for different halides (X) in $CsPbX_3$ perovskites. Even though the presence of these resonance was up to now only confirmed in literature

for perovskite nanocrystals [93], the general nature of the observed phenomenon suggests a wider applicability of the MPA-MEG resonances to other semiconductor arrays. However, further studies shall be carried out in order to fully confirm this statement.

Furthermore, thinking about optoelectronic applications of these efficient light emitters, the possibility to use them for light amplification and lasing has been investigated. To this end, both electronically coupled and uncoupled perovskites structures were analysed under high-intensity optical pumping conditions. $CsPbBr_3$ nanocubes were found to exhibit an extremely low threshold for amplified spontaneous emission (ASE) under above-bandgap excitation ($2.14 \mu J cm^{-2}$) when spontaneously packed into "coffee-ring" configurations. These measurements indicate that the arrangement of the nanocrystals and their relative proximity is an important parameter, influencing not only their nonlinear properties but also their ability to amplify light. Below-bandgap optical pumping in the proximity of a MPA-MEG resonance was also investigated. The results showed that ASE can be obtained under these conditions as well, and a model to explain the population inversion mechanism was developed.

To deepen the understanding of the function of close-packing on the light emission and amplification properties of $CsPbBr_3$ nanocubes, samples comprising both nanocubes and their relative supercrystals were investigated. The supercrystals exhibited a red-shift in their PL and absorbance spectra which could be attributed to the formation of minibands. Additionally, under high-intensity photoexcitation, ASE could be observed from these ordered assemblies. Interestingly, the emission from the excited material could be deconvoluted into two different emission peaks: one due to the presence of uncoupled nanocubes and one due to coupled ones. By doing power-dependent studies it could be observed that the spontaneous emission from the supercrystals saturated almost completely when the threshold fluence for ASE was reached. This is an indication that the feeding mechanism providing the origin of light amplification can be attributed to the electronically coupled nanocrystals.

With these observations, it was proven that the arrangement of perovskite nanocrystals plays a crucial role not only in determining the appearance of MPA-MEG resonances, but also in controlling their ASE efficiency. Importantly, it was demonstrated for the first time that, employing a closely-packed arrangement of these nanocrystals, it is possible to use low-energy photons to efficiently generate multiple excitons close to the observed resonances.

Additionally, feasibility studies to check the applicability of these findings for solar applications have been carried out. As a result, it was shown that the proposed MPA-MEG resonances, which have been studied using pulsed lasers as excitation source, can also be obtained with continuous wave solar energy through the use of solar concentrators. This mechanism is therefore feasible for enhancing the conversion efficiency of low-energy photons stemming for the infrared regime of the solar spectrum. This process can be very efficient, especially when the energy exchange is close to the reported resonances.

Bibliography

[1] International Energy Agency (IEA). *https://www.iea.org/*.

[2] William Shockley and Hans J. Queisser. "Detailed balance limit of efficiency of p-n junction solar cells". In: *J. Appl. Phys.* 32.3 (1961), pp. 510–519.

[3] R J Ellingson et al. "Highly efficient multiple excition generation in colloidal PbSe and PbS quantum dots". In: *Nano Lett.* 5 (2005), pp. 865–871.

[4] Richard D. Schaller, Vladimir M. Agranovich, and Victor I. Klimov. "High-efficiency carrier multiplication through direct photogeneration of multi-excitons via virtual single-exciton states". In: *Nat. Phys.* 1.3 (2005), pp. 189–194.

[5] James E. Murphy et al. "PbTe colloidal nanocrystals: synthesis, characterization, and multiple exciton generation". In: *J. Am. Chem. Soc.* 128.10 (2006), pp. 3241–3247.

[6] Matthew C. Beard et al. "Multiple exciton generation in colloidal silicon nanocrystals". In: *Nano Lett.* (2007).

[7] Joseph M. Luther et al. "Multiple exciton generation in films of electronically coupled PbSe quantum dots". In: *Nano Lett.* 7.6 (2007), pp. 1779–1784.

[8] Ji Minbiao et al. "Efficient multiple exciton generation observed in colloidal PbSe quantum dots with temporally and spectrally resolved intraband excitation". In: *Nano Lett.* 9.3 (2009), pp. 1217–1222.

[9] Ji Minbiao et al. "Efficient multiple exciton generation observed in colloidal PbSe quantum dots with temporally and spectrally resolved intraband excitation". In: *Nano Lett.* 9.3 (2009), pp. 1217–1222.

[10] Arthur J. Nozik. "Nanoscience and nanostructures for photovoltaics and solar fuels". In: *Nano Lett.* 10.8 (2010), pp. 2735–2741.

[11] Matthew C Beard et al. "Third generation photovoltaics: multiple exciton generation in colloidal quantum dots, quantum dot arrays, and quantum dot solar cells". In: *2010 35th IEEE Photovolt. Spec. Conf.* (2010), pp. 000370–000375.

[12] Arthur J. Nozikhew. "Multiple exciton generation in semiconductor quantum dots". In: *J. Phys. Chem. Lett.* 2.11 (2011), pp. 1282–1288.

[13] Aaron G. Midgett et al. "Size and composition dependent multiple exciton generation efficiency in PbS, PbSe, and PbSxSe1-x alloyed quantum dots". In: *Nano Lett.* 13.7 (2013), pp. 3078–3085.

[14] Heather M. Jaeger, Kim Hyeon-Deuk, and Oleg V. Prezhdo. "Exciton multiplication from first principles". In: *Acc. Chem. Res.* 46.6 (2013), pp. 1280–1289.

[15] Fikeraddis A Damtie and Andreas Wacker. "Time dependent study of multiple exciton generation in nanocrystal quantum dots". In: *J. Condens. Matter* 696 (2016), p. 012012.

[16] Manoj Kumar et al. “Hot exciton cooling and multiple exciton generation in PbSe quantum dots”. In: *Phys. Chem. Chem. Phys.* 18.45 (2016), pp. 31107–31114.

[17] Vaidya Nathan, S. S. Mitra, and A. H. Guenther. “Review of multiphoton absorption in crystalline solids”. In: *J. Opt. Soc. Am. B* (1985).

[18] Wolfgang Ketterle. “Two-Photon excitation”. In: *MIT “Physics 8.421 At. Opt. Physics”* (2007).

[19] Mariacristina Rumi and Joseph W. Perry. “Two-photon absorption: an overview of measurements and principles”. In: *Adv. Opt. Photonics* 2.4 (2010), p. 451.

[20] Alexander W. Achtstein et al. “One- and two-photon absorption in CdS nanodots and wires: The role of dimensionality in the one- and two-photon luminescence excitation spectrum”. In: *J. Phys. Chem. C* 119.2 (2015), pp. 1260–1267.

[21] Gabriel Nagamine et al. “Two-photon absorption and two-photon-induced gain in perovskite quantum dots”. In: *J. Phys. Chem. Lett.* 9.12 (2018), pp. 3478–3484.

[22] He Huang et al. “Colloidal lead halide perovskite nanocrystals: synthesis, optical properties and applications”. In: *NPG Asia Mater.* (2016).

[23] Maksym V. Kovalenko, Loredana Protesescu, and Maryna I. Bodnarchuk. *Properties and potential optoelectronic applications of lead halide perovskite nanocrystals*. 2017.

[24] Mark C. Weidman, Aaron J. Goodman, and William A. Tisdale. *Colloidal halide perovskite nanoplatelets: an exciting new class of semiconductor nanomaterials*. 2017.

[25] Marc D. Levenson. “Multiphoton absorption”. In: *Introd. to Nonlinear Laser Spectrosc.* Elsevier, 1982, pp. 161–194.

[26] T.H. Maiman. “Stimulated optical radiation in Ruby”. In: *Nature* 187.4736 (1960).

[27] Richard L. Sutherland. *Nonlinear Optics. By Robert W. Boyd.* Vol. 31. 07. 2018, p. 1590.

[28] Guang S. He et al. “Multiphoton absorbing materials: Molecular designs, characterizations, and applications”. In: *Chem. Rev.* 108.4 (2008), pp. 1245–1330.

[29] D. F. Swinehart. “The Beer-Lambert Law”. In: *J. Chem. Educ.* 39.7 (1962), p. 333.

[30] R. D. Schaller and V. I. Klimov. “High efficiency carrier multiplication in PbSe nanocrystals: Implications for solar energy conversion”. In: *Phys. Rev. Lett.* 92.18 (2004), pp. 186601–1.

[31] E. Cartier et al. “Impact ionization in silicon”. In: *Appl. Phys. Lett.* 62.25 (1993), pp. 3339–3341.

[32] Charles Smith and David Binks. “Multiple exciton generation in colloidal nanocrystals”. In: *Nanomaterials* 4.1 (2013), pp. 19–45.

[33] D Timmerman et al. “Space-separated quantum cutting with silicon nanocrystals for photovoltaic applications”. In: *Nat. Photonics* 2.2 (2008), pp. 105–109.

[34] A. Shabaev, Al L. Efros, and A. J. Nozik. “Multiexciton generation by a single photon in nanocrystals”. In: *Nano Lett.* 6.12 (2006), pp. 2856–2863.

[35] M. Tuan Trinh et al. “Direct generation of multiple excitons in adjacent silicon nanocrystals revealed by induced absorption”. In: *Nat. Photon.* 6.5 (2012), pp. 316–321.

[36] Arthur J Nozik. “Spectroscopy and hot electron relaxation dynamics in semiconductor quantum wells and quantum dots”. In: *Annu. Rev. Phys. Chem.* 52.1 (Oct. 2001), pp. 193–231.

[37] D. Mukherji and B. R. Nag. “Band structure of semiconductor superlattices”. In: *Phys. Rev. B* (1975).

[38] K Fujlwara, Roberto Cingolani, and K. Ploog. "Spectroscopic investigations of miniband dispersion and excitonic effects in GaAs/AlAs short-period superlattices". In: *Solid State Commun.* 72.4 (1989), pp. 389–392.

[39] Jasprit Singh. *Electronic and Optoelectronic Properties of Semiconductor Structures.* 2012.

[40] Hiba Diab et al. "Impact of reabsorption on the emission spectra and recombination dynamics of hybrid perovskite single crystals". In: *J. Phys. Chem. Lett.* (2017).

[41] John William Strutt Rayleigh. *The theory of sound Vol. II.* 1896, p. 523.

[42] Kenju Otsuka. "Winner-takes-all dynamics and antiphase states in modulated multimode lasers". In: *Phys. Rev. Lett.* (1991).

[43] Tianyi Shen et al. "Highly stable and efficient all-inorganic lead-free perovskite solar cells with native-oxide passivation". In: *Nat. Commun.* 10.1 (2018), pp. 1–8.

[44] A Kojima et al. "Organometal halide perovskites as visible-light sensitizers for photovoltaic cells". In: *J. Am. Chem. Soc.* 131.17 (2009), pp. 6050–1.

[45] Yasuhiro Tachibana et al. "CdS quantum dots sensitized TiO2 sandwich type photoelectrochemical solar cells". In: *Chem. Lett.* (2007).

[46] NREL. "Solar cell efficiency chart". In: *Sol. cell Effic. chart* (2019).

[47] Luciana C. Schmidt et al. "Nontemplate Synthesis of CH3NH3PbB3 Perovskite Nanoparticles". In: *J. Am. Chem. Soc.* 136.3 (Jan. 2014), pp. 850–853.

[48] Jasmina A. Sichert et al. "Quantum size effect in organometal halide perovskite nanoplatelets". In: *Nano Lett.* 15.10 (2015), pp. 6521–6527.

[49] Verena a. Hintermayr et al. "Tuning the optical properties of perovskite nanoplatelets through composition and thickness by ligand-assisted exfoliation". In: *Adv. Mater.* (2016), pp. 1–8.

[50] Yu Tong et al. "Highly luminescent Cesium Lead Halide perovskite nanocrystals with tunable composition and thickness by ultrasonication". In: *Angew. Chemie Int. Ed.* 55.44 (Oct. 2016), pp. 13887–13892.

[51] Yu Tong et al. "From precursor powders to CsPbX3 perovksite nanowires: one-pot synthesis, growth mechanism and oriented self-assemblies". In: *Angew. Chemie - Int. Ed.* 56 (2017), pp. 13887–13892.

[52] Yu Tong et al. "Chemical cutting of perovskite nanowires into single-photon emissive low-aspect-ratio CsPbX3 (X=Cl, Br, I) nanorods". In: *Angew. Chemie - Int. Ed.* 57.49 (2018), pp. 16094–16098.

[53] Maksym V. Kovalenko and Maryna I. Bodnarchuk. "Lead halide perovskite nanocrystals: from discovery to self-assembly and applications". In: *Chim. Int. J. Chem.* 71.7 (2017), pp. 461–470.

[54] Michael A. Becker et al. "Bright triplet excitons in caesium lead halide perovskites". In: *Nature* 553.7687 (2018), pp. 189–193.

[55] Loredana Protesescu et al. "Nanocrystals of Cesium Lead Halide perovskites (CsPbX3, X = Cl, Br, and I): novel optoelectronic materials showing bright emission with wide color gamut". In: *Nano Lett.* 15.6 (2015), pp. 3692–3696.

[56] Ioannis Lignos et al. "Unveiling the shape evolution and halide-ion-segregation in blue-emitting formamidinium Lead halide perovskite nanocrystals using an automated microfluidic platform". In: *Nano Lett.* 18.2 (2018), pp. 1246–1252.

[57] Yu Tong et al. "Spontaneous self-assembly of perovskite nanocrystals into electronically coupled supercrystals : toward filling the green gap". In: *Adv. Mater.* 1801117 (2018), pp. 1–7.

[58] Grant Walters et al. “Two-photon absorption in oganometallic bromide perovskites”. In: *ACS Nano* 9.9 (2015), pp. 9340–9346.

[59] Basanth S Kalanoor et al. “Third order optical nonlinearities in organometallic methylammonium lead iodide perovskite thin films”. In: *ACS Photonics* (2016), acsphotonics.5b00746.

[60] Rui Zhang et al. “Nonlinear optical response of organic-inorganic halide perovskites”. In: *ACS Photonics* 3 (2016), pp. 371–377.

[61] Ke Wei et al. “Temperature-dependent excitonic photoluminescence excited by two-photon absorption in perovskite CsPbBr3 quantum dots”. In: *Opt. Lett.* 41.16 (2016), pp. 16–19.

[62] Jingzhou Li et al. “Two-photon absorption and emission in CsPb(Br/I)3 cesium lead halide perovskite quantum dots”. In: *CrystEngComm* 18.41 (2016), pp. 7945–7949.

[63] Wen Gao Lu et al. “Nonlinear optical properties of colloidal CH3NH3PbBr3 and CsPbBr3 quantum dots: a comparison study using Z-Scan technique”. In: *Adv. Opt. Mater.* 4.11 (2016), pp. 1732–1737.

[64] Nikolay S. Makarov et al. “Spectral and dynamical properties of single excitons, biexcitons, and trions in Cesium-Lead-Halide Perovskite quantum dots”. In: *Nano Lett.* 16.4 (2016), pp. 2349–2362.

[65] Elinore M. L. D. de Jong et al. “Multiexciton lifetime in all-inorganic CsPbBr3 perovskite nanocrystals”. In: *J. Phys. Chem. C* 121 (2016), pp. 1941–1947.

[66] Quinten A Akkerman et al. “Strongly emissive perovskite nanocrystal inks for high-voltage solar cells”. In: 2.December (2016), pp. 1–7.

[67] Guichuan Xing et al. “Low-temperature solution-processed wavelength-tunable perovskites for lasing.” In: *Nat. Mater.* 13.5 (2014), pp. 476–80.

[68] Haiming Zhu et al. “Lead halide perovskite nanowire lasers with low lasing thresholds and high quality factors”. In: *Nat. Mater.* 14.6 (June 2015), pp. 636–642.

[69] Philipp Brenner et al. “Continuous wave amplified spontaneous emission in phase-stable lead halide perovskites”. In: *Nat. Commun.* 10.1 (Dec. 2019), p. 988.

[70] Sergii Yakunin et al. “Low-threshold amplified spontaneous emission and lasing from colloidal nanocrystals of caesium lead halide perovskites”. In: *Nat. Commun.* 6 (2015), pp. 1–8.

[71] Zhiyuan Gu et al. “Two-Photon Pumped CH 3 NH 3 PbBr 3 Perovskite Microwire Lasers”. In: *Adv. Opt. Mater.* 4.3 (Mar. 2016), pp. 472–479.

[72] Yue Wang et al. “Nonlinear absorption and low-threshold multiphoton pumped stimulated emission from all-inorganic perovskite nanocrystals”. In: *Nano Lett.* 16.1 (2016), pp. 448–453.

[73] Aizhao Pan et al. “Templated self-assembly of one-dimensional CsPbX3 perovskite nanocrystal superlattices”. In: *Nanoscale* 9.45 (2017), pp. 17688–17693.

[74] Naiya Soetan et al. “Solvent-assisted self-assembly of CsPbBr3 perovskite nanocrystals into one-dimensional superlattice”. In: *J. Phys. Chem. C* 121.33 (2017), pp. 18186–18194.

[75] Julia S. van der Burgt et al. “Cuboidal supraparticles self-assembled from cubic CsPbBr3 perovskite nanocrystals”. In: *J. Phys. Chem. C* 122.27 (July 2018), pp. 15706–15712.

[76] Muhammad Imran et al. “Shape-pure, nearly monodispersed CsPbBr3 nanocubes prepared using secondary aliphatic amines”. In: *Nano Lett.* 18.12 (2018), pp. 7822–7831.

[77] Gabriele Rainò et al. “Superfluorescence from lead halide perovskite quantum dot superlattices”. In: *Nature* 563.7733 (2018), pp. 671–675.

[78] Kun Hua Wang et al. “Metal halide perovskite supercrystals: Gold-Bromide complex triggered assembly of CsPbBr3 nanocubes”. In: *Langmuir* 34.2 (2018), pp. 595–602.

[79] Yongqiang Ji et al. “Nanowire-assisted self-assembly of one-dimensional nanocrystal superlattice chains”. In: *J. Mater. Chem. C* (2019).

[80] Frank Stern and J. M. Woodall. “Photon recycling in semiconductor lasers”. In: *J. Appl. Phys.* 45.9 (1974), pp. 3904–3906.

[81] M. Alsari et al. “Photon recycling in lead iodide perovskite solar cells”. In: *Science (80-.).* 351.6280 (2016), pp. 1430–1433.

[82] M. Batsch et al. “Dipole-dipole coupling of excitons in double quantum wells”. In: *Phys. Rev. B* 48.16 (Oct. 1993), pp. 11817–11826.

[83] M.F.H. Schuurmans et al. “Superfluorescence”. In: *Adv. At. Mol. Phys.* Vol. 17. C. 1982, pp. 167–228.

[84] V. Sukhovatkin et al. “Room-temperature amplified spontaneous emission at 1300 nm in solution-processed PbS quantum-dot films”. In: *Opt. Lett.* (2005).

[85] Louis De Broglie. “Recherches sur la théorie des Quanta”. In: *Ann. Phys. (Paris).* 10.3 (1924), pp. 22–128.

[86] Aurora Manzi et al. “Resonantly enhanced multiple exciton generation through below-band-gap multi-photon absorption in perovskite nanocrystals”. In: *Nat. Commun.* 9.1 (2018).

[87] Cuong Dang and Arto Nurmikko. “Beyond quantum dot LEDs: Optical gain and laser action in red, green, and blue colors”. In: *MRS Bull.* (2013).

[88] Margherita Zavelani-Rossi et al. “Lasing in self-assembled microcavities of CdSe/CdS core/shell colloidal quantum rods”. In: *Nanoscale* (2010).

[89] Abhishek Swarnkar et al. “Colloidal CsPbBr3 perovskite nanocrystals: luminescence beyond traditional quantum dots”. In: *Angew. Chemie - Int. Ed.* 54.51 (2015), pp. 15424–15428.

[90] Yevgeny Rakita et al. “Low-temperature solution-grown CsPbBr3 single crystals and their characterization”. In: *Cryst. Growth Des.* 16.10 (2016), pp. 5717–5725.

[91] Justinas Butkus et al. “The evolution of quantum confinement in CsPbBr3 perovskite nanocrystals”. In: *Chem. Mater.* (2017).

[92] Chenkun Zhou et al. “Luminescent zero-dimensional organic metal halide hybrids with near-unity quantum efficiency”. In: *Chem. Sci.* (2018).

[93] Chunfeng Cai et al. “ Photoluminescence enhancement in wide spectral range excitation in CsPbBr 3 nanocrystal/Ag nanostructure via surface plasmon coupling ”. In: *Opt. Lett.* 44.3 (2019), p. 658.

Acknowledgements

This thesis is the result of the work I carried out between 2015 and 2019 at the **Chair for Photonics and Optoelectronics**, member of the Faculty of Physics of the LMU Munich. Being part of this team, I could experience the supportive environment, breeding ground for scientific discussions and personal growth, which is one of its distinctive marks. This provided me with the basis for the achievement of the scientific results that I have reported in this thesis, as well as for the professional growth that I have experienced during my time at the chair. I therefore avail myself of this occasion to express my gratitude to those who made all this possible.

First of all, I want to thank **Prof. Dr. Jochen Feldmann** for the great opportunity he gave me to join his chair for my PhD studies. He actively supervised my work, and offered me the possibility to design my experiments having access to some of the best equipment in the field. He has always been open to discuss my results and to provide very substantial input to the understanding of the physics behind the data. Furthermore, he enabled me to participate in collaborations, to converse with the top scientist he invited at the chair, to present my work in international conferences and in lecture halls, to supervise bachelor and master students, and even to organize myself a scientific workshop in my home town. I am extremely grateful for the trust I was given, that allowed me to grow as a scientist and as a woman.

I want to thank **Dr. Lakshminarayana Polavarapu** for his help in synthesising, together with **Dr. Yu Tong** and **Maximilian Feil**, the perovskite nanocrystals that I have used for these studies. I am very grateful that he provided me with new ideas given by his great experience in the field, and a great support in the preparation of my manuscripts. I am also thankful to **Prof. Dr. Alexander Urban** for his support during the first years of my PhD. His contagious enthusiasm and his advices helped me to develop my scientific skills.

Many thanks to all the fellow PhD students that I met at the chair for sharing this amazing experience with me. I am immensely grateful for the constructive environment that we have created, where everybody was willing to lend a hand if someone needed, without expecting much in return. Among them I feel obliged to mention **Dr. Verena Hintermayr**, **Christoph Maier**, **Bernhard Bohn**, **Florian Erhat**, **Dr. Carla Pernpeintner**, **Patrick Urban**, **Stefanie Pritzl**, **Alexander Richter** and (although he did not do his PhD at the chair) **Felix Winterer**. Spending this important phase of our life together we ended up becoming friends rather than just colleagues.

I also want to thank **Simone Strohmair** for being a great office mate and always my roommate, whenever we joined a conference together. Discussing with her has always been a pleasure, whether the topic was setting up experiments, understanding scientific laws or private life. I would also like to thank **Dr. Jenny Merlin** for the time we spent at the chair together and for the friendship which has grown between us.

I am thankful to all the students that I had the chance to supervise: **Verena Pichler**, **Abraham Moreno Moreno**, **Julius Feucht**, **Daria Markina**, **Maximilian Feil** and **Philipp Konrad**. Working with them taught me a lot, and I am really grateful that they chose me for getting introduced to the methodology of scientific work.

Besides, special thanks go to all those who helped me revising the draft of this thesis: **Bernhard Bohn**, **Dr. Verena Hintermayr**, **Nicola Kerschbaumer**, **Christoph Maier**, **Dr. Lakshminarayana Polavarapu**, **Stefanie Pritzl**, **Alexander Richter**, **Sebastian Rieger**, **Francis Schuknecht**, **Simone Strohmair**, **Ilka Vincon** and **Dr. En-Ping Yao** and to all the current and former members of the chair.

I wish to express my infinite gratitude to **Gerlinde Adam**, for always providing a ready help with administrative matters and whenever her human support was needed. I thank also **Stefan Niedermaier** and **Talee Barghouti** for their technical help, as well as **Nicola Kerschbaumer** and **Francis Schuknecht** for the IT support.

Last but not least, the biggest thanks go to my family: **Andrea Piazza**, for always encouraging me to give my best and to dream big, for providing me with all the love and support I needed and for becoming my husband during this journey. The sweetest thanks go to our baby growing inside me, for giving me the right motivation to complete this ambitious project in the best possible way, and for being so kind to me during these first months together. I also want to thank my parents **Tania** and **Felice**, and my sister **Simona** for always being my biggest fans.

Furthermore, I am very grateful to my Italian friends living in Munich, and to the ones which are part of the **MCC**, for creating a family atmosphere in which to grow together. Finally, I want to acknowledge **Piero Angela** for inspiring me with the fascinating documentaries about science and nature that I enjoyed watching since I was a little girl and that helped me choose the career I am pursuing today.